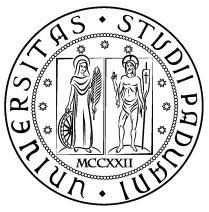

UNIVERSITÀ DEGLI STUDI DI PADOVA

CISAS "G. Colombo"

Center of Studies and Activities for Space

Doctorate of Philosophy Thesis

BASE REACTION CONTROL OF SPACE MANIPULATORS

CONTROLLO DELLE REAZIONI DI MANIPOLATORI PER UTILIZZI SPAZIALI

Ph.D. Candidate:

Isacco Pretto

Doctoral School in
Sciences Technologies and Measurements for Space

Curriculum
Astronautics and Satellite Sciences

XXII *Ciclo di Dottorato*

School Director: Prof. Cesare Barbieri
Department of Astronomy, University of Padova, Italy

Curriculum Coordinator: Prof. Giampiero Naletto
Department of Information Engineering, University of Padova, Italy

Supervisor: Dr. Silvio Cocuzza
CISAS "G. Colombo", University of Padova, Italy

28 January 2010

Abstract

In this thesis a research activity is presented, concerning matters of dynamics and control of robot manipulators for space robotics applications. In particular, kinematic control principles suitable for the realization of trajectory-tracking manoeuvres are considered for manipulators in the kinematic redundancy condition, that is typically available on actual space robotic systems. A well known characteristic of space manipulators is due to the dynamic coupling that arises between the manipulator motion and the motion of the base spacecraft on which the manipulator is mounted, due to action-reaction exchanges between the subsystems, and to the characteristics of their momentum equations that determine the non-holonomic nature of the system. This coupling determines dynamic disturbances generated by the manipulator during operation. It reveals important to control these disturbances in order to respect the pointing requirements of the spacecraft, for what concerns communications, on-board instrumentation, and solar panels orientation, and also for what concerns restrictions on the admissible acceleration disturbances exerted on the base platform, that in particular can be imposed during experimental micro-gravity activities onboard the space station. Fundamental objective of the kinematic control schemes developed in this work is to achieve an optimization of the possible joint trajectories that command the movement of the arm, in order to minimize the dynamic disturbances exerted on the platform, which is possible thanks to a balanced coordination of the arm internal motions, that compensates for its momentum variations that are produced during a trajectory-tracking manoeuvre. Original formulations for the base reaction control are presented and analyzed, and the problem is set in the mathematical framework of constrained least squares methods, while the kinematic control is resolved at the joint acceleration level, in order to attain an effective expressions of the kinematic and dynamic variables involved. The proposed principles reveal suitable for real-time space applications, thanks to the local formulation of the optimization problems and to the use of stable and consolidated solution routines. Analysis and validation of the proposed laws have been developed be means of an experimental test campaign on a planar robot manipulator

prototype with three degrees-of-freedom, suspended by air bearings on a flat granite plane, in order to simulate the microgravity environment. In particular a series of trajectory-tracking tests have been performed with dynamic measurements of the resultant base reactions. The analysis is completed by means of a robot simulator system, that has been developed by reproducing the geometrical and inertial characteristics of the experimental prototype. The performance of the control laws have been evaluated both in the fixed base condition, and in the free-floating base condition, and in this case an evaluation on the influence of the inertial parameters involved have been carried out. An independent research activity was related to the application of optimization methods for contact forces control of a bio-inspired climbing robots with dry adhesive pads. Control principles are presented, and their performances evaluated by means of a robot simulator and validated through an experimental robot prototype.

$\sim$

In questa tesi è presentato un lavoro di ricerca sulla dinamica ed il controllo di bracci robotici per applicazioni spaziali. In particolare, sono proposti dei principi di controllo cinematico adatti all'inseguimento di traiettorie nello spazio operativo del manipolatore in condizioni di ridondanza cinematica, le quali sono tipicamente disponibili negli attuali sistemi robotici spaziali. Caratteristica meccanica peculiare delle applicazioni di robotica orbitale è l'accoppiamento dinamico che si verifica tra il moto del braccio ed il moto della piattaforma satellitare sulla quale è montato, dovuto agli scambi di azione e reazione che i due sottosistemi si scambiano tra di loro ed alla natura non-olonomica del sistema. Tale accoppiamento è causa di disturbi dinamici esercitati dal manipolatore in fase di operazione, che è necessario controllare in modo da ottemperare sia ai requisiti di puntamento del satellite per quanto riguarda le comunicazioni, la strumentazione di bordo, e l'orientazione dei pannelli solari, sia alle restrizioni sui disturbi di accelerazione impartiti alla piattaforma, che in particolare possono essere imposte durante attività sperimentali in microgravità a bordo della stazione spaziale. Obiettivo fondamentale degli schemi di controllo cinematico sviluppati in questo lavoro, è quello di realizzare una ottimizzazione delle possibili traiettorie di giunto che comandano il movimento del braccio, in modo da minimizzare il disturbo dinamico esercitato sulla piattaforma, reso possibile attraverso la coordinazione dei movimenti interni del braccio, i quali compensino le variazioni di momento che si producono in questo durante l'inseguimento di

traiettoria. Formulazioni originali di controllo delle reazioni sono presentate ed analizzate, attraverso il supporto matematico dei metodi ai minimi quadrati vincolati, mentre il controllo cinematico è risolto al livello delle accelerazioni di giunto, in modo da poter esprimere in maniera efficace le grandezze cinematiche e dinamiche coinvolte. I principi proposti si rivelano adatti per l'implementazione in tempo reale in applicazioni spaziali, grazie all'impostazione dei problemi in forma locale ed alla possibilità di utilizzo di algoritmi numerici stabili e consolidati. L'analisi e la validazione delle leggi proposte è stata effettuata attraverso prove sperimentali su un manipolatore planare sperimentale a tre gradi di libertà, sospeso su cuscinetti d'aria in modo da simulare l'ambiente di microgravità, con il quale sono state effettuate prove di inseguimento con misure dinamiche dei disturbi di reazione. L'analisi sperimentale è accompagnata dallo sviluppo di un ambiente di simulazione, il quale riproduce le caratteristiche geometriche ed inerziali del robot sperimentale. Le prestazioni delle leggi di controllo sono state valutate sia per le condizioni di vincolo a base fissa, che di base libera, ed in quest'ultimo caso sono state effettuate valutazioni rispetto all'influenza dei parametri inerziali coinvolti. Una parte indipendente del lavoro, riguarda infine l'applicazione di metodi di ottimizzazione per il controllo delle forze di adesione, adatti al controllo di robot arrampicatori, i quali sfruttano l'utilizzo di sistemi di adesione secca in modo da aumentare l'aderenza alla superficie. I principi di controllo sono testati attraverso un simulatore ed i risultati validati in un robot prototipo sperimentale.

Contents

Acknowledgments

The author would like to acknowledge Prof. F. Angrilli and Prof. S. Debei, for the scientific discussions and the financial support on this research project; Dr. S. Cocuzza for the constant mentorship and interest on this research activity, and the perseverance in setting up and performing the experimental validation campaign; Prof. C. Menon for the motivating research meetings and the enthusiasm towards the development of innovative concepts during the months as a visiting scholar at the Simon Fraser University in Vancouver BC (Canada); the other M.S. and Ph.D. students at the robotics laboratory at the Simon Fraser University for the pleasant working environment, and in particular S. Ruffieux and Y. Li also for their contributions in the experimental tests regarding the climbing robot project; the Ph.D. students and post-docs at the CISAS center of the University of Padova (Italy) who shared their passion for research and an enthusiastic attitude towards space sciences and technologies. Finally, I would like to thank my family and my friends, for their valuable support and for sharing the gratifications of the achievements during these three years of doctorate of research.

Chapter 1

Sommario esteso

Il tema principale di ricerca presentato in questa tesi riguarda il controllo delle reazioni dinamiche esercitate alla base di manipolatori per utilizzi spaziali durante manovre di inseguimento di traiettoria. Il problema viene affrontato attraverso la definizione di schemi di controllo cinematico al livello delle accelerazioni di giunto, all'interno del contesto operativo del Controllo ad Accelerazione Risolta (RAC), e viene sfruttata la caratteristica di ridondanza cinematica tipica dei manipolatori spaziali in modo da provvederne delle risoluzioni ottime al livello delle accelerazioni di giunto.

L'ottimizzazione delle traiettorie di giunto è resa possibile attraverso schemi di ottimizzazione ai minimi quadrati vincolati, i quali, ai fini del raggiungimento degli obiettivi preposti, sono applicati nelle formulazioni dei problemi ai minimi quadrati con vincoli di uguaglianza, denominati *Least Squares problems with Equality constraints* (LSE) ed estese alla formulazione di problemi ai minimi quadrati con vincoli di uguaglianza e disuguaglianza, denominati *Least Squares problems with Equality and Inequality constraints* (LSEI), in modo da poter considerare l'intervento dei limiti di giunto nella soluzione.

Tale impostazione del problema si presta all'implementazione per applicazioni di manovra in tempo reale, grazie alla disponibilità di algoritmi consolidati ed efficienti per la soluzione dei problemi ai minimi quadrati ed il calcolo delle grandezze cinematiche e dinamiche coinvolte, ed all'definizione del problema di ottimizzazione in forma locale.

La possibilità di conseguire l'ottimizzazione delle prestazioni dinamiche durante il movimento del braccio è resa possibile attraverso una preliminare modellazione cinematica e dinamica del sistema studiato. In accordo con approcci consolidati in robotica, il sistema composto dal satellite e dal braccio robotico montato su di esso, è modellato come un sistema articolato com-

posto di una catena cinematica aperta di corpi rigidi, vincolati tra di loro attraverso giunti elementari.

Attraverso la modellazione cinematica e dinamica, è possibile ottenere le richieste equazioni differenziali cinematiche e dinamiche al livello delle accelerazioni di giunto. Gli schemi di modellazione sono presentati sia per la configurazione di vincolo a base fissa, sia per la configurazione a base libera, e ne è sottolineata l'analogia strutturale. Per mezzo di essa è mostrato come è possibile impostare il problema cinematico e dinamico sotto una comune formulazione.

In particolare la cinematica a base fissa è presentata attraverso l'uso della matrice Jacobiana del manipolatore, nota anche come *Fixed Base Jacobian* matrix (FJB), mentre la cinematica a base libera è presentata sia attraverso l'utilizzo della FBJ, sia attraverso l'uso della matrice Jacobiana generalizzata del sistema base-manipolatore, nota in letteratura come *Generalized Jacobian Matrix* (GJM). Attraverso la prima è possibile l'inseguimento di riferimenti espressi nel sistema della piattaforma, mentre attraverso la GJM è possibile l'inseguimento di riferimenti nel sistema inerziale esterno.

Le equazioni della dinamica sono quindi proposte per quanto riguarda le relazioni differenziali intercorrenti tra le variabili di giunto e le loro derivate, rispetto alle forze e coppie di reazione esercitate alla base in conseguenza ai movimenti del braccio. Attraverso di esse, è stato definito il vettore delle reazioni pesate, equivalente a una combinazione lineare pesata con una matrice di peso. Grazie all'introduzione della matrice di peso, è possibile la valutazione complessiva dell'effetto dinamico sulla base, e la definizione di una funzione di costo del problema di ottimizzazione dinamica. Analogamente al caso cinematico, anche nel caso dinamico è stata quindi proposta la formulazione per la configurazione di vincolo a base fissa, e per la configurazione a base libera, la quale porta alla definizione di differenti matrici di massa.

In seguito alla derivazione delle equazioni dirette dei modelli, è possibile osservare non solo l'analogia strutturale delle due condizioni di vincolo della base, ma allo stesso modo l'esistenza di un'analogia strutturale anche per quanto riguarda le relazioni cinematiche e dinamiche tra di loro. Grazie all'impostazione del problema di controllo delle reazioni attraverso l'utilizzo di metodi ai minimi quadrati lineari, è possibile sfruttare appieno tale analogia. La differenza fondamentale nella valutazione delle variabili coinvolte, è data dal fatto che nel caso a base libera è necessario disporre di valori aggiornati delle variabili di orientazione della piattaforma satellitare, attraverso elaborazione dei segnali di misura di assetto forniti dalla strumentazione di bordo, oppure tramite integrazione numerica. Ciò è dovuto, come noto, alla natura anolonoma del sistema costituito dal satellite e dal manipolatore, dato dalla non integrabilità delle equazioni del momento angolare nel caso generale.

Essendo il problema affrontato al livello delle accelerazioni, si osserva che le equazioni cinematiche e dinamiche risultano lineari rispetto alle accelerazioni di giunto, le quali rappresentano la variabile di controllo del problema, mentre le variabili delle velocità di giunto, delle posizioni di giunto, e della posizione del satellite – nella configurazione a base libera -sono considerate come variabili di stato.

A questo punto, è possibile definire in maniera completa il problema di ottimizzazione e controllo, attraverso la definizione di opportune funzioni di costo. Il problema fondamentale della minimizzazione delle reazioni, è quindi impostato in forma locale nelle accelerazioni di giunto, mentre la funzione di costo è definita come la norma del vettore delle reazioni pesate, ovvero la norma pesata del vettore composto, costituito da forze e coppie di reazione risultanti.

Il problema di inseguimento di traiettoria, costituisce in questo contesto il vincolo di uguaglianza del problema LSE, di dimensione pari al grado di ridondanza cinematica del braccio rispetto alla dimensione del vettore cinematico di inseguimento. All'interno di tale vincolo, è ricercata la soluzione ottima che genera il minimo disturbo di reazione. La soluzione è fornita sia in forma chiusa attraverso espressioni algebriche, sia attraverso l'utilizzo di una matrice Jacobiana estesa opportunamente definita, che si presenta adatta all'utilizzo in schemi pseudo-inversi ed alla risoluzione del problema LSE per mezzo del metodo dei pesi. Il problema con limiti di accelerazione di giunto LSEI è stato quindi proposto come completamento della struttura di controllo.

Come soluzione particolare, è investigato il caso del problema cinematico e dinamico inverso, la cui soluzione è ammessa in particolari condizioni dimensionali, date dal minimo numero di ridondanze con le quali è possibile investigare la possibilità di una soluzione esatta dell'inseguimento di traiettoria, e di ottenere allo stesso tempo una reazione pesata nulla durante il movimento. Le soluzioni sono quindi confrontate alla tradizionale risoluzione pseudo inversa ai minimi quadrati, il cui problema è denominato *Least Squares* (LS), la quale nel caso ridondante produce il moto di minima accelerazione di giunto.

Una estensione del problema è quindi proposto attraverso l'estensione del metodo dei pesi, la quale permette ottenere un miglioramento delle performance di riduzione del disturbo di reazione, sfruttando la possibilità di attenuare la precisione di inseguimento del vincolo cinematico. In questo caso è stata definita una opportuna funzione di costo, composta sia di un contributo dinamico, che da uno cinematico.

Quindi, dopo la presentazione dell'impianto teorico del controllo delle reazioni, viene presentata una campagna di test di simulazione, seguita dalla validazione sperimentale dei risultati. Il sistema sperimentale è costituito da un braccio robotico prototipo planare a tre gradi di libertà (GDL), presente

nei laboratori del CISAS presso l'Università di Padova, sospeso su di un piano di granito per mezzo di cuscinetti d'aria in modo da simulare l'ambiente di microgravità. Il manipolatore è controllato da un sistema di asservimento industriale, mentre una bilancia dinamometrica collegata con la flangia di attacco del braccio, fornisce le misure dinamiche delle forze e coppie di reazione risultanti. Un simulatore è stato sviluppato dall'autore, il quale riproduce le caratteristiche geometriche ed inerziali del braccio, ed estende la possibilità di analisi alla configurazione a base libera.

Sono quindi presentati test di inseguimento di traiettoria con misure di forze e coppie di reazione per il caso a base fissa, nella condizioni più generali di controllo delle reazione, e confrontate le prestazioni degli schemi di soluzione LS, LSE, ed LSEI, sia attraverso simulazione, sia attraverso test sperimentali. Segue una fase di analisi di sensibilità rispetto alle variabili più significative. In particolare, viene valutata l'influenza della scelta dei fattori di peso nella definizione della reazione pesata, l'influenza dei valori massimi dei limiti di accelerazione imposti, e delle caratteristiche inerziali del braccio. Quindi dei test sono presentati i quali intendono valutare le possibilità di miglioramento delle performance dinamiche attraverso il rilassamento del vincolo cinematico.

Come condizione dimensionale particolare è in seguito testata la minimizzazione della sola coppia di reazione, dimostrando la possibilità di ottenere l'inseguimento di traiettoria con un profilo di reazione nulla alla base. Anche per tale caso significativo, vengono presentati la fase di simulazione, seguita dalle validazioni sperimentali, per le soluzioni LS, LSE, ed LSEI. Quindi viene proposta un'analisi dello spazio di lavoro a reazioni nulle, attraverso una campagna di simulazione, dimostrando la validità del principio per un elevato numero di traiettorie di prova.

Alla presentazione dei risultati nel caso a base fissa, segue l'esposizione dei test di simulazione sulla configurazione a base libera. Test di inseguimento vengono effettuati per i diversi schemi di controllo, ed in particolare l'attenzione è qui concentrata nell'indagine delle condizioni di reazione nulla. I risultati sono analizzati per diverse caratteristiche inerziali della piattaforma, sia rispetto al disturbo dinamico generato, che rispetto ai valori delle variabili di giunto coinvolte.

In conclusione della parte riguardante lo studio sui manipolatori robotici, è quindi presentata una estensione delle applicazioni al caso generale dell' inseguimento di un profilo di reazione, attraverso cui è possibile ottenere un controllo completo sia delle accelerazioni all'end-effector, sia delle reazioni generate. Tale estensione suggerisce prospettive interessanti nel contesto della possibilità di coordinazione di più bracci montati sulla stessa piattaforma.

Come argomento collaterale, è quindi presentato il lavoro riguardante delle applicazioni per robot arrampicatori, svolto in collaborazione con la Simon Fraser University di Vancouver in Canada. Tale ricerca si inserisce

nel contesto della realizzazione di un sistema robotico arrampicatore, che sfrutta dispositivi di attacco con adesione secca, i quali traggono ispirazione dalle caratteristiche adottate in natura da alcune specie di rettili.

In questo contesto, sono stati affrontati due argomenti di ricerca. Il primo riguarda la proposta di un modello di adesione semplificato adatto ad essere implementato in sistemi di simulazione e controllo per applicazioni robotiche. Il secondo riguarda lo studio di schemi di controllo per migliorare la stabilità di un robot arrampicatore in condizioni di inclinazione anche critiche. Per quanto riguarda il modello di adesione, è stata effettuata una campagna di prova per una tipologia di materiale polimerico innovativa dotata di microstruttura, a contatto con una superficie di vetro, e un modello è stato proposto e testato. Nel contesto, invece, del controllo delle forze di contatto, viene presentato un originale approccio al problema, che consiste nell'ottimizzazione delle forze di contatto del sistema robotico, nel rispetto dei vincoli di equilibrio statico del suo insieme. Due tipologie di soluzione sono proposte e confrontate. Viene presentato sia un approccio al problema ai minimi quadrati; che un approccio di tipo *minimax*, assieme alla metodologia per ottenere le corrispondenti coppie di giunto. Gli schemi sono stati testati sia per quanto riguarda le forze di contatto, che per quanto riguarda le coppie di giunto: I test sono stati effettuati in diverse condizioni operative attraverso un sistema di simulazione, mentre validazioni sperimentale sono stati realizzate attraverso un robot prototipo messo a punto nei laboratori della Simon Fraser University.

Chapter 2

Introduction

The use of space robotic manipulation systems for on-orbit applications is a relatively recent fact, that mainly relies on space operation support provided by the two Canadian-built manipulators, operating on the Space Shuttle – the Shuttle Remote Manipulator System (SRMS) – and on the International Space Station (ISS) – the Space Station Remote Manipulator System (SSRMS) – that, together with the Special Purpose Dexterous Manipulator (SPDM) and the Mobile Base System (MBS), forms the Mobile Servicing System (MSS), that reveals a central role in support of many space operation missions. More recently a Japanese robotic arm have appeared in the Japanese Experimental Module (JEM) on the ISS, the Japanese Remote Manipulator System (JEM RMS), and the near future will see a European Robotic Arm (ERA) mounted on the Russian segment of the space station.

The use of robotic technologies for space applications presents the main advantages that risks faced by astronauts are reduced, especially for what concerns Extra Vehicular Activities (EVA), that can be performed or assisted by a robotic arm, and also that productivity results increased. The grasping and maneuvering capabilities of a robotic manipulator are also essential in handling massive payloads, such as in berthing operations with target vehicles and spacecrafts. Former studies on space robotic missions and their analysis in EVA and Intra Vehicular Activities (IVA) were part of the NASA telerobotic program [1, 2, 3] and research on dynamics and control of space robotic systems began to provide the first significant results in the 1980s. Since then, research on space robotics have advanced to the point that several studies have been carried out about the opportunity of the utilization of space service units equipped with robotic manipulators, for on-orbit satellite servicing missions, space assembly, and space exploration applications. Recent reviews on actual applications and research programs

in space robotics can be found in [4] and in [5].

Among the most significant experimental modules that have been developed in order to investigate the feasibility of on-orbit service systems, it should be mentioned the Japanese ETS-VII mission, and the American Orbital Express, while fundamental pioneering works on dynamics and control of space robotics system have been developed especially at the MIT and in Japan by Dubowsky and Papadopoulos [6, 7, 8], and Nenchev, Umetani and Yoshida [9, 10, 11] . A survey on the fundamental theory in dynamics and control of space robotic systems can be found in [12], while a more recent review can be found in [13]. A fundamental characteristic of space manipulators, that differentiates them from terrestrial application manipulators, resides in the dynamic coupling that exists between the motion of the robot manipulator and the motion of the base spacecraft, due to the fact that the manipulator exerts reaction forces and torques on the base during manoeuvres. In this thesis, the problem of controlling the base reaction disturbance while performing a general target-tracking manoeuvre is tackled, and original contributions to the body of literature on the subject is provided, by exploiting the manipulator redundancy in order to minimize a cost function of the base reactions. The minimization of the base reaction disturbance on the base spacecraft is fundamental for the following reasons [3]: 1) in order to maintain the antennas communication link, the orientation of pointing instrumentation and scanning devices, since reduced dynamic disturbances result in a reduced energy consumption of the Attitude Control System (ACS) for the maintenance of the desired attitude, or for the reorientation after the manipulator manoeuvre and, therefore, lead to an increased system useful life; 2) in order to preserve the microgravity environment onboard the spacecraft; 3) in order to reduce the energy consumption of the propulsion system, if a controlled spacecraft attitude and/or position is required.

Redundancy resolution schemes have been proposed in literature according to a kinematic approach, for the local minimization of the spacecraft angular velocity, exploiting the the momentum and angular momentum conservation laws [6, 9]. In particular, robot motions, if any, that allow to maintain the same spacecraft attitude can be found by means of the Fixed Attitude Restricted (FAR) Jacobian matrix introduced by Nenchev et al. [14]. Heuristic path planning methods that proposed the introduction of a disturbance map by Dubowsky et al. [6, 15], have also been proposed. The non-holonomic properties of the system in the path planning problem has been pointed out by Nakamura and Mukheerjee in [16, 17]. On the other hand, other authors proposed a dynamic approach, that is also the approach used in this thesis, the object of which consists in the reduction of the reactions transferred to the base spacecraft. A local optimization approach for reaction minimization was proposed by De Silva and Quinn [18, 19], in which a Rayleigh-Ritz technique and polynomial shape functions are used

in order to optimize the joint trajectories. A Lagrangian constrained optimization method has been proposed by Schäfer, Krenn et al. in [20, 21], in which second and forth order polynomials have been used in order to approximate the base motion. The Reaction Null Space (RNS) concept have been proposed by Nenchev et al. [22, 23] in order to study the existence of zero reaction paths in the manipulator workspace. Globally optimal solutions outperform local solutions for a defined manipulation manoeuvre, but require heavy computations that rule out real-time control [19], and are not suitable for teleoperation purposes.

The solutions to the base reaction control problem proposed in this thesis are developed in the framework of local optimization methods in which the manipulator kinematics equations are inverted by means of considering the optimization of dynamics cost functions into account, thanks to the availability of a kinematic redundancy. The resolutions of the redundancy is carried out at the joint acceleration level, in the context of the Resolved Acceleration Control [24], providing an extension of kinematic control principles for redundant manipulators [25, 26], in terms of Jacobian pseudoinverse formulations, and extended Jacobian formulations. The proposed optimization problem setting makes use of constrained least squares methods [27, 28, 29], and optimization problems are defined in the form of Least Squares problems with Equality constraints (LSE), suitable for real-time applications [30, 31, 32]. The introduction of joint acceleration limits in the solution have been studied by means of the formulation of Least Squares Problem with Equality and Inequality constraints (LSEI). Furthermore, closed form solutions to the defined LSE problems have been given, and a formulation of the solution have been introduced by means of the weighting method [33, 34, 27]. By an extension of the applications of the weighting method, a solution have been provided that allows the reduction of the base reactions up to a desired level, by means of relaxing the end-effector tracking requirements.

Kinematic control problems and their solutions are presented, and their performance tested by simulations, and validated by means of a 3 degrees-of-freedom (DOF) planar manipulator prototype. Sensitivity studies are carried out for the significant dynamic and control variables, and the performance analyzed in different operative conditions. The control problems, their solutions, and their tests, have been carried out both for the fixed base configuration and for the free-floating base configuration. The existence of zero reaction solutions have been demonstrated and validated, and a zero reaction workspace study has been carried out for different robot inertial properties. The control principles have then been extended to the definition of the new concept of base reaction tracking, that reveals promising in terms of defining manoeuvres that exert an exact desired base reaction, eventually zero, and in possible coordination principles for multi-manipulator systems.

A collateral work is presented in the final part of this thesis, that presents a study on modeling and control of the contact forces of bio-inspired climbing robots, that has been studied by means of Least Squares (LS) and Minimax (MMX) optimization routines, followed by simulation tests and experimental validation, which have been carried out in cooperation with the Simon Fraser University.

The thesis is organized as follows: Chapter 4 presents the kinematics and dynamics model of a space manipulator; in Chapter 5 the base reaction optimization framework is developed, that represents the general basis on which the solutions of foregoing chapters are founded; Chapter 6 presents the reaction control schemes as applied to a fixed base manipulator, and its simulation and experimental test campaign; Chapter 7 extends the base reaction control to the free floating base condition, and simulation tests are presented and analyzed; in Chapter 8 an extended application is proposed in which a base reaction tracking manoeuvre is performed; Chapter 9 presents the research activity on climbing robots; and Chapter 10 concludes the thesis. An overview about constrained least squares methods is provided in Appendix A.

The results of this thesis, have been published by the author and his research group in the following articles [35, 36, 37, 38, 39, 40, 41, 42, 43, 44, 45], to which the reader is referred for further informations and details.

Chapter 3

Notation

A brief description on the notation used in this work is exposed in this Chapter. In order to describe the physical quantities and their numerical description, three fundamental geometrical elements are used: scalars, vectors, and arrays.

Scalars Scalars are identified by normal symbols, lower-case when possible, such as:

$$t, k, \rho \tag{3.1}$$

Euclidean space For what concerns vectors, since they represent geometrical or physical entities which description depends on the geometrical observer, a distinction is made between a vector, intended as the physical entity, and its representation in a given reference frame, here denoted as *component array*. The term *vector* will sometimes be used for both when it's clear the context. *Euclidean points* and reference frames will have a separate notation. Euclidean points are represented as normal symbols, upper-case, like:

$$P, Q, \Omega \tag{3.2}$$

Vectors are represented with an arrow like:

$$\vec{v}, \vec{\omega}, \vec{F} \tag{3.3}$$

Reference frames are denoted with the symbol $\vec{\Sigma}$ and an index that identifies the frame, like:

$$\vec{\Sigma}_A, \vec{\Sigma}_B, \vec{\Sigma}_N \tag{3.4}$$

Reference frames are defined as a set of an Euclidean point as origin, and three normal right-handed unit vectors, for example $\Sigma_N = \{O, \vec{e_1}, \vec{e_2}, \vec{e_3}\}$.

Component arrays Finally, component arrays are ordered collections of scalars, and are represented with a bold symbol. An index in the upper-left side of the symbol identifies the projection frame when useful. Some examples may be:

$$\boldsymbol{f}, {}^{B}\boldsymbol{\omega}, {}^{N}\boldsymbol{R} \tag{3.5}$$

Component arrays are representations of vectors in a reference frame, for example:

$${}^{A}\boldsymbol{v} = (\vec{\Sigma}_A \cdot)\, \vec{v} \tag{3.6}$$

The component array notation is used to represent vectors and *matrices*:

$$\boldsymbol{F} = \begin{bmatrix} F_1 \\ F_2 \\ F_3 \end{bmatrix} \quad \boldsymbol{Q} = \begin{bmatrix} Q_{11} & Q_{21} & Q_{31} \\ Q_{12} & Q_{22} & Q_{32} \\ Q_{13} & Q_{23} & Q_{33} \end{bmatrix} \tag{3.7}$$

Observe that an array representation of an Euclidean vector is a column array.

Operations

Products Consider two vectors $\vec{v}$ and $\vec{u}$. The internal (dot) product between vectors is expressed as:

$$c = \vec{v} \cdot \vec{u} \tag{3.8}$$

Where a reference frame $\vec{\Sigma}_b$ is chosen, the *same* scalar result can be obtained from the corresponding array internal product expressed as:

$$c = \boldsymbol{v}^T \boldsymbol{u} = \begin{bmatrix} v_1 & v_2 & v_3 \end{bmatrix} \begin{bmatrix} u_1 \\ u_2 \\ u_3 \end{bmatrix} \tag{3.9}$$

The external (cross) product between the vectors is expressed as:

$$\vec{w} = \vec{v} \times \vec{u} \tag{3.10}$$

and between arrays in $\vec{\Sigma}_b$ components as:

$$\boldsymbol{w} = \boldsymbol{v}^{\times} \boldsymbol{u} = \begin{bmatrix} 0 & -v_3 & v_2 \\ v_3 & 0 & -v_1 \\ -v_2 & v_1 & 0 \end{bmatrix} \begin{bmatrix} u_1 \\ u_2 \\ u_3 \end{bmatrix} \tag{3.11}$$

The expression $\boldsymbol{v}^{\times}$ identifies the *skew matrix* associated with $\boldsymbol{v}$.

Point differences Two points P and Q can be joined by a vector which is associated with them and is denoted as $\overrightarrow{PQ}$, from P to Q. Given any third point O, a difference between points can be defined as

$$\overrightarrow{PQ} = Q - P \triangleq \overrightarrow{OQ} - \overrightarrow{OP} \tag{3.12}$$

The last point-difference has this clear meaning, and identifies the same vector for whatever origin.

Relevant entities

Position vector The position of a Point G *w.r.t* a point O is an applied vector defined as:

$$\vec{r}_{OG} \triangleq \overrightarrow{OG} \tag{3.13}$$

It is preferable for O to be the origin of a Reference Frame. If the reference point O is clear, it may be also written $\vec{r}_G$. If also the point G is clear from the contexrt, it may be written directly $\vec{r}$.

Direction cosine matrix The orientation of a reference frame $\vec{\Sigma}_B = \vec{\Sigma}_A = \{O_A, \vec{a}_1, \vec{a}_2, \vec{a}_3\}$ is a matrix defined by the expression (projection) of the orientation part of $\vec{\Sigma}_B$, say $\vec{C}_B$ in $\vec{\Sigma}_A$. It is also known as Direction Cosine Matrix (DCM) and is given by:

$${}^A\boldsymbol{C}_B = \left[{}^A\boldsymbol{b}_1\, {}^A\boldsymbol{b}_2\, {}^A\boldsymbol{b}_3\right] \tag{3.14}$$

It also represents rotation matrices, and is sometimes addressed as ${}^A\boldsymbol{R}_B$ in literature. Nevertheless the symbol $\boldsymbol{C}$ is used in this thesis. Observe that the basis of a reference frame $\vec{C}_B$ projected as 3 column vectors can be represented as a DCM as ${}^A\boldsymbol{C}_B$.

Rototranslation homogeneous matrix A roto-translation matrix (RTM) is a matrix representation of a reference frame of origin $\boldsymbol{r}$ and orientation matrix $\boldsymbol{C}$, and is defined as:

$$\mathbf{T} = \begin{bmatrix} \boldsymbol{C} & \boldsymbol{r} \\ \mathbf{0}^T & 1 \end{bmatrix} \tag{3.15}$$

The notation:

$${}^A\mathbf{T}_B = (\vec{\Sigma}_A \cdot)\vec{\Sigma}_B \tag{3.16}$$

represents the location of frame B expressed in the frame A. With the notation:

$$\hat{\boldsymbol{v}} = \begin{bmatrix} \boldsymbol{v} \\ 1 \end{bmatrix} \tag{3.17}$$

it is meant the addition of a unit element to a 3D vector $\boldsymbol{v}$, in order to be used for multiplication with $\mathbf{T}$ matrices.

Chapter 4

Space manipulator kinematics and dynamics

The mechanical system studied in this thesis is composed of a spacecraft platform on which robotic dexterous manipulators are mounted. The main objective consists in defining appropriate kinematic control commands that drive the joint motors in order to perform a trajectory-tracking manoeuvre, also called target-tracking manoeuvre, as illustrated in Fig. 4.1. As a specific property of the system, one recognizes that the motion of the manipulator and the motion of the spacecraft are not independent, due to action-reaction exchanges between the respective devices. This causes two relevant consequences on the control of a robotic arm:

1. a certain degree of coordination has to be undertaken for the whole systems in order for the manipulator end-effector to be able to reach a desired location in the inertial space;

2. the base reaction disturbance exerted by the manipulator on the base spacecraft during operation need to be managed in order to reduce the undesired dynamic effects on the spacecraft.

The first point have been well investigated in literature and can be tackled by means of Generalized Jacobian Matrices and sensory feedback control, while original contributions to the reaction disturbance control problem of the second are developed in this work for different operational conditions.

It is in fact an undesired effect that the motion of the manipulator exerts a disturbance on the spacecraft. As pointed out in the Introduction, a reaction disturbance on the base spacecraft that is generated during manipulator

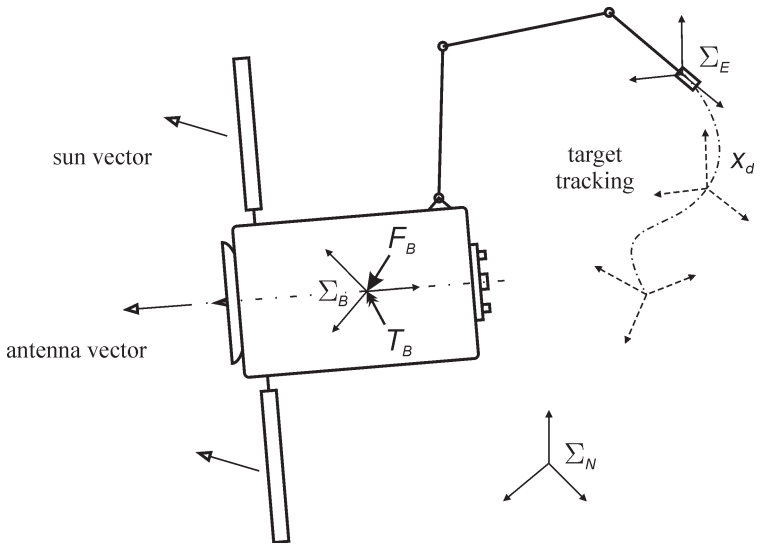

Figure 4.1: A spacecraft mounted manipulator during a target tracking manoeuvre, and the relevant vector references.

operation, is undesirable both because it may introduce S/C position and attitude disturbances, and because it leads to acceleration disturbances to the microgravity environment onboard the spacecraft or the space station.

Finally, the availability of control schemes that are suitable for on-line applications is also taken into account. This is an important requirement both for autonomy and teleoperation modes, if a non-repetitive task is carried out. In order to satisfy these requirement, one needs

1. appropriate models for system kinematics and dynamics;
2. a kinematic control framework;
3. appropriate algorithms and routines.

The systems is modeled as a multi-body chain composed of rigid bodies connected by ideal non-flexible joints, and the main purpose of this chapter is to give a description of these models. In order to be able to deal with reaction forces and torque quantities, the kinematic control is developed at the acceleration-level, and optimality-driven acceleration commands are derived thanks to the availability of a kinematic redundancy, common in existing space manipulators. The least squares mathematical framework completes the scheme for the optimization process.

4.1 Rigid body dynamics

The rigid body model represents the most significant model used to represent complex mechanical systems. In particular a robotic manipulator is often modeled as a multi-body chain of rigid bodies joined by 1-DOF kinematic joints. More accurate models that consider the influence of joints and links flexibilities are also matter of research in the robotic community, and can represent a future development of the proposed schemes.

Position, velocity, and acceleration Consider an *observation frame* $\vec{\Sigma}_c = \{O, \vec{c}_{c1}, \vec{c}_{c2}, \vec{c}_{c3}\}$ that can be imagined fixed to a camera. We want to describe the motion of a rigid body with respect to $\vec{\Sigma}_c$, i. e. the motion of any of its points P, ${}^c\boldsymbol{r}_P \triangleq (\vec{\Sigma}_c \cdot) \overrightarrow{OP}$. Consider also a *body frame* $\vec{\Sigma}_b = \{\Omega, \vec{c}_{b1}, \vec{c}_{b2}, \vec{c}_{b3}\}$ that moves with the body. If the motion of the body frame is known w.r.t. the observation frame, the actual position at time t of every point P of the rigid body, $\vec{r}_{OP} = \overrightarrow{OP}$ is known as well, since the relative positions of the material points of the body in the body frame ${}^b\boldsymbol{r}_P \triangleq (\vec{\Sigma}_b \cdot) \overrightarrow{\Omega P}$ are constant by definition of rigid body. The position of a point P with respect to a point O is

$$\vec{r}_{O,P} = \vec{r}_{O,\Omega} + \vec{r}_{\Omega,P} \tag{4.1}$$

Projected in the observation reference frames it becomes

$$\begin{aligned} {}^c\boldsymbol{r}_{O,P} &= {}^c\boldsymbol{r}_{O,\Omega} + {}^c\boldsymbol{r}_{\Omega,P} && (4.2)\\ &= {}^c\boldsymbol{r}_{O,\Omega} + ({}^c\boldsymbol{C}_b)\, {}^b\boldsymbol{r}_{\Omega,P} && (4.3)\\ &= ({}^c\mathbf{T}_b)\, {}^b\hat{\boldsymbol{r}}_{\Omega,P} && (4.4) \end{aligned}$$

Thus the motion of the rigid body can be completely characterized by the homogeneous matrix:

$${}^c\mathbf{T}_b = \begin{bmatrix} {}^c\boldsymbol{C}_b & {}^c\boldsymbol{r}_b \\ \mathbf{0}^{\mathrm{T}} & 1 \end{bmatrix} \tag{4.5}$$

Since a rigid body has 6 DOF, minimal representations of its location with 6-dimensional vectors are common. The difference arises in the representation of the orientation, for which different choices are possible. The most common representations are those due to Euler and called Euler angles, and quaternions (or Euler parameters), this latter has the advantage that it avoids representation singularity problems, but at the expence of an increased number of variables to 7. Denote by $\boldsymbol{\phi}_b$ the chosen attitude representation, the rigid body location vector $\boldsymbol{x}_b$ expressed in the observation reference frame is:

$${}^c\boldsymbol{x}_b = \begin{bmatrix} {}^c\boldsymbol{r}_b \\ {}^c\boldsymbol{\phi}_b \end{bmatrix} \tag{4.6}$$

In what follows, consider Euler angles and a 6-dimensional location vector without loss of generality.

The derivations of the rigid body position vector in an observation reference frame leads to its velocity and accelerations relative to that frame. Velocity is a relative entity and is associated to a reference frame with respect to which it is observed, or defined. This has nothing to do with the scalar representation of the vector in a given reference frame, in fact a velocity relative to a reference frame can be expressed in a second reference frame. To avoid confusion, the *velocity of a point* P with respect to a point Q is denoted as $\vec{v}_{Q,P}$ and defined as

$$\vec{v}_{Q,P} \triangleq \tfrac{\mathrm{d}}{\mathrm{d}t}\, \vec{r}_{Q,P} \tag{4.7}$$

The representation of a linear velocity vector $\vec{v}_{Q,P}$ in an observation reference frame $\vec{\Sigma}_c$ leads to a scalar representation

$$\begin{aligned} {}^c\boldsymbol{v}_{Q,P} &= (\vec{\Sigma}_c \cdot)\, \vec{v}_{Q,P} && (4.8)\\ &= {}^c\dot{\boldsymbol{r}}_{Q,P} && (4.9) \end{aligned}$$

Observe that all the quantities associated with the notion of velocity have a relative nature , such as the momentum and the kinetic energy. Now, the *angular velocity* of a rigid body b with respect to a relative orientation frame $\vec{C}_a$,[1] is defined by the *kinematic equations* of Poisson, as the vector $\vec{\omega}_{a,b}$, whose cross product with the unit vectors of the body frame gives their derivative

$$\tfrac{\mathrm{d}}{\mathrm{d}t}(\vec{C}_{a,b}) = \vec{\omega}_{a,b} \times \vec{C}_b \tag{4.10}$$

Notice that $\frac{\mathrm{d}}{\mathrm{d}t}(\vec{C}_{a,b})$ is the time derivative of the orientation frame $\vec{C}_b$ with respect to the observation frame $\vec{C}_a$. Projected in the observation frame $\vec{\Sigma}_c$, the scalar representations are obtained

$${}^c\dot{\boldsymbol{C}}_{a,b} = {}^c\boldsymbol{\omega}^{\times}_{a,b}\, {}^c\boldsymbol{C}_b \tag{4.11}$$

These can be inverted to give the angular velocity

$${}^c\boldsymbol{\omega}^{\times}_{a,b} = {}^c\dot{\boldsymbol{C}}_{a,b}\, {}^c\boldsymbol{C}_b^{\mathrm{T}} \tag{4.12}$$

and the components extracted $\boldsymbol{\omega} = [-\omega^{\times}_{23}, \omega^{\times}_{13}, -\omega^{\times}_{12}]^{\mathrm{T}}$. The complete symbol ${}^c\boldsymbol{\omega}_{a,b}$ represents the angular velocity *of* frame b, *with respect to* frame a, *expressed in* frame c. This discussion was useful in order to avoid confusion when some reference symbols are omitted in order to simplify the notation.

[1] A point of origin, or a complete relative reference frame, is not necessary for the definition of the angular velocity of a rigid body.

The time-derivative of the the location vector of a rigid body leads to:

$$ {}^c\dot{\boldsymbol{x}}_b = \begin{bmatrix} {}^c\dot{\boldsymbol{r}}_b \\ {}^c\dot{\boldsymbol{\phi}}_b \end{bmatrix} \tag{4.13} $$

This vector does not strictly represent a velocity for what concerns the orientation part, but the angular velocity can be derived from it depending on the particular representation. It is interesting to remind that for small displacements the difference between the angular velocity and the derivatives of any Euler-angle representation vanishes (see for example the discussion in Hughes [46]). An observation seems interesting about a possible notion of an *absolute angular velocity*. This concept has a dynamic character and is associated to the importance of inertial reference frames. It is known from Galilei that all the inertial frames, consider two of them $\vec{\Sigma}_{N_1}$ and $\vec{\Sigma}_{N_2}$, are relatively translating between each other and not rotating $\vec{\omega}_{N_1,N_2} = \vec{0}$, so the angular velocity of any inertial frame could be assumed for this reason as an absolute (dynamically) angular velocity and set to zero $\vec{\omega}_N = \vec{0}$.

The velocity vector field of a rigid body has interesting application in the screw theory, and was studied by Mozzi and reproposed by Chasles:

$$ \vec{v}_{A,P} = \vec{v}_{A,Q} + \vec{\omega}_{a,b} \times \vec{r}_{Q,P} \tag{4.14} $$

The velocity field of a rigid body is then completely determined by the linear velocity of a point and the angular velocity of the rigid body. At each time instant there is an axis in the body space which point have the same minimum velocity, called velocity of translation, and this axis is called *spin axis*, or *axis of Mozzi*, parallel to the angular velocity vector.

Without further details on the reference frames, for what concerns the acceleration field of a rigid body, we give the expression of the second derivative of the location vector:

$$ {}^c\ddot{\boldsymbol{x}}_b = \begin{bmatrix} {}^c\ddot{\boldsymbol{r}}_b \\ {}^c\ddot{\boldsymbol{\phi}}_b \end{bmatrix} \tag{4.15} $$

Relations analogous to the velocity vector can be derived and are available in the literature [47, 46].

Forces and Torques Forces and torques applied to a rigid body, can be usually modeled as

1. concentrated forces $\vec{f}_i = \vec{f}(\vec{r}_i)$, and torques $\vec{t}_i = \vec{t}(\vec{r}_i)$, acting at their application point P_i of position $\vec{r}_i$;
2. a continuous surface force field $\vec{f}_S = \vec{f}(\vec{r})\,\mathrm{d}r^2$, and torque field $\vec{t}_S = \vec{t}(\vec{r})\,\mathrm{d}r^2$, applied in a (at least) a region of the external surface of the body, such as contact forces;

3. a continuous volume force field $\vec{f}_V = \vec{f}(\vec{r})\,\mathrm{d}r^3$, and torque field $\vec{t}_V = \vec{t}(\vec{r})\,\mathrm{d}r^3$, applied in (at least) a region of the volume of the body, such as gravitational forces;

Observe that a concentrated force $\vec{f}_P$ applied to a point P, produces a concentrated torque about a point Ω of value $\vec{t}_\Omega = \vec{r}_{\Omega,P} \times \vec{f}_P$, by definition of torque as the moment of a force vector about a point. The same happens for force fields, that may produce a torque about a point. Torque fields are less useful than force fields in order to model physical interactions. Now, the motion of a rigid body subject to external forces $\vec{f}_i$ and torques $\vec{t}_i$, does not depend by the forces distribution or nature, but only by the resultant forces and torques. The resulant force acting on the rigid body b at the time t is defined as the sum of all the forces acting on the body

$$\vec{F}^b = \sum_i \vec{f}_i + \int_{S_b} \vec{f}_S\,\mathrm{d}r^2 + \int_{V_b} \vec{f}_V\,\mathrm{d}r^3 \tag{4.16}$$

The resultant torque *about a point* Ω is defined as the sum of all the external torques interacting with the body. Since the torque is defined as the moment of a force vector about a point, the point of evaluation of the torque, say Q, must be specified.

$$\vec{T}^b_Q = \sum_i \vec{t}_i + \int_{S_b} \vec{t}_S\,\mathrm{d}r^2 + \int_{V_b} \vec{t}_V\,\mathrm{d}r^3 \tag{4.17}$$

While the resultant force is a given vector, the resultant torque about a point depends on the point according to the following law, due to Poinsot:

$$\vec{T}_P = \vec{T}_Q + \vec{F} \times \vec{r}_{Q,P} \tag{4.18}$$

The equation is dual to the rigid-motion velocity field of Eq. (4.14). These similarities are exploited in the development of *screw theory*, where a rigid velocity field is said to be a *twist* on a screw, while the torque field is said to be a *wrench* on a screw. An axis exists about which the torques are minimal, called Poinsot axis, and dual to the spin axis of Mozzi for the velocity field.

Forces and torques can again be described in different frames, such as the body-frame, in which we have ${}^b\boldsymbol{F} = (\vec{\Sigma}_b \cdot)\,\vec{F}$ and ${}^b\boldsymbol{T}_Q = (\vec{\Sigma}_b \cdot)\,\vec{T}_Q$, or an inertial-frame, in which the projections lead to ${}^N\boldsymbol{F} = (\vec{\Sigma}_N \cdot)\,\vec{F}$ and ${}^N\boldsymbol{T}_Q = (\vec{\Sigma}_N \cdot)\,\vec{T}_Q$. Different representation can be useful depending on the applications, for example body-referenced quantities can be directly compared to the data form body-mounted instrumentation.

Laws of motion The interaction between the external solicitation to the body, and its kinematic evolution in time, is expressed by the laws of motion, usually addressed as Newton-Euler equations of motion for a rigid body.

Before presenting the expression for the equations of motion, we give the definition of *linear momentum* of a rigid body as the resultant of all the linear momenta of its points:

$$\vec{p}^{\,b} = \int_{V_b} \rho\, \vec{v}\, \mathrm{d}r^3 \tag{4.19}$$

and *angular momentum* of a rigid body as the resultant of all the angular momenta of its points, that results to be:

$$\vec{h}^{\,b}_Q = \int_{V_b} (\vec{r} - \vec{r}_Q) \times \rho\, \vec{v}\, \mathrm{d}r^3 \tag{4.20}$$

The specification of the reference frame relies on the discussion for velocities. The equations of motion for a rigid body, are:

$$\begin{cases} \vec{F}^b = \frac{\mathrm{d}}{\mathrm{d}t}\, \vec{p}^{\,b} \\ \vec{T}^b_Q = \vec{v}_Q \times \vec{p}^{\,b} + \frac{\mathrm{d}}{\mathrm{d}t}\, \vec{h}_Q \end{cases} \tag{4.21}$$

By expressing the body momenta in terms of velocities, projecting the equations in the body reference frame $\vec{\Sigma}_b$, and evaluating the velocity of the body center of mass CM and the torque about the body CM, we obtain the Newton-Euler equations of motion

$$\begin{cases} \boldsymbol{F}^b = m_b\, \dot{\boldsymbol{v}}^b_{\mathrm{CM}} \\ \boldsymbol{T}^b_{\mathrm{CM}} = \boldsymbol{I}^b_{\mathrm{CM}}\, \dot{\boldsymbol{\omega}}_b + \boldsymbol{\omega}_b \times \boldsymbol{I}^b_{\mathrm{CM}}\, \boldsymbol{\omega}_b \end{cases} \tag{4.22}$$

The first equation is also known as equation of Newton for a rigid body, while the second is known as equation of Euler for a rigid body. The inertial quantities in this equations are the mass of the body $m = \int_{V_b} \rho \mathrm{d}r^3$ and its tensor of inertia about the center of mass, expressed in the body reference frame, $\boldsymbol{I}^b_{\mathrm{CM}} = \int_{V_b} (r^2\, \mathbf{1} - \boldsymbol{r}\boldsymbol{r}^{\mathrm{T}})\, \rho\, \mathrm{d}r^3$.

4.2 Spacecraft-manipulator system

A system composed of a spacecraft and a manipulator can be modeled as an open chain of rigid-body systems for our purposes. The subsystems of the spacecraft and the manipulator are dinamically coupled, and the coupling problem have been extensively studied in literature [12]. In the following, the spacecraft base and its reference frame is denoted by the index B, an external Newtonian inertial frame by the symbol N, and the end-effector frame by the symbol E.

Given an n-DOF manipulator with n joints represented in the joint position variable $\boldsymbol{\theta}$, the overall system have $6+n$ DOF. Since in the free-floating

condition that is analyzed in this work, we are interested in maneuvering the system by means of the only arm joints, it was an important the demonstration that it's possible to express the spacecraft location variables in terms of the manipulator joint varibles or their derivatives. In particular, by means of the equation of the system center of mass, it is possible to express the spacecraft CM-position in terms of the arm joints position:

$$\boldsymbol{r}_B = \boldsymbol{k}_r(\boldsymbol{\theta}) \tag{4.23}$$

and by means of the system momenta by the substitution of the base position by means of the previous relation, the base angular velocity can be expressed in terms of the base attitude, the joint positions and velocities

$$\boldsymbol{\omega}_B = \boldsymbol{J}_B \, \dot{\boldsymbol{\theta}} \tag{4.24}$$

The base attitude Jacobian matrix is a function of base attitude and joint positions $\boldsymbol{J}_B = \boldsymbol{J}_B(\boldsymbol{\phi}_B, \boldsymbol{\theta})$. The non-integrability of the angular momentum equation that leads to this expression, is the origin of the non-holonomic characteristic of this system.

4.3 Manipulator kinematics

A space manipulator can be employed in order to perform a trajectory-tracking about the spacecraft frame $\vec{\Sigma}_B$, as for example when moving parts on the station or preforming maintenance operations on the spacecraft, or it can be employed in order to perform a trajectory-tracking manoeuvre in the inertial space $\vec{\Sigma}_N$, for example when capturing a floating object or berthing with a target satellite. For this reason they are of interest both the base-referenced kinematics, and the inertially-referenced kinematics. In what follows, $\vec{x}$ is the end effector location vector.

Base referenced kinematics The description of the end-effector location in the spacecraft reference frame ${}^B\boldsymbol{x}$ provides the traditional robot kinematics description of terrestrial manipulators. The kinematic relations between the end-effector location and the joint variables can be carried out leading to the forward kinematics equation:

$${}^B\boldsymbol{x} = \boldsymbol{k}_B(\boldsymbol{\theta}) \tag{4.25}$$

Its derivative leads to the velocity-level forward kinematics, and to definition of the spacecraft referenced Jacobian matrix of the manipulator ${}^B\boldsymbol{J} = \frac{\partial \boldsymbol{k}_B}{\partial \boldsymbol{\theta}}$, also known in literature as Fixed Base Jacobian (FJM), or manipulator

Jacobian matrix, since its determination does not depend on the spacecraft variables but on the only manipulator itself:

$$^{B}\dot{\boldsymbol{x}} = {}^{B}\boldsymbol{J}\,\dot{\boldsymbol{\theta}} \tag{4.26}$$

The FJM is a function of the actual configuration of the manipulator $^{B}\boldsymbol{J} = {}^{B}\boldsymbol{J}(\boldsymbol{\theta})$. It can be interpreted as a linear mapping between the actual joint velocities $\dot{\boldsymbol{\theta}}$ and the corresponding end-effector velocity vector $^{B}\dot{\boldsymbol{x}}$, as expressed in the base spacecraft reference frame. A second derivation provides the acceleration-level forward kinematics in the form

$$^{B}\ddot{\boldsymbol{x}} = {}^{B}\boldsymbol{J}\,\ddot{\boldsymbol{\theta}} + {}^{B}\dot{\boldsymbol{J}}\,\dot{\boldsymbol{\theta}} \tag{4.27}$$

Inertially referenced kinematics On the other side, the description of the end-effector location in the inertial reference frame $^{N}\boldsymbol{x}$ is characteristic of manipulators mounted on a free-floating base, and the kinematic relations are coupled with the spacecraft dynamics. The manipulator position-level forward kinematics leads to an expression of the form

$$^{N}\boldsymbol{x} = \boldsymbol{k}_{N}(\boldsymbol{\phi}_{B}, \boldsymbol{\theta}) \tag{4.28}$$

Where $\boldsymbol{\phi}_{B}$ represents the spacecraft attitude vector variable. Notice that the spacecraft position variables are not involved since they can be resolved by means of Eq. (4.23). The derivation of the previous relations lead to the velocity-level forward kinematics, and to the definition oof the inertially referenced Jacobian matrix, known in literature as Generalized Jacobian Matrix (GJM), introduced by Papadopoulos and Dubowsky, $^{N}\boldsymbol{J} = \frac{\partial\,\boldsymbol{k}_{N}}{\partial\,(\boldsymbol{\phi}_{B},\boldsymbol{\theta})}$, such that:

$$^{N}\dot{\boldsymbol{x}} = {}^{N}\boldsymbol{J}\,\dot{\boldsymbol{\theta}} \tag{4.29}$$

The GJM depends on the manipulator configuration and on the spacecraft orientation $^{N}\boldsymbol{J} = {}^{N}\boldsymbol{J}(\boldsymbol{\phi}_{B}, \boldsymbol{\theta})$, but it does not depend on the base velocity, since it has been resolved thanks to Eq. (4.24). For this reason the GJM still maps the actual joint velocities $\dot{\boldsymbol{\theta}}$ to the actual end-effector velocity vector $^{N}\dot{\boldsymbol{x}}$, expressed in the inertial reference frame. A second derivation of the forward kinematics equations provides the acceleration-level forward kinematics equations for the free-floating condition:

$$^{N}\ddot{\boldsymbol{x}} = {}^{N}\boldsymbol{J}\,\ddot{\boldsymbol{\theta}} + {}^{N}\dot{\boldsymbol{J}}\,\dot{\boldsymbol{\theta}} \tag{4.30}$$

The acceleration-level kinematics equations presented in this paragraph represent the kinematic model of the system that will be used for the developement of the kinematic control. It should be noticed the formal similarities between the base-referenced kinematics expressions and the inertially-referenced kinematics.

4.4 Manipulator dynamics

From the dynamics point of view, a space manipulator exhibits two significant relations. The first corresponds to the dynamics equations that provide the relation between the arm motion and the joint torques $\boldsymbol{\tau}$. The second and most important in this framework are the dynamics equations that provide the relation between the arm motion and the reaction forces $\boldsymbol{F}_B$ and torques $\boldsymbol{T}_B$ exerted to the base during the manoeuvre, and evaluated with respect to the base spacecraft center of mass, CM.

Joint Torques Dynamics Neglect interaction forces at the end-effector and gravitational forces that are not of interest in this context. The traditional equations of motion of terrestrial manipulator can be expressed in the well known second-oorder system of the form:

$$\boldsymbol{\tau} = \boldsymbol{H}_B\,\ddot{\boldsymbol{\theta}} + \boldsymbol{c}_B \tag{4.31}$$

The mass matrix depends on the joint positions $\boldsymbol{H}_B = \boldsymbol{H}_B(\boldsymbol{\theta})$ while the nonlinear-velocity term depends on the joints positions and velocities $\boldsymbol{c} = \boldsymbol{c}(\boldsymbol{\theta}, \dot{\boldsymbol{\theta}})$. Also for the dynamics model, a structural similarity occurs for the free-floating base manipulator, in which the joint torques dynamics equations take the form of Eq. (4.32):

$$\boldsymbol{\tau} = \boldsymbol{H}_N\,\ddot{\boldsymbol{\theta}} + \boldsymbol{c}_N \tag{4.32}$$

but in which the mass matrix $\boldsymbol{H}_N = \boldsymbol{H}_N(\boldsymbol{\theta}, \boldsymbol{\phi_B})$ and the non-linear velocity term $\boldsymbol{c}_N = \boldsymbol{c}(\boldsymbol{\phi}_B, \boldsymbol{\theta}, \dot{\boldsymbol{\theta}})$ depend also on the base attitude.

Base reactions dynamics Consider reaction forces $\vec{F}_B$ and torques $\vec{T}_B$ exherted by the manipulator on the supporting base, and their epression in the base reference frame, $\boldsymbol{F}_B = (\vec{\Sigma}_B \cdot)\,\vec{F}_B\cdot$ and $\boldsymbol{T}_B = (\vec{\Sigma}_B \cdot)\vec{T}_B$. For reaction forces $\boldsymbol{F}_B$, they can be expressed at the acceleration-level in the form:

$$\boldsymbol{F}_B = \boldsymbol{M}_F\,\ddot{\boldsymbol{\theta}} + \boldsymbol{n}_F \tag{4.33}$$

similarly, for reaction torques $\boldsymbol{T}_B$, they can be expressed at the acceleration-level in the form:

$$\boldsymbol{T}_B = \boldsymbol{M}_T\,\ddot{\boldsymbol{\theta}} + \boldsymbol{n}_T \tag{4.34}$$

These expressions are directly related to the disturbance motion of the base spacecraft through the motion Eq. (4.22). Also in this case, the dependence on the base attitude variable is necessary for the free-floating base robot. As it will be explained in the foregoing chapters, the objective of the study is the optimization of a base reaction cost function $f_R(\ddot{\boldsymbol{\theta}})$. For this reason, it is convenient to define a *weighted base reaction vector* $\boldsymbol{R}$ as a weighted

combination of reaction forces and torques by means of a weighting matrix $\boldsymbol{W}$:

$$\boldsymbol{R} \triangleq \boldsymbol{W} \begin{bmatrix} \boldsymbol{F}_B \\ \boldsymbol{T}_B \end{bmatrix} = \begin{bmatrix} \boldsymbol{W}_F & 0 \\ 0 & \boldsymbol{W}_T \end{bmatrix} \begin{bmatrix} \boldsymbol{F}_B \\ \boldsymbol{T}_B \end{bmatrix} \tag{4.35}$$

The dynamics equations of the base reactions can be summarized with the weighted reaction vector in the equations

$$\boldsymbol{R} = \boldsymbol{M}\,\ddot{\boldsymbol{\theta}} + \boldsymbol{n} \tag{4.36}$$

This expression allows to express the reaction wrench in a single vector. it is clear that for the fixed base manipulator, the mass matrix depends on the joint variables only $\boldsymbol{M} = \boldsymbol{M}(\boldsymbol{\theta})$, and the velocity terms depend on the joint variables and velocities $\boldsymbol{n} = \boldsymbol{n}(\boldsymbol{\theta}, \dot{\boldsymbol{\theta}})$, while for the free-floating base manipulator the mass matrix depends on the actual base attitude $\boldsymbol{M} = \boldsymbol{M}(\boldsymbol{\phi}_B, \boldsymbol{\theta})$, and so does the non-linear velocity term $\boldsymbol{n} = \boldsymbol{n}(\boldsymbol{\phi}_B, \boldsymbol{\theta}, \dot{\boldsymbol{\theta}})$. This equations complete the framework for the dynamics model of the system.

Chapter 5

Redundancy and dynamics optimization

In this chapter the general framework for kinematic control of space manipulator with optimal dynamic control of the base reactions is presented. The solutions to the inverse kinematics problem with base reaction control is provided making use of the manipulator redundancy that will be discussed in what follows. The least squares local optimization criteria are based in the general least squares methods discussed in Appendix A to which the reader is referred. Thanks to the structural similarities of the fixed base and free-floating base kinematics and dynamics models, the optimization framework can be developed in general form, and the use of reference indexes is avoided by purpose. The control logics developed in general form in this chapter, have then been tested for different fixed base and free base condition, as it will be presented in the foregoing chapters.

With *kinematic redundancy* it is traditionally meant the difference between the number of DOF of a manipulator, n, and the dimension of the kinematic task, k. Since the redundancy will be discussed also with respect to the dynamic task, of dimension d, it is convenient in this context to set a distinction between the *kinematic-task redundancy* and the *dynamic-task redundancy*.

Selection matrix and redundancy The manipulator has n independent joints controlled by the same number of motors, such that:

$$n = \dim(\boldsymbol{\theta}) \tag{5.1}$$

while the controlled variables are the end-effector trajectory, and the base reactions. The end-effector location is completely determined by at least 6 variables, of which $k \leq 6$ are under control in a defined kinematic task. A boolean selection matrix $\underset{k\times 6}{\boldsymbol{S}}$ can be defined for the purpose of isolating the controlled kinematic variables from the complete representation, this matrix is composed of elements in $\mathbb{B} = \{0, 1\}$, and generates a k-dimensional end-effector location vector:[1]

$$\boldsymbol{x}_{\mathrm{c}} = (\boldsymbol{S}_x)\,\boldsymbol{x} \tag{5.2}$$

such that

$$k = \dim(\boldsymbol{x}_{\mathrm{c}}) \tag{5.3}$$

The same concept can be applied to velocity $\dot{\boldsymbol{x}}$ and acceleration vector $\ddot{\boldsymbol{x}}$, and to the weighted reaction vector $\boldsymbol{R}$ as well, in order to define a controlled reaction vector of dimension d:

$$\boldsymbol{R}_{\mathrm{c}} = (\boldsymbol{S}_R)\,\boldsymbol{R} \tag{5.4}$$

Such that it becomes the dimension of the dynamic task

$$d = \dim(\boldsymbol{R}_{\mathrm{c}}) \tag{5.5}$$

Now that the control vectors have been defined, both with regards to the end-effector trajectory and the base reaction profile, the kinematic and dynamic task redundancy can be discussed. The degree of kinematic-task redundancy is defined as

$$r_{\mathrm{k}} \triangleq n - k \tag{5.6}$$

In this way, from a kinematic-task point of view it can be stated $n = k + r_{\mathrm{k}}$. Similarly, the degree of dynamic-task redundancy is defined as

$$r_{\mathrm{d}} \triangleq n - d \tag{5.7}$$

Similarly, from a dynamic-task point of view it can be stated $n = d + r_{\mathrm{d}}$. Where these values are non-positive, the corresponding redundancy vanishes, and the approximation problem can be undertaken, as will be discussed in the foregoing paragraphs, according to optimization criteria. As already observed, in order to simplify the notation, the distinction between the complete representation vectors, and the actually controlled vectors, will be stated only where necessary, and the symbols $\boldsymbol{x}$, and $\boldsymbol{R}$ are used.

[1] For example, a selection matrix that isolates the position vector $\boldsymbol{r}$ is given by $\boldsymbol{S}_r = \begin{bmatrix} 1 & 0 & 0 & 0 & 0 & 0 \\ 0 & 1 & 0 & 0 & 0 & 0 \\ 0 & 0 & 1 & 0 & 0 & 0 \end{bmatrix}$, and $\boldsymbol{r} = \boldsymbol{S}_r\,\boldsymbol{x}$. An analogous matrix can be defined to extract the orientation vector $\boldsymbol{\phi}$.

The two fundamental problems of *end-effector trajectory tracking*, and *base-reaction profile tracking* are now discussed, with respect to the available number of redundancies. The solution to this general problem represents the basis framework for the solution of the the different manipulator kinematics and dynamics problems in this work.

5.1 Acceleration level formulation

Traditionally, the resolution of kinematic redundancy of robot manipulators, have first been undertaken in literature at the velocity level. Among the first important works on the subject are due to Liégeois [48], who first derived a local gradient optimization method to resolve the kinematic redundancy at the velocity level, making use of the inversion of the first-order differential kinematics. The kinematic control resolution at the velocity level gave origin to the Resolved Motion Rate Control (RMRC), introduced by Whitney [49]. Nakamura et al. [50] reordered the kinematic control approach by means of the definition of task priorities. Several velocity level control schemes have been proposed in order to obtain the optimization of a wide variety of cost functions, depending on the specific application; a relatively recent survey can be found in [25]. The kinematic control have then been extended at the acceleration level by Luh et al. [24] that proposed the Resolved Acceleration Control (RAC).

Resolved acceleration control The kinematic control at the acceleration have been less investigated in literature, although it reveals more suitable in terms of modeling capabilities of interactions with the environment and for extension of the control schemes to more complex systems. The acceleration level approach allows the description of dynamic phenomena, such as forces, torques, vibrations, and in the same way it is appropriate for their control. Khatib [51] devised the difference in the two formulations characteristics, and called *kinematic approach* the treatment of a problem at the velocity-level, and *dynamic approach* the treatment at the acceleration-level. The redundancy resolution at the acceleration level, makes use of a cost function of the joint acceleration vector $g_{\mathrm{a}} = g_{\mathrm{a}}(\ddot{\boldsymbol{\theta}})$, while the position and velocity variables of $\{\boldsymbol{\phi}_B, \boldsymbol{\theta}, \dot{\boldsymbol{\theta}}\}$ are regarded as *state variables*, and are assumed available by instrumentation measurements or integration.

The problem is going to be investigated in detail in the following sections, with respect to different number of redundancies, different task-priorities, and optimization criteria. Two general tasks are considered, the kinematic, and the dynamic task. In particular here the second order differential kinematics of Eq.s (4.27) and (4.30) of the end-effector motion is considered:

$$\ddot{\boldsymbol{x}}(\ddot{\boldsymbol{\theta}}) = \boldsymbol{J}\,\ddot{\boldsymbol{\theta}} + \dot{\boldsymbol{J}}\,\dot{\boldsymbol{\theta}} \tag{5.8}$$

together with the base reactions dynamics (4.36):

$$\boldsymbol{R}(\ddot{\boldsymbol{\theta}}) = \boldsymbol{M}\,\ddot{\boldsymbol{\theta}} + \boldsymbol{n}\,. \tag{5.9}$$

For sake of generality, a desired end-effector trajectory is considered $\ddot{\boldsymbol{x}}_{\mathrm{d}} = \ddot{\boldsymbol{x}}_{\mathrm{d}}(t)$, and a desired base reaction profile as well $\boldsymbol{R}_{\mathrm{d}} = \boldsymbol{R}_{\mathrm{d}}(t)$. The minimization of two cost functions is investigated, the norm of the end-effector acceleration error:

$$g_x(\ddot{\boldsymbol{\theta}}) \triangleq \|\ddot{\boldsymbol{x}}(\ddot{\boldsymbol{\theta}}) - \ddot{\boldsymbol{x}}_{\mathrm{d}}\|^2 = e_{\ddot{x}}^2 \tag{5.10}$$

and the norm of the reaction error:

$$g_R(\ddot{\boldsymbol{\theta}}) \triangleq \|\boldsymbol{R}(\ddot{\boldsymbol{\theta}}) - \boldsymbol{R}_{\mathrm{d}}\|^2 = e_R^2 \tag{5.11}$$

Different redundancy conditions, task-priorities, and desired trajectories generate different optimal solutions.

5.2 Jacobian inverse and pseudoinverse

In this paragraph, it is shown how the inverse solution of the kinematics for a non-redundant manipulator is extended to pseudoinverse solution, for which two different interpretations are proposed.

Inverse kinematics problem Consider a non-redundant manipulator, such that

$$n = k \tag{5.12}$$

For this condition, and a full rank Jacobian matrix, the forward kinematics equation of Eq. (5.8) can be inverted towards a desired end-effector acceleration according to Eq. (A.5), leading to the solution of the target-tracking problem $\ddot{\boldsymbol{x}}(\ddot{\boldsymbol{\theta}}) = \ddot{\boldsymbol{x}}_{\mathrm{d}}(t)$, in the form

$$\ddot{\boldsymbol{\theta}} = \boldsymbol{J}^{-1}(\,\ddot{\boldsymbol{x}}_{\mathrm{d}} - \dot{\boldsymbol{J}}\,\dot{\boldsymbol{\theta}}\,) \tag{5.13}$$

This gives a representation of the unique solution of the inverse kinematics problem in differential form, if the tracking problem is feasible and a solution exists.

Least squares kinematics problems The approach adopted, for $n \neq k$ extends the use of the kinematic Jacobian pseudoinverse solution, that is expressed in the well known acceleration-level formulation as:

$$\ddot{\boldsymbol{\theta}} = \boldsymbol{J}^{\dagger}(\,\ddot{\boldsymbol{x}}_{\mathrm{d}} - \dot{\boldsymbol{J}}\,\dot{\boldsymbol{\theta}}\,) \tag{5.14}$$

also known as Least Squares (LS) solution, according to (A.7) and (A.8). The interpretation of this solution, depends on the available number of redundancies, according to the discussion in Appendix A. If no kinematic redundancy is available, this solution is equivalent to the Jacobian inverse solution in (5.13), since in this case $\boldsymbol{J}^{\dagger} = \boldsymbol{J}^{-1}$.

Where the number of redundancies is different to the dimension of the tracking task, the existence of a unique solution is generally not available. In the condition for which a solution does not exist, it's interesting to determine a best approximation solution, while if infinite solutions exit, optimization criteria may be used. Consider a *kinematic deficiency* condition for which

$$n < k \tag{5.15}$$

In this situation it is not possible in general for the robot to track any desired trajectory. The LS solution gives the best approximation of the acceleration profile in a least squares sense $\ddot{\boldsymbol{x}}(\ddot{\boldsymbol{\theta}}) \cong \ddot{\boldsymbol{x}}_{\mathrm{d}}(t)$, minimizing the acceleration error $g_x = \ddot{e}_x^2$, and being the solution to the problem

$$\boldsymbol{J}\,\ddot{\boldsymbol{\theta}} + \dot{\boldsymbol{J}}\,\dot{\boldsymbol{\theta}} \cong \ddot{\boldsymbol{x}}_{\mathrm{d}}(t) \tag{5.16}$$

in the joint acceleration unknown $\ddot{\boldsymbol{\theta}}$.

On the other side, for the *kinematic redundancy* condition

$$n > k \tag{5.17}$$

the LS solution of Eq. (5.14) represents the target tracking $\ddot{\boldsymbol{x}}(\ddot{\boldsymbol{\theta}}) = \ddot{\boldsymbol{x}}_{\mathrm{d}}(t)$ solution of minimum joint acceleration norm $\ddot{\boldsymbol{\theta}} \cong \mathbf{0}$, solution to the explicit problem

$$\begin{cases} \boldsymbol{J}\,\ddot{\boldsymbol{\theta}} + \dot{\boldsymbol{J}}\,\dot{\boldsymbol{\theta}} &= \ddot{\boldsymbol{x}}_{\mathrm{d}}(t) \\ \ddot{\boldsymbol{\theta}} &\cong \mathbf{0} \end{cases} \tag{5.18}$$

This dual interpretation of the pseudoinverse solution was not well evidenced in the robotics literature.

5.3 Extended Jacobian inverse and pseudoinverse

The previous relations are now extended to the tracking of a kinematic and a dynamic trajectory, and the available solutions examined.

Extended inverse kinematics and dynamics problem Consider now a manipulator with a number of kinematic redundancies exactly equal to the dimension of the dynamic task, such as

$$n = k + d \tag{5.19}$$

For this special condition, the tracking problem for an end-effector trajectory $\ddot{\boldsymbol{x}}(\ddot{\boldsymbol{\theta}}) = \ddot{\boldsymbol{x}}_{\mathrm{d}}(t)$ *and* a base reaction profile $\boldsymbol{R}(\ddot{\boldsymbol{\theta}}) = \boldsymbol{R}_{\mathrm{d}}(t)$ can be investigated, and the solution, if exists, is unique. Making the kinematics and dynamics equations explicit in the joint variables, the problem can be stated in a linear system formulation:

$$\left\{ \begin{array}{rcl} \boldsymbol{J}\,\ddot{\boldsymbol{\theta}} + \dot{\boldsymbol{J}}\,\dot{\boldsymbol{\theta}} & = & \ddot{\boldsymbol{x}}_{\mathrm{d}}(t) \\ \boldsymbol{M}\,\ddot{\boldsymbol{\theta}} + \boldsymbol{n} & = & \boldsymbol{R}_{\mathrm{d}}(t) \end{array} \right. \tag{5.20}$$

The solution, if it exists, is given in the form of an *extended* (or *augmented*) Jacobian formulation, as:

$$\ddot{\boldsymbol{\theta}} = \left[\begin{array}{c} \boldsymbol{J} \\ \boldsymbol{M} \end{array} \right]^{-1} \left[\begin{array}{c} \ddot{\boldsymbol{x}}_{\mathrm{d}} - \dot{\boldsymbol{J}}\,\dot{\boldsymbol{\theta}} \\ \boldsymbol{R}_{\mathrm{d}} - \boldsymbol{n} \end{array} \right] \tag{5.21}$$

It can be noticed that this solution is a natural extension of the simple inverse kinematics problem (5.13) to a an extended – non only kinematic – Jacobian matrix. The numeric implementation of this formulation, can be carried out by means of factorization or iterative methods.

Extended least squares kinematics and dynamics problems The previous relations are now extended to more general redundancy conditions, for which *tracking*, *approximation*, and *optimization* problems can be tackled. For the over-constrained dimensional condition of

$$n < k + d \tag{5.22}$$

one can investigate the meaning of the pseudoinverse solution of the extended Jacobian matrix, expresssed as:

$$\ddot{\boldsymbol{\theta}} = \left[\begin{array}{c} \boldsymbol{J} \\ \boldsymbol{M} \end{array} \right]^{\dagger} \left[\begin{array}{c} \ddot{\boldsymbol{x}}_{\mathrm{d}} - \dot{\boldsymbol{J}}\,\dot{\boldsymbol{\theta}} \\ \boldsymbol{R}_{\mathrm{d}} - \boldsymbol{n} \end{array} \right] \tag{5.23}$$

In fact, this problem has the same structure of Eq. (5.14), and in this case it provides the minimization of the cost function

$$g_{xR} \triangleq e_{\ddot{x}}^2 + e_R^2 \tag{5.24}$$

This observation suggests the introduction of weighting factors λ_x and λ_R in order to minimize a more convenient function of the form:

$$g_{\lambda} \triangleq \lambda_x\, e_{\ddot{x}}^2 + \lambda_R\, e_R^2 \tag{5.25}$$

The solution to this weighted-tasks problem results in the following original extended Jacobian expression:

$$\ddot{\boldsymbol{\theta}} = \left[\begin{array}{c} \lambda_x\,\boldsymbol{J} \\ \lambda_R\,\boldsymbol{M} \end{array} \right]^{\dagger} \left[\begin{array}{c} \lambda_x\,(\,\ddot{\boldsymbol{x}}_{\mathrm{d}} - \dot{\boldsymbol{J}}\,\dot{\boldsymbol{\theta}}\,) \\ \lambda_R\,(\,\boldsymbol{R}_{\mathrm{d}} - \boldsymbol{n}\,) \end{array} \right] \tag{5.26}$$

In order to complete the least squares framework robotic manipulators, the hyper-redundant condition for which

$$n > k + d \tag{5.27}$$

can lead to further optimization problems. Anyways, according to (A.27), the pseudoinverse solution (5.23) and (5.26) do minimize respectively the cost functions g_{xR} and g_λ with the minimum norm of the joint accelerations; they are the minimum norm least squares solutions.

5.4 Constrained least squares solutions

For the purposes of this work, it is of interest to investigate the feasibility of exact solutions and best approximations of kinematic-task and dynamic-task desired profiles.

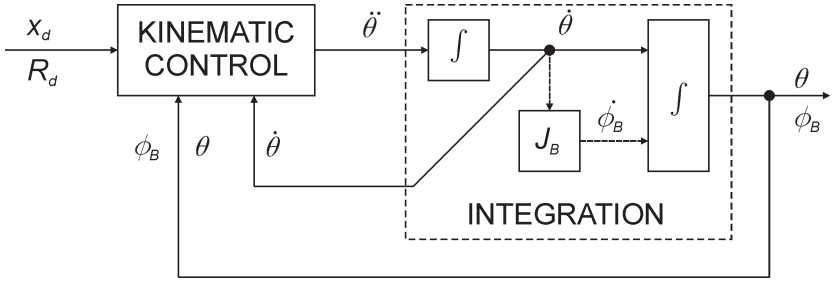

Figure 5.1: Kinematic control, implementation scheme.

LSE problem and solution The most significant problem is the tracking of a desired end-effector acceleration profile, with the simultaneous approximation of a desired base-reaction profile (i.e. the minimization of the reaction tracking error). The optimization problem setting leads to the Least Squares problem with Equality constraints (LSE), of the form:

$$\begin{cases} \boldsymbol{J}\,\ddot{\boldsymbol{\theta}} + \dot{\boldsymbol{J}}\,\dot{\boldsymbol{\theta}} &= \ddot{\boldsymbol{x}}_{\mathrm{d}}(t) \\ \boldsymbol{M}\,\ddot{\boldsymbol{\theta}} + \boldsymbol{n} &\cong \boldsymbol{R}_{\mathrm{d}}(t) \end{cases} \tag{5.28}$$

The kinematic-task equation represent the equality constraint, while the dynamic-task represent the optimization cost function. Its solution can be given by means of generalized inverses. According to A.23, the pseudoinverse formulation of the solution is

$$\ddot{\boldsymbol{\theta}} = \boldsymbol{J}^{\dagger}(\ddot{\boldsymbol{x}}_{\mathrm{d}} - \dot{\boldsymbol{J}}\,\dot{\boldsymbol{\theta}}) - (\boldsymbol{M}\boldsymbol{Z}_{J})^{\dagger}\,[\boldsymbol{M}\boldsymbol{J}^{\dagger}(\,\ddot{\boldsymbol{x}}_{\mathrm{d}} - \dot{\boldsymbol{J}}\,\dot{\boldsymbol{\theta}}\,) - (\,\boldsymbol{R}_{\mathrm{d}} - \boldsymbol{n}\,)] \tag{5.29}$$

This solution minimizes the error of the base reaction profile e_R^2. Now, the utilization of the weighting methods explained in Appendix A to this LSE problem, can be reformulated by means of the weighted extended Jacobian matrix of Eq. (5.26), setting the weight to $\mu = \frac{\lambda_x}{\lambda_R}$. A formal representation of the solution, can then be given by:

$$\ddot{\boldsymbol{\theta}} = \begin{bmatrix} \lambda_x \boldsymbol{J} \\ \lambda_R \boldsymbol{M} \end{bmatrix}^{\dagger} \begin{bmatrix} \lambda_x \left(\ddot{\boldsymbol{x}}_{\mathrm{d}} - \dot{\boldsymbol{J}}\,\dot{\boldsymbol{\theta}} \right) \\ \lambda_R \left(\boldsymbol{R}_{\mathrm{d}} - \boldsymbol{n} \right) \end{bmatrix} \qquad \text{for} \quad \frac{\lambda_x}{\lambda_R} \to \infty \tag{5.30}$$

The dual problem of tracking a trajectory profile while minimizing the

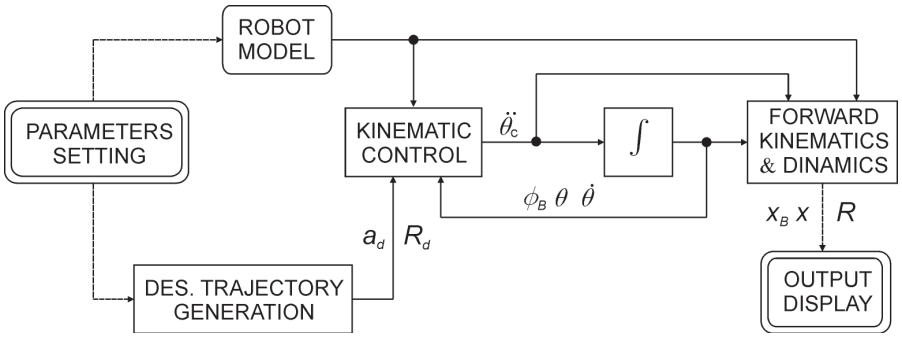

Figure 5.2: Robot simulator structure.

error of the achieved end-effector acceleration by exchanging the role of the kinematic and dynamic equations will be presented in Chapter 8. In the extended Jacobian formulation, this solution is provided by the condition of $\frac{\lambda_x}{\lambda_R} \to 0$.

LSEI problem and solution The LSE kinematics-dynamics problem, can be extended with the introduction of joint acceleration boundaries to the possible solutions. According to Appendix A, the problem can be formulated in the form:

$$\begin{cases} \boldsymbol{J}\,\ddot{\boldsymbol{\theta}} + \dot{\boldsymbol{J}}\,\dot{\boldsymbol{\theta}} = \ddot{\boldsymbol{x}}_{\mathrm{d}}(t) \\ \boldsymbol{M}\,\ddot{\boldsymbol{\theta}} + \boldsymbol{n} \cong \boldsymbol{R}_{\mathrm{d}}(t) \\ \bar{\ddot{\boldsymbol{\vartheta}}}_{\mathrm{l}} \leqslant \ddot{\boldsymbol{\theta}} \leqslant \bar{\ddot{\boldsymbol{\vartheta}}}_{\mathrm{u}} \end{cases} \tag{5.31}$$

The lower-bound and upper-bound inequalities are intended in a component-wise sense. The solution is addressed as:

$$\ddot{\boldsymbol{\theta}} = \mathrm{LSEI}(\boldsymbol{J}, (\ddot{\boldsymbol{x}}_{\mathrm{d}} - \dot{\boldsymbol{J}}\,\dot{\boldsymbol{\theta}}), \boldsymbol{M}, (\boldsymbol{R}_{\mathrm{d}} - \boldsymbol{n})) \tag{5.32}$$

The paradigms exposed in this chapter, have been implemented in a robot simulator for a 3-DOF manipulator mounted either on a on a fixed base or on a free-floating base. Fig. 5.1 represent the scheme of the kinematic

control block, and in Fig. 5.2 is represented the scheme of the complete robot simulator.

Chapter 6

Reaction control of a fixed base manipulator

In this chapter a robot manipulator mounted on a fixed base is considered and the *local minimization* of the base reactions exerted during target-tracking manoeuvres is investigated. It is assumed that the base frame $\vec{\Sigma}_B$ is also an inertial reference frame, such that the base referenced kinematics is considered together with the fixed base dynamics model as previously pointed out in Chapter 4. The FJM is used for the kinematic mapping since the desired end-effector trajectory is base referenced:

$$\boldsymbol{x} = {}^{B}\boldsymbol{x} \tag{6.1}$$

The manipulator has at least one kinematic redundancy, $n > k$, and the optimization cost function is the magnitude of the weighted reaction vector

$$g_R(\ddot{\boldsymbol{\theta}}) = \| \boldsymbol{R} \|^2 \tag{6.2}$$

After the development of the solution according to the optimization framework of Chapter 5, the kinematic law is studied by means of simulations and tested in an experimental 2D robot manipulator with 3-DOF, whose reaction forces and torques are dynamically retrieved by means of a custom design dynamometer. The results reported in this Chapter are under publication in [44] for the weighted reaction control, and are in press in [45] for the reaction torque control at the moment of writing.

6.1 Resolved joint accelerations

The solution of the local optimization problem can be given by means of the constrained least squares framework developed in Chapter 5, by setting the desired weighted reaction vector to zero

$$\boldsymbol{R}_{\mathrm{d}}(t) = \mathbf{0} \tag{6.3}$$

Observe that the minimization of the magnitude of the weighted reaction vector in a least squares sense, is the same problem of the least squares approximation of the zero weighted reaction vector. The equality constraint is provided by the kinematic tracking task, since it is necessary that the trajectory be exactly tracked.

LS solution the LS solution (5.14) is used for comparison with the proposed optimal solutions since it represents a common resolution scheme, together with its velocity-level counterpart. Its formulation is reminded here:

$$\ddot{\boldsymbol{\theta}} = \boldsymbol{J}^{\dagger}(\ddot{\boldsymbol{x}}_{\mathrm{d}} - \dot{\boldsymbol{J}}\,\dot{\boldsymbol{\theta}})$$

This is the pseudoinverse solution of minimum joint acceleration, since the manipulator is in an under-constrained kinematic redundancy condition.

Extended inverse solution In some cases ($n \geqslant k + d$) it is possible to achieve an exactly zero base reaction while performing a target tracking manoeuvre. If $n = k + d$ and without rank deficiency inconveniences, the inverse kinematics and dynamics problem can be tackled:

$$\left\{ \begin{array}{rcl} \boldsymbol{J}\,\ddot{\boldsymbol{\theta}} + \dot{\boldsymbol{J}}\,\dot{\boldsymbol{\theta}} & = & \ddot{\boldsymbol{x}}_{\mathrm{d}}(t) \\ \boldsymbol{M}\,\ddot{\boldsymbol{\theta}} + \boldsymbol{n} & = & \mathbf{0} \end{array} \right. \tag{6.4}$$

and the inverse solution results in the extended Jacobian formulation of Eq: (5.21):

$$\ddot{\boldsymbol{\theta}} = \left[\begin{array}{c} \boldsymbol{J} \\ \boldsymbol{M} \end{array} \right]^{-1} \left[\begin{array}{c} \ddot{\boldsymbol{x}}_{\mathrm{d}} - \dot{\boldsymbol{J}}\,\dot{\boldsymbol{\theta}} \\ -\boldsymbol{n} \end{array} \right] \tag{6.5}$$

LSE solution More generically, when $n > k$, the base reaction minimization problem can be reformulated in the LSE form as:

$$\left\{ \begin{array}{rcl} \boldsymbol{J}\,\ddot{\boldsymbol{\theta}} + \dot{\boldsymbol{J}}\,\dot{\boldsymbol{\theta}} & = & \ddot{\boldsymbol{x}}_{\mathrm{d}}(t) \\ \boldsymbol{M}\,\ddot{\boldsymbol{\theta}} + \boldsymbol{n} & \cong & \mathbf{0} \end{array} \right. \tag{6.6}$$

The pseudoinverse closed form solution of Eq. (5.29) formulation becomes:

$$\ddot{\boldsymbol{\theta}} = \boldsymbol{J}^{\dagger}(\ddot{\boldsymbol{x}}_{\mathrm{d}} - \dot{\boldsymbol{J}}\,\dot{\boldsymbol{\theta}}) - (\boldsymbol{M}\boldsymbol{Z}_{J})^{\dagger}\,[\boldsymbol{M}\boldsymbol{J}^{\dagger}(\,\ddot{\boldsymbol{x}}_{\mathrm{d}} - \dot{\boldsymbol{J}}\,\dot{\boldsymbol{\theta}}\,) + \boldsymbol{n}\,] \tag{6.7}$$

While the extended Jacobian formulation of the solution by weighting results in the form:

$$\ddot{\boldsymbol{\theta}} = \begin{bmatrix} \lambda_x \boldsymbol{J} \\ \lambda_R \boldsymbol{M} \end{bmatrix}^{\dagger} \begin{bmatrix} \lambda_x \left(\ddot{\boldsymbol{x}}_{\mathrm{d}} - \dot{\boldsymbol{J}}\,\dot{\boldsymbol{\theta}} \right) \\ \lambda_R \left(-\boldsymbol{n} \right) \end{bmatrix} \qquad \text{for} \quad \lambda_x \gg \lambda_R \tag{6.8}$$

LSEI soluton The LSEI solution with joint acceleration limits is considered as well and have been implemented for the simulation and test campaign. The problem is reformulated as:

$$\begin{cases} \boldsymbol{J}\,\ddot{\boldsymbol{\theta}} + \dot{\boldsymbol{J}}\,\dot{\boldsymbol{\theta}} = \ddot{\boldsymbol{x}}_{\mathrm{d}}(t) \\ \boldsymbol{M}\,\ddot{\boldsymbol{\theta}} + \boldsymbol{n} \cong \boldsymbol{0} \\ \ddot{\bar{\boldsymbol{\vartheta}}}_{\mathrm{l}} \leqslant \ddot{\boldsymbol{\theta}} \leqslant \ddot{\bar{\boldsymbol{\vartheta}}}_{\mathrm{u}} \end{cases} \tag{6.9}$$

While the solution is again addressed with the statement:

$$\ddot{\boldsymbol{\theta}} = \mathrm{LSEI}(\boldsymbol{J}, (\ddot{\boldsymbol{x}}_{\mathrm{d}} - \dot{\boldsymbol{J}}\,\dot{\boldsymbol{\theta}}), \boldsymbol{M}, -\boldsymbol{n}) \tag{6.10}$$

These kinematic control schemes have been tested by means of a robot simulator presented in Chapter 5, and validated with an experimental robot setup, described in the following section.

6.2 Experimental robot setup

The experimental setup [52] used to validate and test the kinematic control solutions of this work, consists of a robotic manipulator and a load cell designed in order to measure the base reactions. The manipulator is a 3 DOF planar arm suspended by air bearings over a flat granite plane in order to get rid of the gravitational effects and simulate the microgravity environment, as shown in Fig. 6.1. The manipulator is driven by DC servomotors and commanded by a Robox$^{\mathrm{TM}}$ RMC4 motion controller. The main geometric and inertial parameters of the arm are presented in Tab. 6.1.

The first joint, joint 1, of position variable θ_1, is connected to the dynamometer through a rigid flange; joint 2, of position variable θ_2, is the central joint, and joint 3, of position variable θ_3, is connected to the end-effector, whose tip describes the actual trajectory $\vec{x}$ in the Cartesian plane. The origin O of the Cartesian base reference frame $\vec{\Sigma}_B$ is set at the center of the dynamometer, at a distance of 0.087 m from the first joint axis, and in the *zero* configuration with all the links aligned the joint variable is set to zero $\boldsymbol{\theta} = \boldsymbol{0}$, the links are aligned to the x-axis, the z-axis is oriented normal to the motion plane, and the y-axis belongs to the motion plane and is oriented in order to form a right reference frame $\vec{\Sigma}_B$. All the quantities are expressed in this base frame.

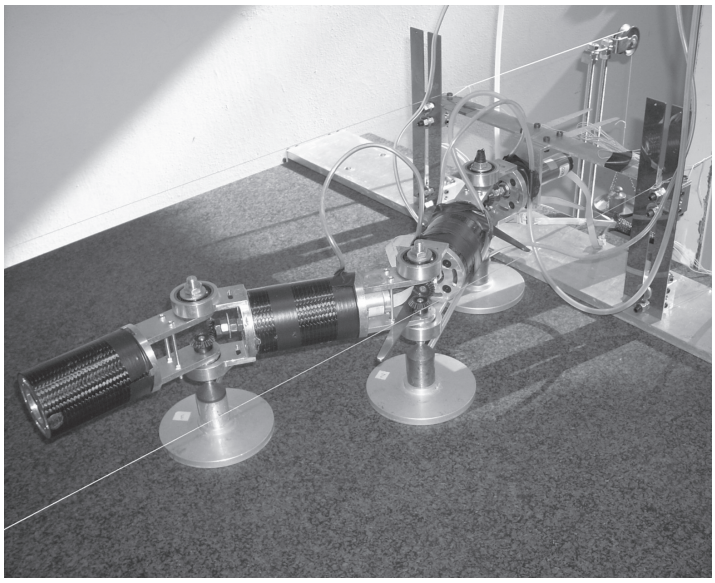

Figure 6.1: Experimental setup. The planar 3-DOF manipulator suspended by air bearings [52].

As shown in Fig. 6.2, the dynamometer is made of two polymeric beams of square cross section equipped with strain gauges connected in two Weathstone bridges that are connected to an ADC data acquisition system that sends the data to a computer for storage and analysis. The dynamometer can measure maximum forces of 1 N along the two axes with a resolution of $1.7 \cdot 10^{-3}$ N and an accuracy of $\pm 5.4 \cdot 10^{-2}$ N , and a maximum torque of 0.320 N-m with a resolution of $2.6 \cdot 10^{-4}$ N-m and an accuracy of $\pm 8.5 \cdot 10^{-}3$ N-m. The system have been designed in order to obtain the first eigenfrequency of the dynamometer be greater then 15 Hz. For further informations on the design details of the robotic arm and the instrumentation see the doctorate thesis of Cocuzza in [52], and in [53, 54].

6.3 Weighted reactions minimization

A test campaign have been carried out by simulation and validated by experiments, showing that the proposed kinematic control environment presents appealing performances in terms of dynamic disturbance minimization and kinematics-to-dynamics task priority attribution capabilities. The simulator code have been implemented in Matlab^{TM}, and models the experimental robot manipulator my means of a multi rigid-body open chain, such

Property	Link 1	Link 2	Link 3
l [m]	0.176	0.176	0.135
l_G [m]	0.115	0.115	0.056
m [kg]	0.615	0.615	0.200
I_{Gx} [kg-m^2]	$2.43 \cdot 10^{-4}$	$2.43 \cdot 10^{-4}$	$1.21 \cdot 10^{-4}$
I_{Gy} [kg-m^2]	$2.73 \cdot 10^{-3}$	$2.73 \cdot 10^{-3}$	$1.24 \cdot 10^{-3}$
I_{Gz} [kg-m^2]	$2.73 \cdot 10^{-3}$	$2.73 \cdot 10^{-3}$	$1.24 \cdot 10^{-3}$

Table 6.1: Experimental robot geometrical and inertial properties.

as there is a correspondence between the mathematical models in the kinematic control, the simulation models, and the experimental setup. A flexible joints model have also been implemented in Adams$^{\text{TM}}$, in order to asses the possibility to interpret the differences between the Matlab model and the experimental results in terms of joint flexibility [52].

Trajectory tracking tests

Here we present the results for a trajectory tracking of a circular path of diameter $D = 0.100$ m. All the tests are performed starting from the same initial configuration:

$$\boldsymbol{\theta}_0 = [-0.20,\ 0.60,\ -0.54]^{\text{T}} \text{ rad} \tag{6.11}$$

This initial configuration is used in all the test presented in this thesis in order to be compared between each others. The desired path is described with a smooth motion law $s = s(t)$, which has been designed as a combination of sinusoid functions, in order to be free of discontinuities up to the jerk-level, as illustrated in Fig. 6.3 for a general condition. This is a requirement for many space application operations, and is also useful in the experimental campaign in order to reduce vibration disturbances that may affect the analysis. The motion law can be scaled according to a desired path length L and a desired period T in which the trajectory is performed. For the tests presented in this paragraph, the circular path is described in a period of $T = 3$ s, which results in an appropriate speed in order to allow an accurate evaluation of the base reactions according to the available instrumentation setup. Slower motion tests more similar to space operation manoeuvres, will

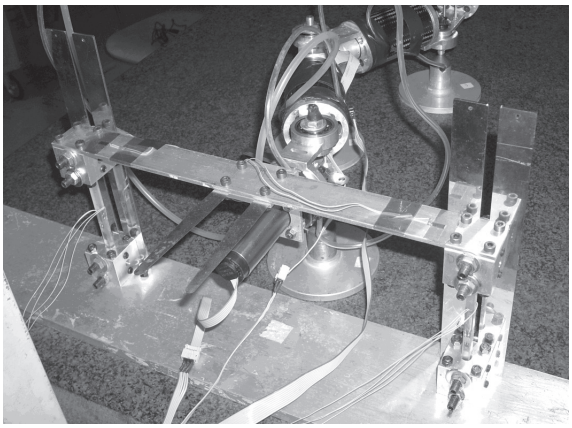

Figure 6.2: Base reaction forces and torque transducer [52].

be presented for the free-floating robot, for which a simulation campaign is carried out. The desired end-effector trajectory is a 2-dimensional vector

$$\boldsymbol{x} = \begin{bmatrix} x \\ y \end{bmatrix} \tag{6.12}$$

leaving one kinematic redundancy, while all the base reactions are controlled

$$\boldsymbol{R} = \begin{bmatrix} w_{Fx} & 0 & 0 \\ 0 & w_{Fy} & 0 \\ 0 & 0 & w_{Tz} \end{bmatrix} \begin{bmatrix} F_x \\ F_y \\ T_z \end{bmatrix} \tag{6.13}$$

And thus the task dimensions involved are:

$$k = 2 \qquad d = 3 \tag{6.14}$$

The selected weights used in the test campaign that form the diagonal reaction weight matrix $\boldsymbol{W}$ are:

$$w_{Fx} = 0.05 \text{ N}^{-1} \quad w_{Fy} = 0.30 \text{ N}^{-1} \quad w_{Tz} = 0.65 \text{ N}^{-1}\text{m}^{-1} \tag{6.15}$$

A parametric study on the influence of weights will also be presented.

The implementation of an LS solution RAC control by means of Eq. (5.14) results in the motion illustrated in Fig. 6.4, where also the evolution of the joint angles is shown. The base reactions retrieved by measurements are compared to the reactions obtained by simulation, as illustrated in Fig. (6.5), showing a good accordance between the model predictions and the experimental profiles. Follows the solution with a RAC control based on the

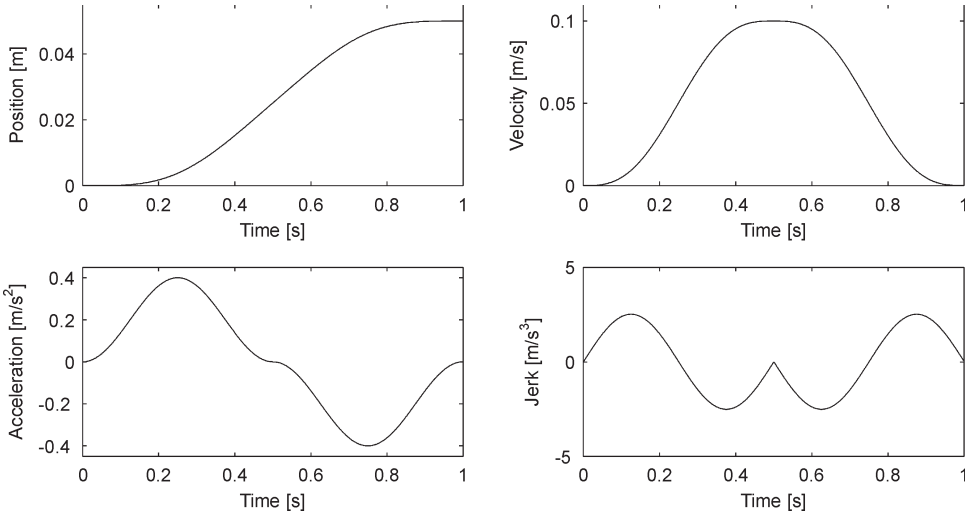

Figure 6.3: Smooth end effector motion law $s = s(t)$ and its derivatives, as used in the trajectory tracking tests. Here normalized to $T = 1$ s, and for an arc length of $L = 5$ cm.

optimal LSE solution of Eq. (6.7), illustrated in Fig. 6.6. The correspondent base reaction profiles are reported in Fig. 6.7, from which it can be observed the significant reduction on the single base reaction components. After the LSE solution, a lower and upper acceleration limits have been introduced in the solution of value ± 8.73 rad/s^2 for all the joints. The introduction of joint acceleration limits is accounted by means of the LSEI solution of Eq. (6.10). The motion of the LSEI kinematic RAC, is illustrated in Fig. 6.8. The resulting simulation and experimental base reactions are reported in Fig. 6.9. It can be noticed a slight increase in the base reaction values of the LSEI solution compared to the LSE solution already with the introduction of a small acceleration constraint. This is due to the fact that once an acceleration limit is reached, the available effective kinematic redundancy actually vanishes and is not available any longer in order to perform the optimization, until the acceleration bound is left. The weighted reaction cost function for the three resolutions is compared in Fig. 6.10 for the simulations and the experiments, showing a reduction of 72.0% in the peak force between LSE and LS, and a reduction of 46.6% between LS ans LSEI the rigid joints *simulations*. The performances of the *experimental* tests are similar, with a reduction of 71.4% in the peak force between LSE and LS, and a reduction of 61.4% between LS ans LSEI that results even better in perfor-

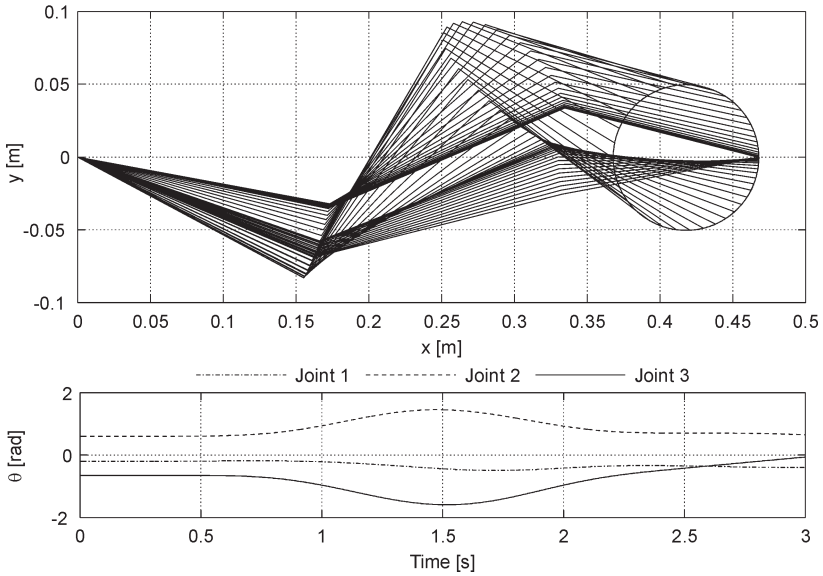

Figure 6.4: Stroboscopic plot and joint angle profiles for the LS resolution.

mance to the rigid case, thanks to the damping provided by joints flexibilities when the acceleration limits become active. It is important to observe that the reaction minimization provided by the LSE solution, is obtained at the expence of a higher joint duty, since the required joint accelerations are significantly higher then those of the LS solution, as can be noticed in Fig. 6.11. In Fig. 6.11 are reported the joint acceleration command solutions for the three cases, and over imposed for comparison. It can be noticed that the LSE and LSEI solutions are equivalent until a joint limit becomes active. In this region, the base reaction cost function relative to the LSEI solution begins to increase, according to Fig. 6.10. Acceleration limits are reached for joints 2 and 3, for which a joint acceleration space projection is reported in Fig. 6.12. An insight on the influence of the joint acceleration limits on the minimization performances of the proposed control will be illustrated in the following paragraph.

Parametric studies

In this paragraph we present some parametric simulation studies, in order to provide a better understanding on the influence of significant quantities in the performances of the algorithms. In particular, we consider 1) the influence of acceleration limits, 2) the influence of a different mass and inertia

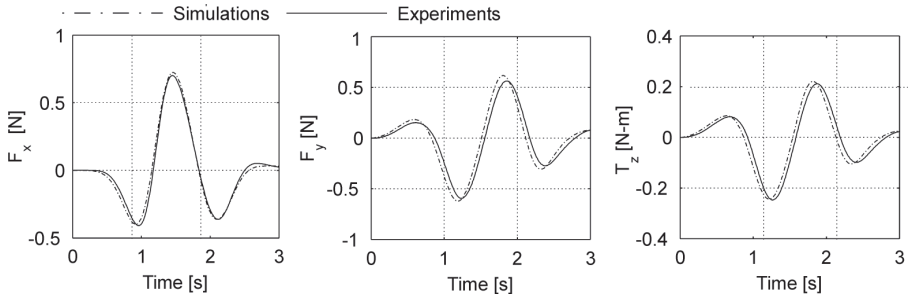

Figure 6.5: Reaction forces and torque with the LS resolution.

of the arm on of a grasped payload, 3) the influence of the reaction weighting factors, and, finally, 4) the possibility of increasing the reaction minimization performances by means of relaxing the trajectory-tracking precision.

For what concerns the influence of joint acceleration limits, we have carried out simulations by imposing stricter acceleration limits while performing the same trajectory-tracking manoeuvre discussed in previous section. It can be noticed that, imposing stringent acceleration limits, less freedom is available to the optimization task program, and the peak base reaction vary accordingly as reported in Fig. 6.13. In order to study the influence of a variation in arm and payload inertial properties to the base reaction minimization, we define the payload-arm mass ratio as

$$k_m = \frac{m_{\text{pay}}}{m_{\text{arm}}} \tag{6.16}$$

Here m_{arm} denotes the mass of the experimental robotic arm, and m_{pay} is the mass of an ideal point-mass payload attached to the manipulator tip. A change in the arm mass and inertia can be performed by defining a variated mass for the arm m'_{arm} with masses and inertias changed with the same factor. The mass ratio for the arm is defined as:

$$k_m = \frac{m'_{\text{arm}}}{m_{\text{arm}}} = \frac{I'_{\text{arm}}}{I_{\text{arm}}} \tag{6.17}$$

The results are presented in Fig. 6.14 for the peak values of the base reaction norm for the LS and LSE resolutions. The trajectory is always the circular path considered up to now. In all the considered cases, the LS reaction is higher than the LSE one, and the slope of the LS curve is higher than the LSE both in case of varying the payload and the arm mass. Moreover, the slope of the curve related to the variation of payload mass is higher than the slope related to the variation of the arm mass both for the LS and the LSE solutions.

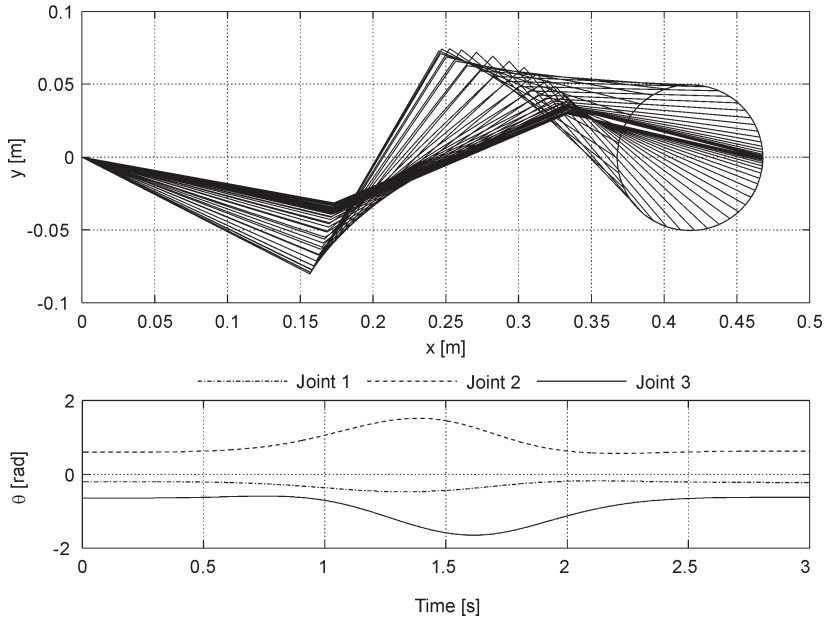

Figure 6.6: Stroboscopic plot and joint angle profiles for the LSE resolution.

In order to study the influence of the weight matrix $\boldsymbol{W}$ and the increase on the optimization requirements, define an equal weighting factor for the forces weights $w_F \triangleq w_{Fx} = w_{Fy}$ and consider the ratio with the torque weight $w_T \triangleq w_{Tz}$. The effects on the weighted reaction norm peaks and average values are reported in Fig. (6.15). It can be noticed that when $w_F/w_T = 0$, i.e when no force minimization is requested, a null reaction is obtained. Then, for increasing values of w_F/w_T the curve of the average values of $\|\boldsymbol{R}\|$ derived using the LSE solution is always below to the one derived using the LS solution. Nevertheless, concerning the peak values, the LSE values of $\|\boldsymbol{R}\|$ result higher than the LS ones for $w_F/w_T > 0.3$. This means that in this case the optimization is not effective in reducing the peak value of the weighted reaction norm even if the LSE average value is always below the LS one. For different end-effector trajectories or robot geometry the crossing point can be obtained for different weighting ratios, or may be not present at all.

Where stringent requirements on the allowed base reaction disturbance are required, the performance of the minimization can be further improved by means of relaxing the tracking precision of the end-effector trajectory, by means of acting on the weighting parameters λ_x and λ_R in the extended Jacobian solution by weightings of Eq. (5.26). The results are reported in

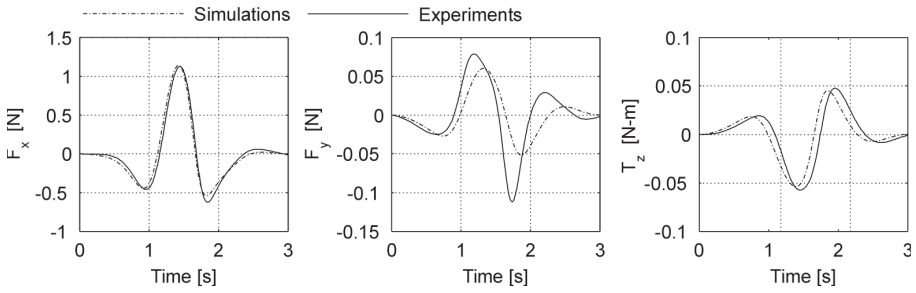

Figure 6.7: Reaction forces and torque with the LSE resolution.

Fig. (6.16) and (6.17) in terms of reaction disturbance and trajectory error, for a linear path trajectory tracking.

6.4 Reaction torque minimization

After the general base reaction control test campaign presented in the previous section, now the special condition for which the number of redundancies are equal to the dimension of the dynamic task is analyzed, i.e. the dimensional condition

$$n = k + d \tag{6.18}$$

The tracking vector is kept unchanged, while the definition of the controlled base reaction could be selected as each one of the reaction forces or torque component. The simulation campaign have demonstrated the interesting result that, for the 3-DOF manipulator under test, it is in general possible to achieve the exact tracking of a desired trajectory while exerting a null base reaction, and this have been tested for all the base reaction components F_x, F_y, and T_z.

Since the reaction torque is directly responsible for attitude disturbances, in this paragraph the results relative to the minimization of the base reaction torque are presented, showing the simulation results and their experimental validation by means of the planar manipulator prototype.

Trajectory tracking tests

The weighting matrix $\boldsymbol{W}$ is actually a scalar value since the only component $\boldsymbol{W} = [w_{Tz}] = 1$ is active. Thus the kinematic and dynamic variables

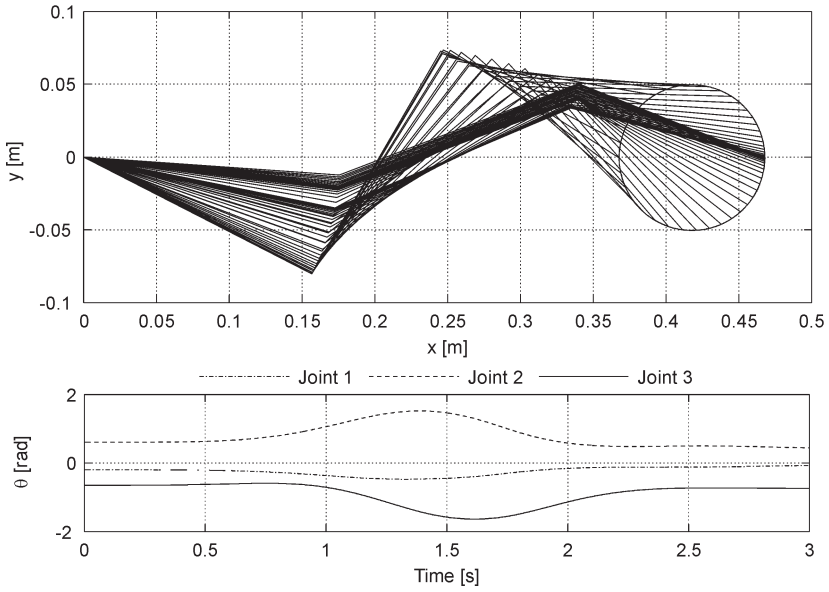

Figure 6.8: Stroboscopic plot and joint angle profiles for the LSEI resolution.

involved are:

$$\boldsymbol{x} = \begin{bmatrix} x \\ y \end{bmatrix} \qquad \boldsymbol{R} = T = [T_z] \tag{6.19}$$

The task dimensional conditions are:

$$k = 2 \qquad d = 1 \tag{6.20}$$

The resultant motion under LS, LSE, and LSEI control is reported in Fig. 6.18. The corresponding joint accelerations solutions are available in Fig. 6.19 for comparison, and lead to conclusions similar to the weighted reaction minimization for what concerns joint duty and acceleration limits. In order to provide a complete simulation and experimental test report, in the following are reported the reaction torques retrieved during the robot motion under RAC with the three algorithms. Reaction torque by LS resolution is reported in Fig. 6.20, reaction torque by LSE resolution in Fig. 6.21, and reaction torque by LSEI resolution in Fig. 6.21. The three reaction torques are compared in their magnitude in Fig. 6.23. Despite the good accord between the simulation and the experiment, the most significant point results in the fact that a *zero reaction torque manoeuvre* have been performed during a trajectory tracking of a generic circular path. The base reaction torque disturbance reduction of the rigid-body model simulation with respect to the LS resolution taken as reference, is of 100.0% for LSE control,

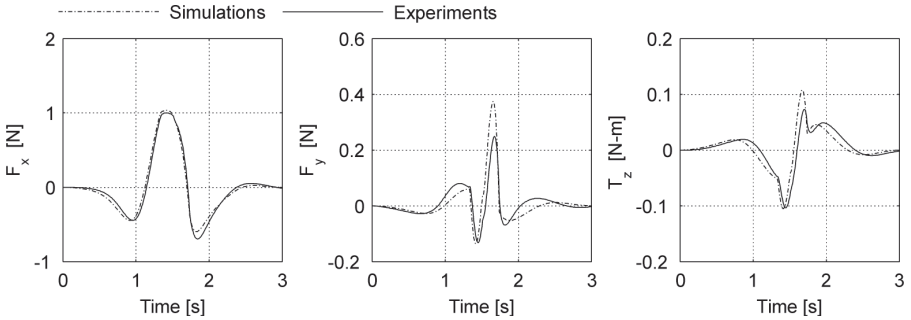

Figure 6.9: Reaction forces and torque with the LSEI resolution.

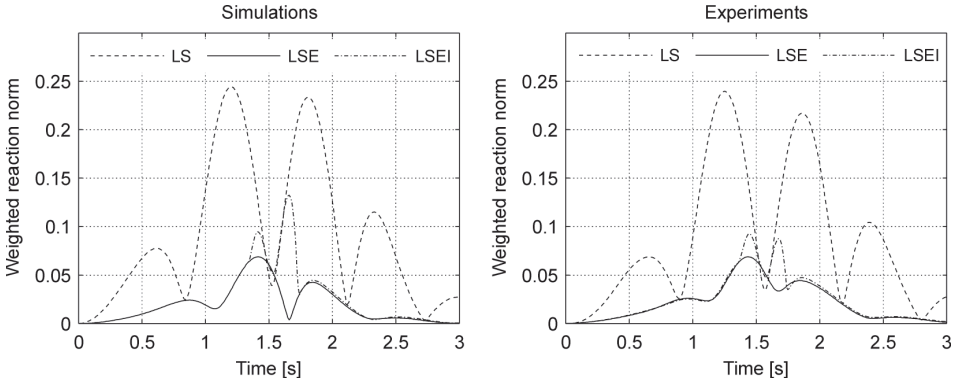

Figure 6.10: Weighted reaction norm comparison.

and reduced to 60.9% in the LSEI case for the same motivations explained in the weighted reaction tests. The experimental validation shows a reduction of 90.9% for LSE control, and 63.4% for LSEI control. The figures also show the simulation tests in Adams, where the joint flexibilities of the experimental robot have been simulated, allowing in a great extent to model the difference between the simulation tests and the experimental validations. Further informations about these tests can be found in publications by the author's group [45].

Thanks to the possibility of obtaining an exactly null reaction during trajectory tracking manoeuvres, the LSE control could be substituted in this conditions by the extended Jacobian inverse solution of Eq. (5.21). Simulations have been carried out and confirmed this statement. The availability of this behavior, suggested to extend the base reaction tracking requirements to a more general base reaction profile, to be used for example in order

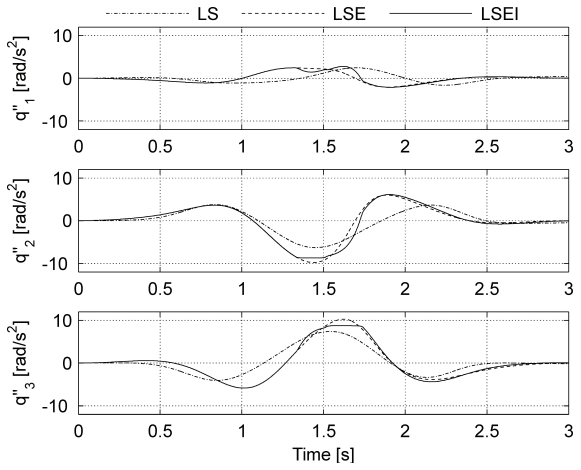

Figure 6.11: Resolved joint accelerations for the LS, LSE, and LSEI resolutions.

to dynamically coordinate several manipulators and/or spacecraft-reaction devices. This problem is introduced in Chapter 8.

Zero reaction workspace

In order to provide an insight on the possible movements that can be described in the manipulator workspace with a zero base reaction torque disturbance, a workspace simulation campaign have been carried out. The simulation tests have allowed the construction of a straight-path zero reaction torque workspace, that is referred to the initial configuration $\boldsymbol{\theta}_0$. When the kinematic control becomes unstable, the joint velocity and acceleration do diverge, and a workspace definition can be set by means of a limit bound for the desired measure. In this test it have been set an joint-velocity workspace limit of ± 0.2 rad/s. The construction of the straight-line workspace is carried out as follows. From the initial configuration a linear trajectory is described of a small length L_0; if the joint velocities during the motion have remained under the limits, the simulation is repeated for a greater length $L_0 + \Delta L$, until the previous condition is not anymore satisfied. At that point a workspace bound is defined and the process can be repeated for a different linear angle, until the whole plane have been spanned. The results are reported in Fig. 6.24, where are illustrated the zero reaction workspace that can be achieved without considering the physical joint position limits, and taking into account the joint limits. It's seen that the workspace is pretty large in the Cartesian space for the fixed base arm, although it

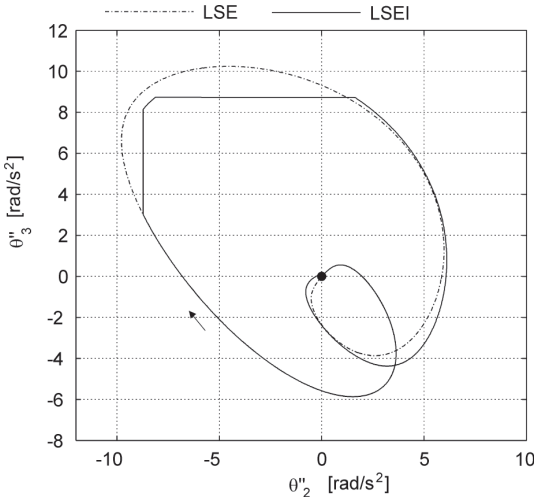

Figure 6.12: Joint acceleration trajectories of LSE and LSEI resolutions projected on joints 2 and 3.

represents a part of the complete motion workspace of the arm. The figure shows also the robot in its initial configuration, and the circular test trajectory, selected such that it was included in this workspace. Furthermore, it has to be noticed that this description is still partial, since although it gives important informations on the possible motions, there could be different nonlinear trajectories that may be performed outside this workspace without providing a base reactions, and others may arise that provide reaction disturbances inside the workspace, such as for singular configurations. Anyways, this construction provides an interesting starting point for further and more complete characterizations.

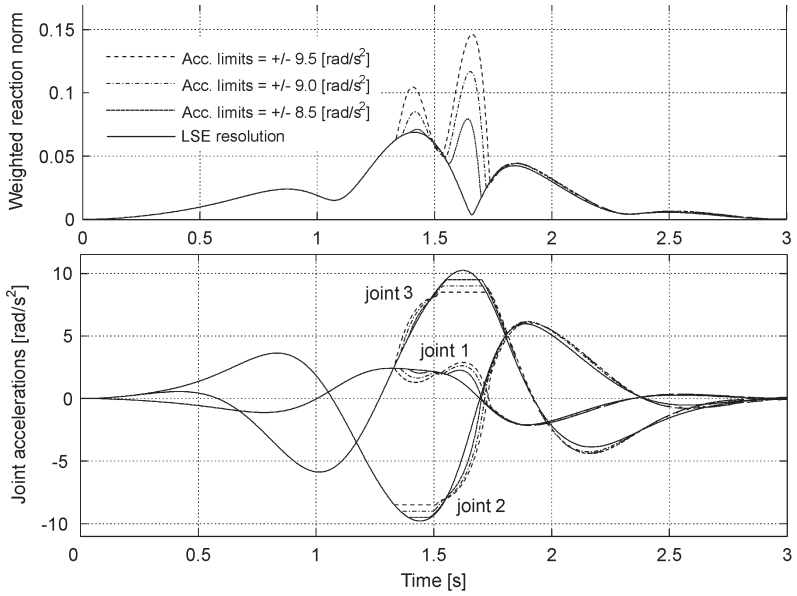

Figure 6.13: Increase of the peak reaction due to the introduction of joint acceleration limits.

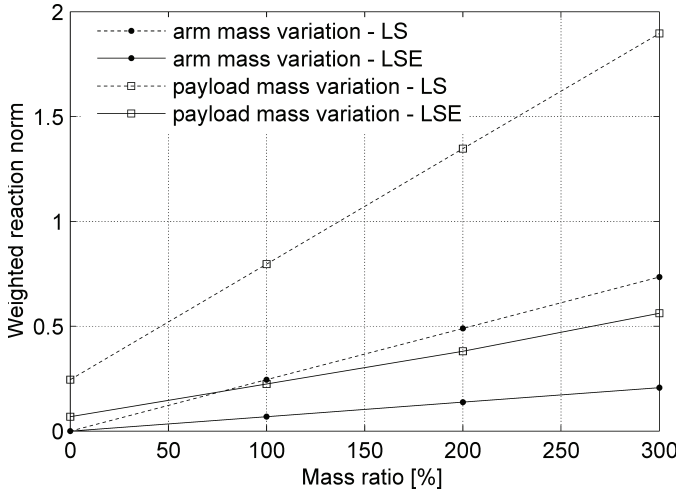

Figure 6.14: Effect of different payload and arm masses on the magnitude of the weighted reactions.

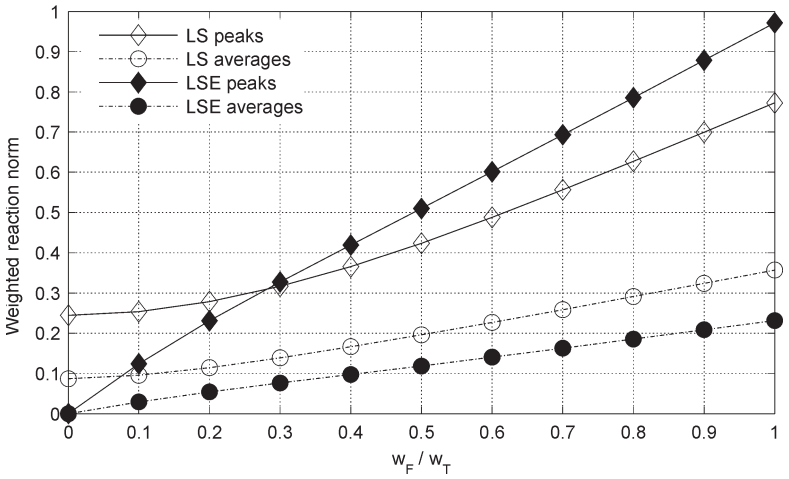

Figure 6.15: Peak and average values of the weighted reaction norm for increasing w_F/w_T ratios.

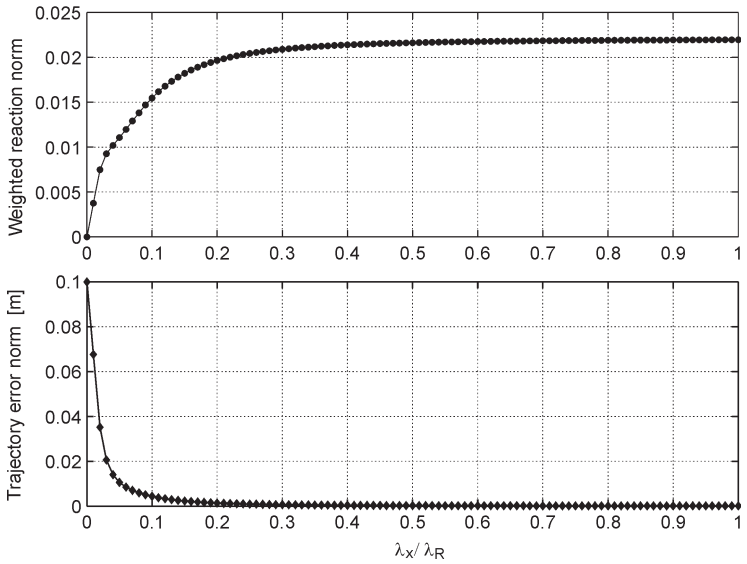

Figure 6.16: Kinematic and dynamic task priority switching for a linear path. A reduction in the trajectory tracking precision allows for reduced base reaction disturbance.

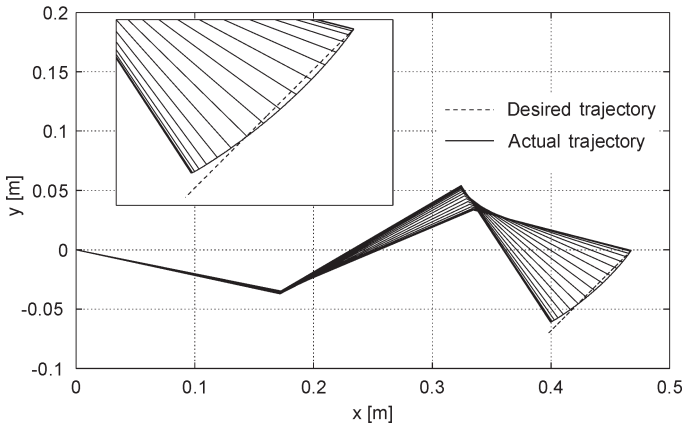

Figure 6.17: Trajectory tracking error with a kinematics/dynamics weight of $\lambda_k/\lambda_d = 0.05$.

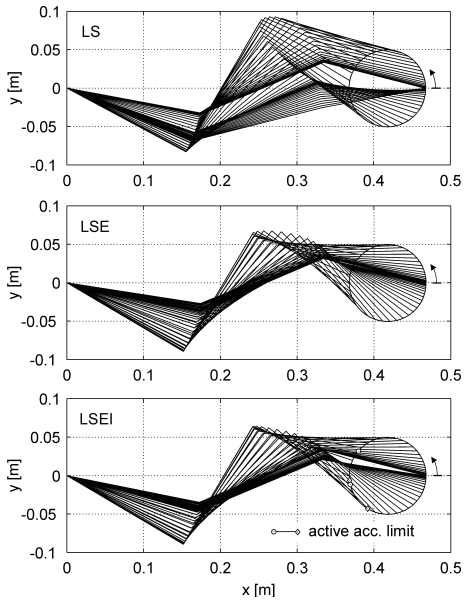

Figure 6.18: Stroboscopic motion plots, comparison of LS, LSE, and LSEI resolutions.

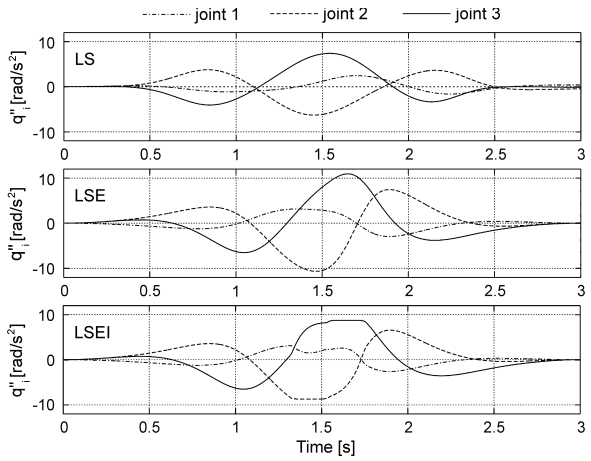

Figure 6.19: Joint control accelerations with LS, LSE, and LSEI solutions.

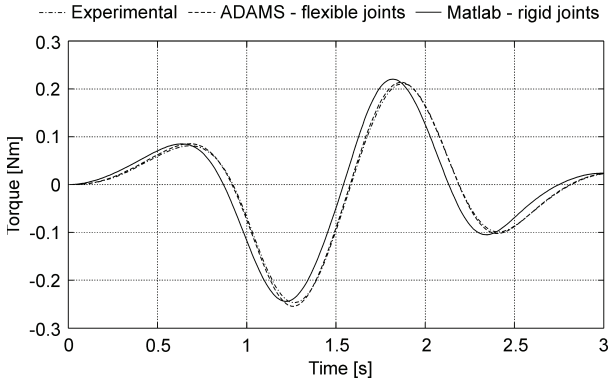

Figure 6.20: Reaction torque with the LS solution. Simulations and experimental results.

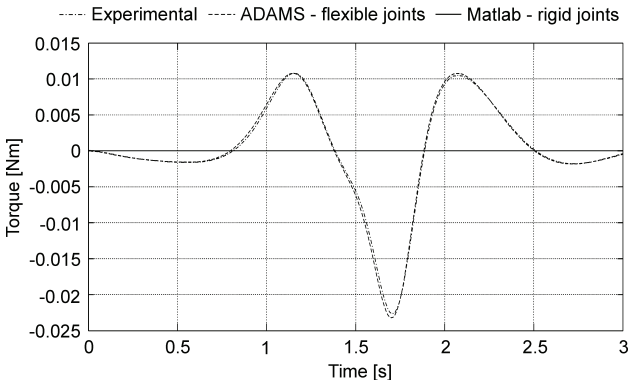

Figure 6.21: Reaction torque with the LSE solution. Simulations and experimental results.

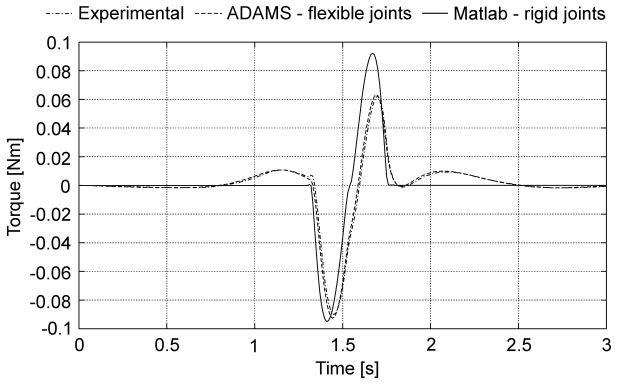

Figure 6.22: Reaction torque with the LSEI solution. Simulations and experimental results.

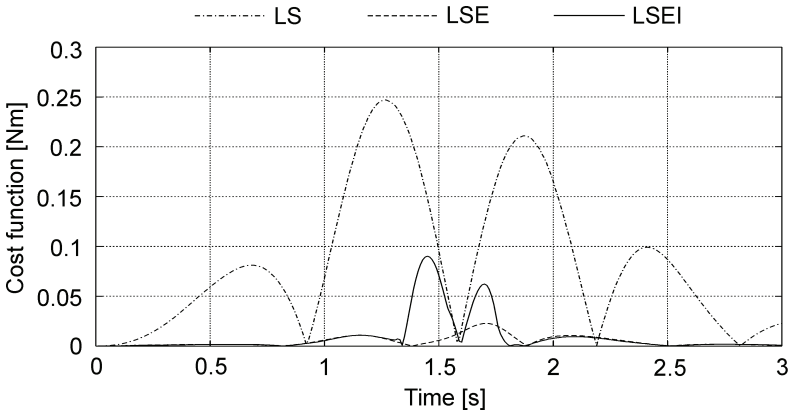

Figure 6.23: Reaction torque norm comparison, experimental results.

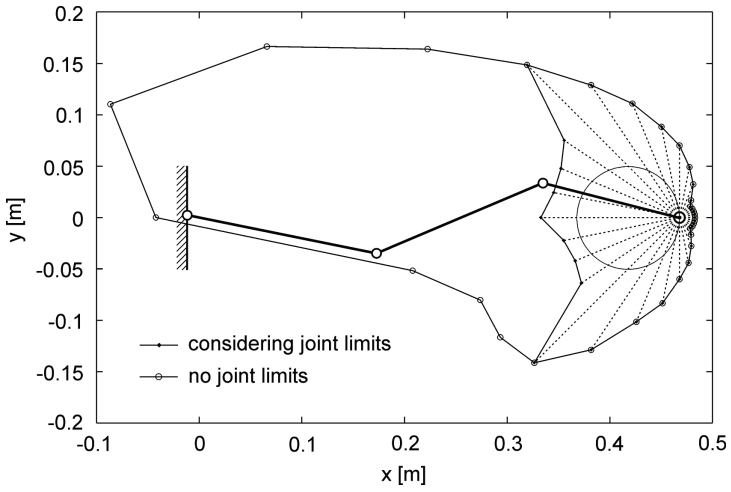

Figure 6.24: Straight-path zero reaction torque workspace, and the circular test trajectory.

Chapter 7

Reaction control of a free-floating base manipulator

In this Chapter the the performances of the base reaction control scheme illustrated in the previous Chapter for fixed base manipulators, is tested for free-floating base manipulator. The formal expression of the solutions is the same as in Chapter 6, with the difference that the base attitude variable need to be integrated by means of the base attitude Jacobian of Eq. (4.24) or retrieved by instrumentation measurements in order to evaluate the dynamic and kinematic quantities, as explained in Chapter 4. For completeness, the tracking trajectory is now defined in the inertial space:

$$\boldsymbol{x} = {}^{N}\boldsymbol{x} \tag{7.1}$$

and the GJM matrix is used in the kinematic expressions. Furthermore, the relations are still valid for a base referenced trajectory by making use of the FJM matrix in the kinematic expressions. The base reaction cost function is still the magnitude of the weighted base reaction:

$$g_R(\ddot{\boldsymbol{\theta}}) = \| \boldsymbol{R} \|^2 \tag{7.2}$$

At the acceleration level RAC control, the control variable is the joint acceleration vector $\ddot{\boldsymbol{\theta}}$, while the state variables is composed of base spacecraft orientation, and arm joint positions and velocities $(\boldsymbol{\phi}_B, \boldsymbol{\theta}, \dot{\boldsymbol{\theta}})$. Simulation tests are carried out for the planar 3-DOF manipulator, mounted on a free-floating base, and the minimization of the reaction torque is investigated in order to assess if the performances obtained for the fixes base condition are still obtained. Comparisons with the fixed base manipulator model

will be carried out and parametric analysis about the most significant variables are undertaken. Finally an extension of the straight-path zero reaction workspace is presented. The results of this Chapter have been published by the author's research group in [42].

7.1 Reaction torque minimization

A simulation test campaign is carried out for the reaction torque minimization control, in order to understand how the introduction of a free-floating base affects the system dynamics and the disturbance minimization performances. In this Chapter a slow tracking trajectory have been considered for tracking, which also represents a test-case for typical space operation manoeuvres, by imposing a tracking time period of $T = 100$ s. The tracking path $\boldsymbol{x}$ in this campaign is a *lemniscate* of length $L = \pi \cdot D$, of parametric equations $x^s = c_{Lx} + \frac{D}{2} \cdot \cos(\frac{2s}{D})$ and $y^s = c_{Ly} + \frac{D}{2} \cdot \sin(\frac{4s}{D})$. The diameter is D = 0.100 m, and center is located in $\boldsymbol{c}_L = \boldsymbol{x}_0 - [\frac{D}{2}, 0]^{\mathrm{T}}$. Here $\boldsymbol{x}_0 = \boldsymbol{k}_N(\boldsymbol{\phi}_{B0}, \boldsymbol{\theta}_0)$ is the initial position of the robot end-effector, and $\boldsymbol{k}_N$ represent the forward kinematics function presented in Chapter 4. The initial base orientation is assumed as the zero attitude angle $\boldsymbol{\phi}_{B0} = \mathbf{0}$. The tracking movement of the arm has to be carried out by means of the same smooth motion law used for the fixed base robot tests of Fig. 6.3, and scaled to the appropriate tracking period. desired trajectory is then obtained by composition as in the circular test campaign $\boldsymbol{x}_{\mathrm{d}}(t) = \boldsymbol{x}^s \circ s(t)$.

The inertial parameters of the free-floating base for the tests are those of the original experimental robot tested during ESA parabolic flight campaign by the author's research group [52, 55]:

$$m_B = 4.16 \text{ kg} \qquad I_B = (I_{Gz})_B = 3.36 \cdot 10^{-2} \text{ kg m}^2 \tag{7.3}$$

Tests are carried out for LS and LSE control, and the results are compared to the same problem resolved for the fixed base manipulator. Motion plots for the LS resolution are displayed in Fig. 7.1 and the relative joint accelerations in Fig. 7.2. It can be noticed the non-negligible attitude disturbance on the base, that results by means of an LS inversion, although the trajectory is tracked with precision. On the other side, the joint acceleration command profiles results significantly increased in the free-floating condition for these inertial configuration, with an increment of 100 %. Results of the LSE resolution compared to the fixed base configuration are displayed in Fig. 7.3 for what concerns the base and arm motion, while in Fig. 7.4 are displayed the joint acceleration solution profiles.

Notice that the base attitude is not affected and remains stable during the whole motion, while the end-effector trajectory is performed with precision. This is due to the fact that in this special task-dimensional condition

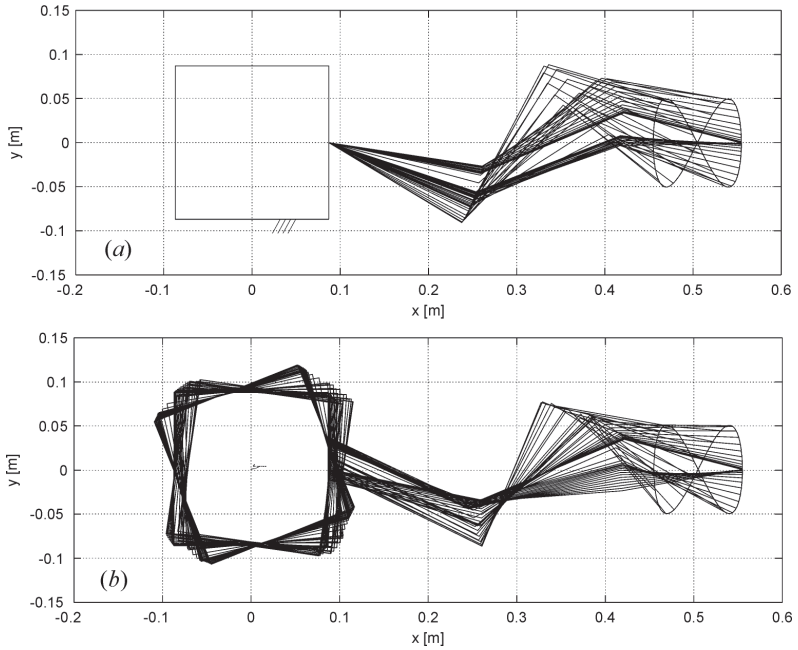

Figure 7.1: Stroboscopic plots, comparison between (a) the fixed base manipulator, and (b) the free-floating base manipulator with the LS solution.

of $n = k + d$, both the tracking task and the base dynamic task may be exactly performed, and the point that a general trajectory-tracking manoeuvre can actually be performed with zero reaction torque and zero attitude disturbance for the free-floating robot represents an important result. Due to this observation, the LSE tracking solution is also achieved by means of an extended Jacobian inverse approach. Observe how the stability conferred to the base location by means of the LSE control, results also in joint acceleration solutions very close to the fixed base LSE solutions, with a peak increment of only 15.7 %. This observation may lead to the investigation of a possible resolution of the optimal dynamic problem by means of a simplified fixed-base dynamics model, with great save in computational efforts. Further informations about this point can be found in the publication by the author's research group [42]. In order to acquire a better understanding on the influence of the base-arm inertial parameters on the required joint acceleration solutions a parametric study is proposed in the following paragraph. In Fig. 7.5 the resulting base reaction torque is reported, and it can be observed the significant increase of 140 % in the base disturbance for the LS solution in the free-floating condition, while a zero reaction torque

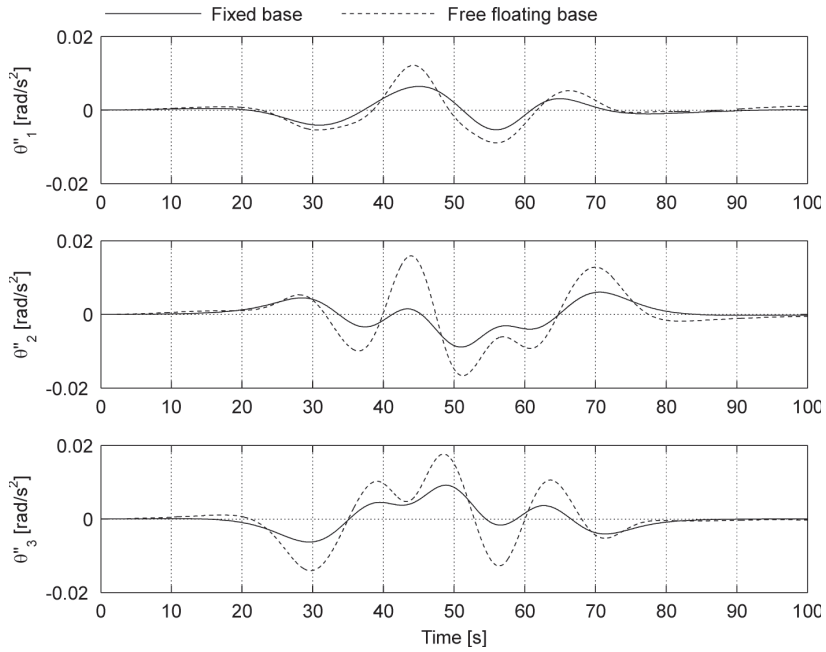

Figure 7.2: LS resolved joint accelerations for the fixed base and the free-floating base conditions.

is achieved for the LSE solution in both the conditions. This represents an important observation in order to justify the implementation of base reaction control schemes for space application, such as the proposed constrained least squares paradigms.

7.2 Mass ratio considerations

In this paragraph, a study on the influence of the inertial properties of the base spacecraft on the required joint position displacements, velocities, and accelerations is presented, performing the trajectory tracking manoeuvre discussed in the previous section by means of mounting the manipulator on free-floating platforms with different masses and inertias. At this purpose, define a base/arm mass ratio k such that:

$$m_B = k \cdot m_{\text{arm}} \tag{7.4}$$

The spacecraft inertia is varied accordingly, by assuming a constant mass density, according to the proportion:

$$I_B / m_B^{\frac{5}{3}} = \text{const.} \tag{7.5}$$

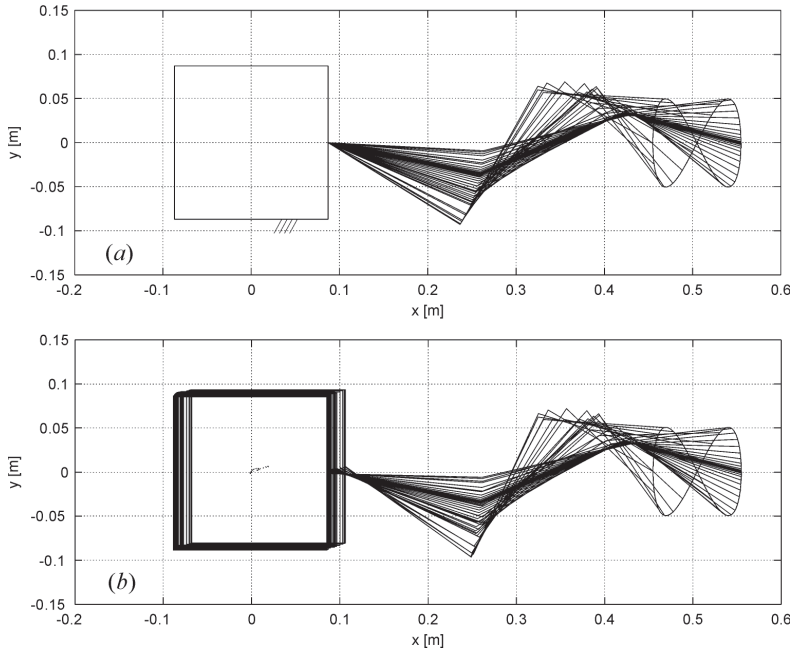

Figure 7.3: Stroboscopic plots, comparison between (a) the fixed base manipulator, and (b) the free-floating base manipulator with the inverse or LSE solution.

The peak joint variables solutions obtained by an LS control, are displayed in Fig. 7.6. Observe that when the spacecraft inertia tends to very high values, the robot approaches the fixed base condition, assuming that the base platform has a null momentum in the inertial space at the beginning of the manoeuvre. Results for the LSE control, are displayed in Fig. 7.7. From the analysis of the LS results, it can be noticed that the peak values of the joint angle, velocity and acceleration increase as long as the inertial properties are decreased, and that the percent variation is higher for joint accelerations and velocities, with respect to joint angles. The same considerations can be made in case of using the LSE solution. Observe also that the joint variables increase is much higher in the LS case, especially for what concerns joint accelerations and velocities. In both figures the case k = 100, which is related to a massive spacecraft, is taken as a reference in order to compute the percent variations. This observations represent a generalization of what was observed in the previous section about the LSE solution, which, thanks to the stability inferred to the base attitude, causes the optimal joint solutions to differ less that the LS solution to the fixed base condition. This motivates further investigations about a possible implementation of approximated fixed

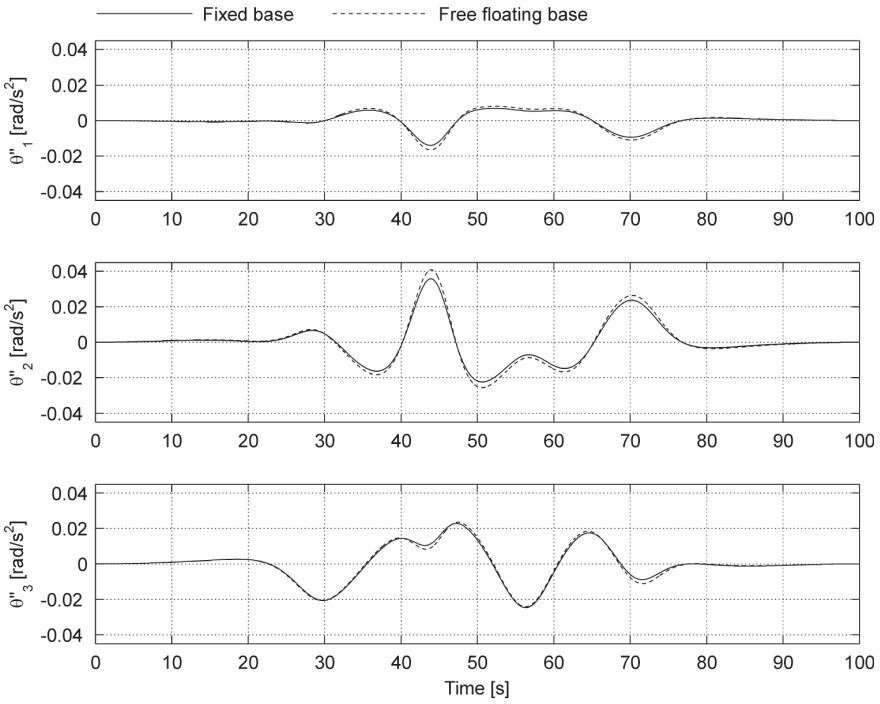

Figure 7.4: LSE resolved joint accelerations for the fixed base and the free-floating base conditions.

base dynamics model in order to achieve good results with great save of computational effort for large spacecrafts and applications for space stations.

7.3 Zero reaction workspace

In this section a study on the straight-path workspace in which a zero reaction torque can be obtained is carried out for different base inertial properties. First of all, the Zero Reaction Workspace of the free-floating robot considered in the previous section, for which $k = 1.95$, is compared to the one of a fixed based robot, for which $k \to \infty$. The comparison, presented in Figure 7.8, is carried out both considering the robot real joint position limits:

$$\bar{\boldsymbol{\vartheta}} = \tfrac{\pi}{180} \cdot [\pm 90, \pm 120, \pm 120]^{\mathrm{T}} \text{ rad} \tag{7.6}$$

and without that constraint. Then, the Zero Reaction Workspace of the robot taken as a reference with $k = 1.95$ is compared to the ones related to a lightweight spacecraft with $k = 0.1$, illustrated again in Fig. 7.8. The Zero

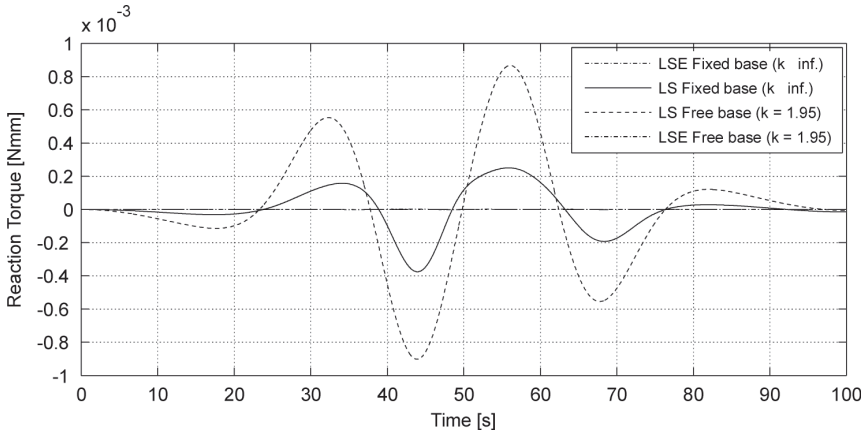

Figure 7.5: Base reaction torque disturbance with LS and LSE resolutions, and comparison to the fixed base robot results.

Reaction Workspaces are computed using straight end-effector paths, in a similar approach to that discussed for the fixes base robot in Chapter 6. In this case a constant velocity profile gave been adopted, and the workspace bound obtained when a joint velocity value exceeded the limit value of ± 2 rad/s. From the analysis of Figure 10, it can be noticed that: 1) the Zero Reaction Workspace computed considering joint limits is contained in the one which does not consider them, for both robot configurations; 2) the Zero Reaction Workspace of the free floating robot computed without considering joint limits is contained in the one of the fixed-based robot; 3) the same as point 2. is true also considering joint limits.

Point 1. is easily understood, since each straight end-effector path can be terminated before the LSE solution becomes unstable, when one joint limit is reached. Point 2. is due to the fact that, for a given end-effector trajectory, if a free-floating robot is used instead of a fixed based one, higher joint velocities and accelerations are needed and, therefore, the joint velocity limit is reached beforehand. Similarly, point 3. is due to the fact that, for a given end-effector trajectory, a free-floating robot needs higher joint angles with respect to a fixed based one.

Some unexpected behaviour is noticed when small base inertial properties are used. For some directions, in fact, the Zero Reaction Workspace for $k = 0.1$ is external to that related to the reference case $k = 1.95$. This is due to a favorable displacement of the base, which during the motion reaches a position that allows the reach of more distant points. This concept can be better understood by means of the example shown in the stroboscopic plot

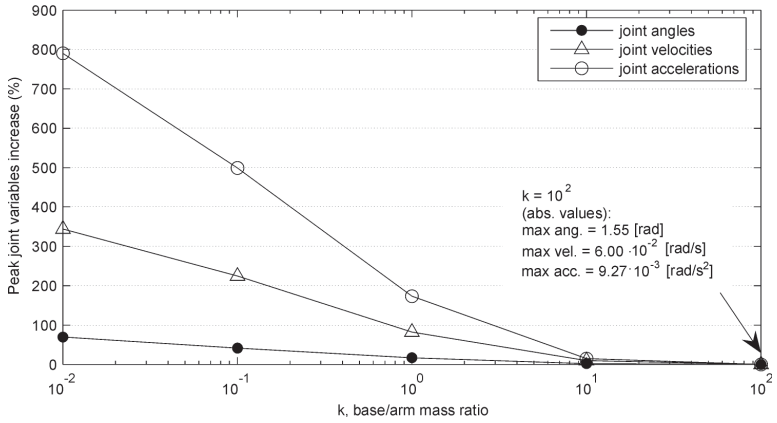

Figure 7.6: Increase the peak joint variables with a reduction in the spacecraft base mass and inertia, with the LS solution.

of Fig. 7.9 in which a long zero reaction straight path is presented in the case of $k = 0.1$.

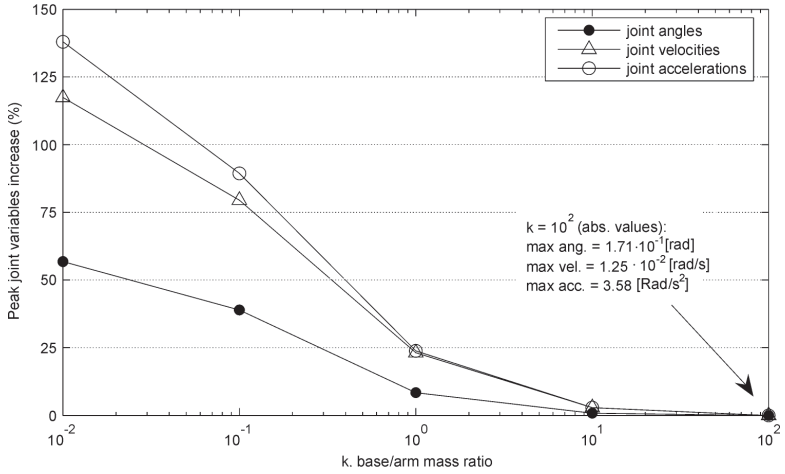

Figure 7.7: Increase the peak joint variables with a reduction in the spacecraft base mass and inertia, with the LSE solution.

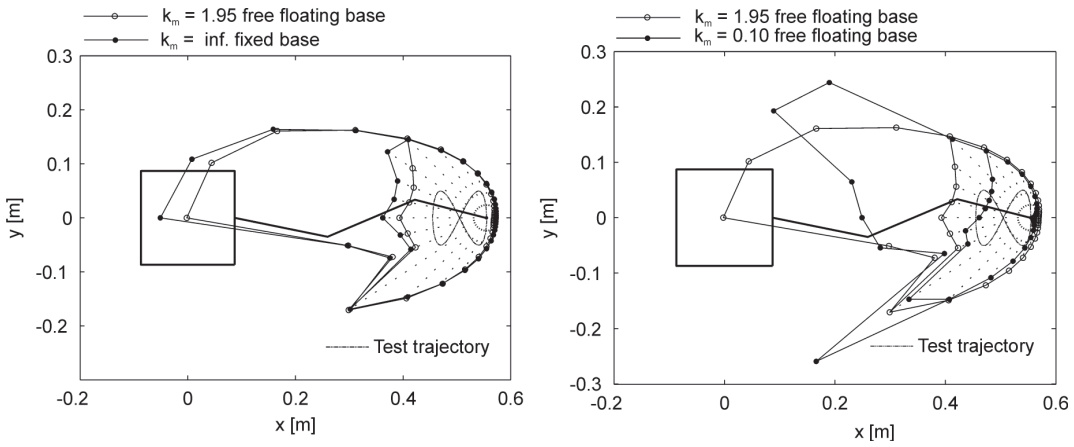

Figure 7.8: Straight-path workspace for a free-floating base arm compared to the fixed base workspace and to a different base inertia.

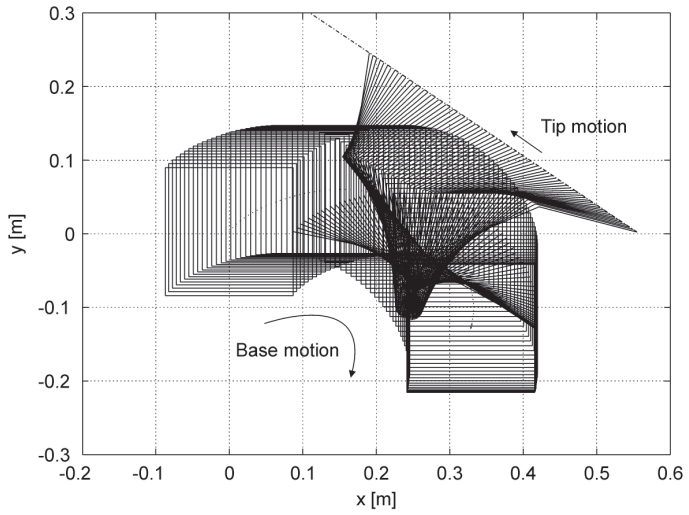

Figure 7.9: Favourable base displacement during a straight path end-effector tracking.

Chapter 8

Extensions and applications

In this Chapter, the base reaction control laws exposed in the previous chapters will be extended to the tracking of a general base reaction profile, making full use of the control framework presented in Chapter 5. A complete description of this concept was published by the author's research group in [43].

8.1 Desired acceleration feedback

In previous chapters, a trajectory tracking maneuver was considered, and the kinematic control problem resolved for a precise trajectory tracking and assuming a fine accordance between the manipulator model and the real robot. In order to cope with model uncertainties and more complex tasks and systems, it reveals useful to introduce a feedback control formulation in the control scheme. In order to realize this objective, the notion of the desired end-effector acceleration profile, denoted now as $\boldsymbol{a}_{\mathrm{d}} = \boldsymbol{a}_{\mathrm{d}}(t)$ can be extended.

In the previous discussion, the desired acceleration profile was simply defined as the second time-derivative of the desired end-effector trajectory

$$\boldsymbol{a}_{\mathrm{d}} = \ddot{\boldsymbol{x}}_{\mathrm{d}} \tag{8.1}$$

A more general acceleration profile can be prescribed instead, including feedback gains with respect to the position and velocity errors in the RAC context, for example with PD the law as proposed by Yoshida and Umetani in [11] for space manipulators:

$$\boldsymbol{a}_{\mathrm{d}} = \ddot{\boldsymbol{x}}_{\mathrm{d}} - \boldsymbol{K}_D(\dot{\boldsymbol{x}} - \dot{\boldsymbol{x}}_{\mathrm{d}}) - \boldsymbol{K}_P(\boldsymbol{x} - \boldsymbol{x}_{\mathrm{d}}) \tag{8.2}$$

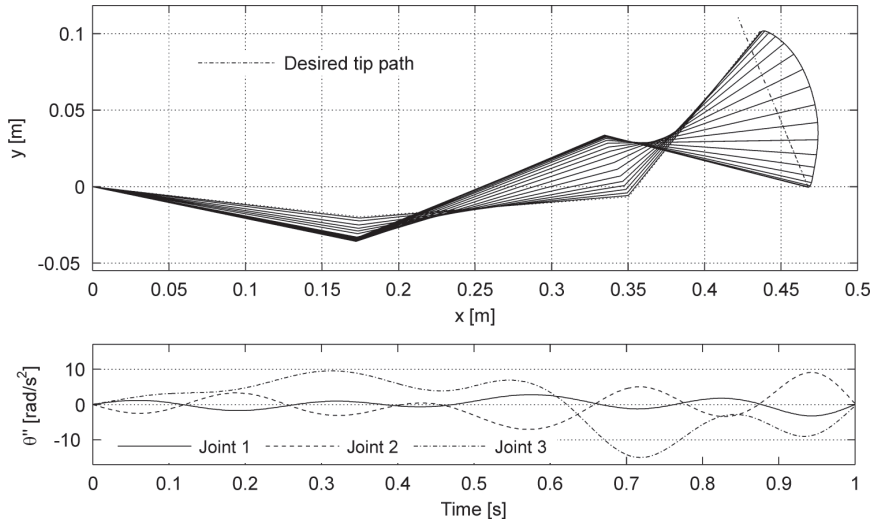

Figure 8.1: Approximation of an end-effector trajectory while performing a force tracking for the reaction components F_x and F_y by simulation.

The proportional gain $\boldsymbol{K}_P$ can be interpreted as a multi-dimensional spring attractor that keeps the end-effector location close to the moving target along the trajectory, while the derivative gain $\boldsymbol{K}_D$ can be interpreted as a multi-dimensional virtual damper. A more simple formulation for the feedback acceleration

$$\boldsymbol{a}_{\mathrm{d}} = -\boldsymbol{K}_P(\boldsymbol{x} - \boldsymbol{x}_{\mathrm{d}}) - \boldsymbol{K}_D(\dot{\boldsymbol{x}} - \dot{\boldsymbol{x}}_{\mathrm{d}}) \tag{8.3}$$

Other laws can be investigated and with their stability properties, according to the specific problem and task priorities considered. For the generality of the formulation consider also a traditional PD feedback scheme at the acceleration level that may be useful for Point to Point Manoeuvres:

$$\boldsymbol{a}_{\mathrm{d}} = -\boldsymbol{K}_P\,(\boldsymbol{x} - \boldsymbol{x}_{\mathrm{d}}) - \boldsymbol{K}_D\,\dot{\boldsymbol{\theta}} \tag{8.4}$$

This last equation may be interpreted as a basic Path Planning scheme. In this way, the RAC statements of imposing the desired acceleration tracking is expressed as

$$\ddot{\boldsymbol{x}}(\ddot{\boldsymbol{\theta}}) = \boldsymbol{a}_{\mathrm{d}}(t) \tag{8.5}$$

and the least squares approximation of the desired acceleration profile is expressed in the form:

$$\ddot{\boldsymbol{x}}(\ddot{\boldsymbol{\theta}}) \cong \boldsymbol{a}_{\mathrm{d}}(t) \tag{8.6}$$

Some of these control laws will be used and investigated in the extended problems of the foregoing sections.

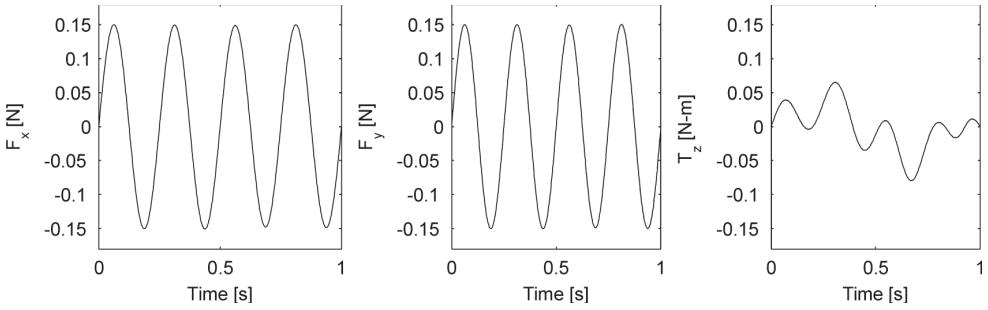

Figure 8.2: Reaction forces and torque simulation. The forces F_x and F_y are under tracking while the torque T_z is free.

8.2 Base reactions tracking

The idea of tracking a desired base reaction profile extends the kinematic trajectory tracking to the dynamic task, exchanging the roles of the kinematic Jacobian matrix and the dynamic mass matrix.

Inverse dynamic-tracking problem For a dimensional condition given by:

$$n = d \tag{8.7}$$

The problem of inverting the dynamics at the acceleration level of the manipulator can be tackled, in order to perform the desired reaction profile

$$\boldsymbol{R}(\ddot{\boldsymbol{\theta}}) = \boldsymbol{R}_{\mathrm{d}}(t) \tag{8.8}$$

and the solution if exists can be given in the form:

$$\ddot{\boldsymbol{\theta}} = \boldsymbol{M}^{-1}(\, \ddot{\boldsymbol{x}}_{\mathrm{d}} - \boldsymbol{n}\,) \tag{8.9}$$

Least squares dynamic-tracking problems The extension to the non-square mass matrix condition, can be provided at first by the pseudoinverse solution at the dynamic task level:

$$\ddot{\boldsymbol{\theta}} = \boldsymbol{M}^{\dagger}(\, \boldsymbol{R}_{\mathrm{d}} - \boldsymbol{n}\,) \tag{8.10}$$

In the *dynamic deficiency* condition for which

$$n < d \tag{8.11}$$

the LS formulation provides the solution to the problem $\boldsymbol{R}(\ddot{\boldsymbol{\theta}}) \cong \boldsymbol{R}_{\mathrm{d}}(t)$, minimizing the acceleration error $g_a = e_a^2$, that can be made explicit in the joint variables as:

$$\boldsymbol{M}\,\ddot{\boldsymbol{\theta}} + \boldsymbol{n} \cong \boldsymbol{R}_{\mathrm{d}}(t) \tag{8.12}$$

On the other side, for the *dynamic-task redundancy* condition

$$n > d \tag{8.13}$$

the LS solution represents the reaction tracking $\boldsymbol{R}(\ddot{\boldsymbol{\theta}}) = \boldsymbol{R}_{\mathrm{d}}(t)$ solution of minimum joint acceleration norm $\ddot{\boldsymbol{\theta}} \cong \mathbf{0}$, solution to the explicit problem

$$\left\{ \begin{array}{rcl} \boldsymbol{M}\,\ddot{\boldsymbol{\theta}} + \boldsymbol{n} & = & \boldsymbol{R}_{\mathrm{d}}(t) \\ \ddot{\boldsymbol{\theta}} & \cong & \mathbf{0} \end{array} \right. \tag{8.14}$$

8.3 Dynamic coordination principles

In order to extend the formulation to the simultaneous kinematic and dynamic task control, the optimization framwork of Chapter 5 can be used and extended.

Exact end-effector trajectory with approximate reaction profile The problem of tracking a desired end-effector trajectory with approximate reaction profile is equivalent to the complete LSE problem in chapter 5. Simulation tests can be found in [43] for this concept.

Exact reaction profile with approximate end-effector trajectory More interesting is the case in which the priorities of the tasks are switched, such as we intend to perform the exact tracking of a defined base reaction profile, with the best approximation of a desired end-effector trajectory. The necessary redundancy condition be:

$$n > d \tag{8.15}$$

This Least Squares problem with Equality constraints (LSE), can be formulated as:

$$\left\{ \begin{array}{rcl} \boldsymbol{J}\,\ddot{\boldsymbol{\theta}} + \dot{\boldsymbol{J}}\,\dot{\boldsymbol{\theta}} & \cong & \boldsymbol{a}_{\mathrm{d}}(t) \\ \boldsymbol{M}\,\ddot{\boldsymbol{\theta}} + \boldsymbol{n} & = & \boldsymbol{R}_{\mathrm{d}}(t) \end{array} \right. \tag{8.16}$$

in which the approximation-optimization line and constraint line have been switched with respect to the previous formulation. The cosed form pseudoinverse formulation of the solution is provided by:

$$\ddot{\boldsymbol{\theta}} = \boldsymbol{M}^{\dagger}(\boldsymbol{R}_{\mathrm{d}} - \boldsymbol{n}) - (\boldsymbol{J}\boldsymbol{Z}_M)^{\dagger}\,[\boldsymbol{J}\boldsymbol{M}^{\dagger}(\,\boldsymbol{R}_{\mathrm{d}} - \boldsymbol{n}) - (\,\boldsymbol{a}_{\mathrm{d}} - \dot{\boldsymbol{J}}\,\dot{\boldsymbol{\theta}}\,)] \tag{8.17}$$

and of course the extended Jacobian formulation by weighting can be used, with $\lambda_R \gg \lambda_x$. In Fig. 8.1 is illustrated the manipulator motion for the tracking of a sinusoidal force profile in which the desired force vector is selected as:

$$\boldsymbol{R} = \begin{bmatrix} F_x \\ F_y \end{bmatrix} \tag{8.18}$$

while the reaction torque is left free. In the meantime a linear path is approximated with the usual smooth motion law, with the feedback acceleration law of Eq. (8.3), and the gains $\boldsymbol{K}_P = \boldsymbol{K}_D = 100 \cdot \mathbf{1}$. Fig. 8.2 shows the resulting base reaction profiles obtained by simulation.

Chapter 9

Climbing forces control of a bio-inspired robot

In this Chapter a work on modeling and control of contact forces for a climbing robot with dry adhesion pads is presented. The work represent a significant part of the research activity carried out in cooperation with the robotics laboratory at the Simon Fraser University in Canada in 2008, under the supervision of Prof. Menon, for the project of development of a bio-inspired climbing robot for space applications [56].

The mechanical model of the climbing robot consists of a main body or payload to which several legs are mounted in order to form a structure with grasping capacities. Consider an inertial reference frame fixed to c climbing surface $\vec{\Sigma}_c$ and express all the quantities in this frame. The external forces applied to the robot are its local-gravity weight $\boldsymbol{F}_b = m\,\boldsymbol{g}_{\otimes}$ and the contact forces and torques at each contact pad $\boldsymbol{F}_{ci}$ and $\boldsymbol{T}_{ci}$, that from a closer insight at each contact pad, are the resultant action of a distributed surface stress field $\boldsymbol{t} = \boldsymbol{t}(\boldsymbol{r})$ applied at the points of contact $\boldsymbol{r}$ between the adhesion pads and the climbing surface.

The robot is conceived in order to take advantage of dry adhesive attachment pads, that consist of Polydimethylsiloxane (PDMS) micromachined layers. In order to take full advantage of the adhesion properties of the robot, and be able to perform a stable climbing of steep, vertical, and maybe negative sloped surfaces, the control problem have been conceived by decomposition in two independent parts:

1. a model of adhesion that relates the resultant actions on the pads to the local surface tensions, that, together with a criticality measure of the local stress tensions, give a prediction of the detachment conditions

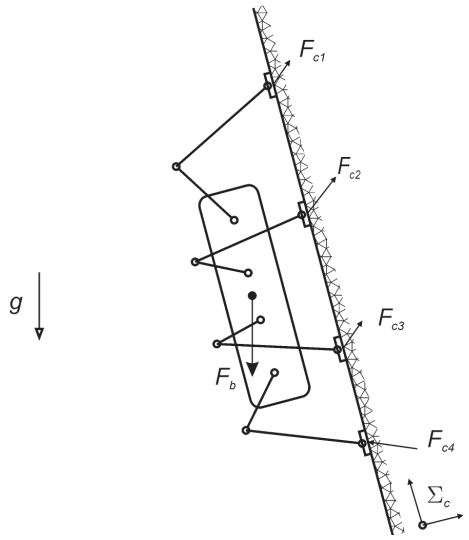

Figure 9.1: Climbing robot weight and contact forces.

of the pads, and allow to formulate a measure of distance from the overall robot detachment conditions, to be minimized through active joint control;

2. a joint torque active control logic, that together with a structural model of the robot relating the joint torques to the surface contact forces, allows to take the best advantage of the system capacity in terms of grasping and adhesion.

The two steps are summarized in Fig. 9.2, and discussed in the following sec-

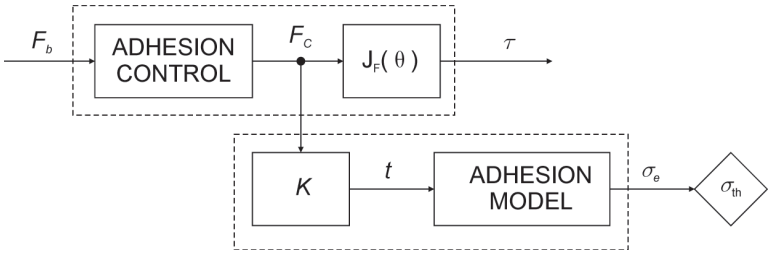

Figure 9.2: Adhesion control schematics.

tions, for the aforementioned adhesive material, and an experimental robot prototype that have been developed at the Simon Fraser University in order to validate the control concepts.

9.1 A model of adhesion

A simple model of adhesion have been proposed for the micro-machined PDMS material in order to be suitable for real-time applications, for control and simulations purposes. The model have been implemented on a dynamic simulator for a climbing robot; for details see the masters thesis of Ruffieux in [57]. The results in this chapter have been presented by the author's research group in [38], while different approaches in literature can be found in particular in Autumn et al. [58].

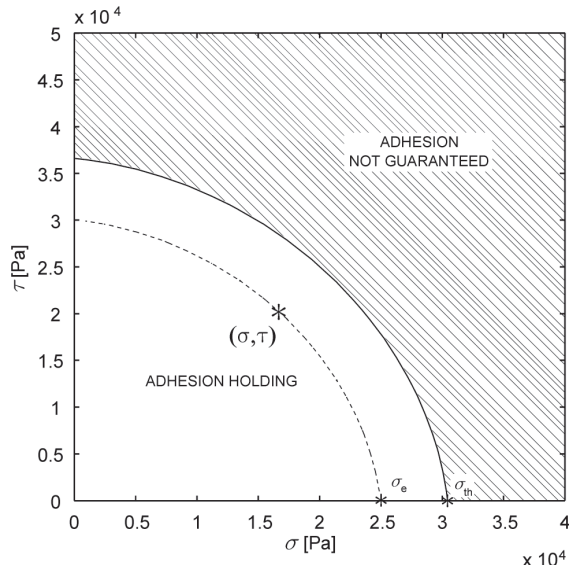

Figure 9.3: Adhesion model in the Yield space of the surface stresses.

Contact forces The model is developed for the surface interaction between PDMS and glass. The adhesion surfaces are applied to the tip of rigid cantilever of rectangular cross section that is subject to different external forces $\boldsymbol{F}$ until the detachment is attained. This setup can be interpreted as a basic model for a single robotic pad, although a specific test campaign may be carried out once a prototype design configuration have been defined. The assumption of the transmission of a negligible torque action by the robot is justified some kind of passive spherical joint is designed in order to adapt the pad to the climbing surface, but the concept can be extended to the more general solicitation condition.

By means of a rigid cantilever model, the resultant contact forces $\boldsymbol{F}_c$ and torque $\boldsymbol{T}_c$ at the contact interface can be retrieved by means of classic

relations from the beam theory. The resultant contact forces are

$$\boldsymbol{F}_c = \begin{bmatrix} F_x \\ F_y \\ F_z \end{bmatrix} \tag{9.1}$$

and resultant contact torques about the center of the contact surface are:

$$\boldsymbol{T}_c = \begin{bmatrix} T_x \\ T_y \\ T_z \end{bmatrix} = \begin{bmatrix} -F_y \cdot \ell \\ F_x \cdot \ell \\ 0 \end{bmatrix} \tag{9.2}$$

Considering the local surface tension vector $\boldsymbol{t} \triangleq [\,\tau_x, \tau_y, \sigma_z\,]^{\mathrm{T}}$, according to a simple elastic beam model, the local solution with $\boldsymbol{r} = [\,x, y, z\,]^{\mathrm{T}}$ is given by:

$$\boldsymbol{t}(\boldsymbol{r}) = \begin{cases} \tau_x &= \left(\frac{h^2/4 - y^2}{b^2/6}\right) \cdot \frac{F_x}{A} \\ \tau_y &= \left(\frac{b^2/4 - x^2}{h^2/6}\right) \cdot \frac{F_y}{A} \\ \sigma_z &= \frac{F_z}{A} + \frac{T_x \cdot y}{J_x} + \frac{T_y \cdot x}{J_y} \end{cases} \tag{9.3}$$

where $A = bh$ is the area of the contact surface, and $J_x = bh^3/12$ and $J_y = hb^3/12$ are the two static moment of inertia for a rectangular surface.

Adhesion model The detachment conditions are studied in the Yield plane of variable $\boldsymbol{\sigma} = [\sigma, \tau] = [\,\sigma_z, \sqrt{\tau_x^2 + \tau_y^2}\,]$. The underlying idea is to obtain a generalization of the classic criterium for the fracture predictions of linear elastic materials due to Von Mises, in which the equivalent stress measure can be evaluated as $\sigma_{e(\mathrm{VM})} = \sqrt{\sigma^2 + 3\tau^2}$. This value can be visualized int the Yield plane as the intercept of the an ellipse passing through the local Yield status, and parallel to the threshold ellipse, with the σ-axis.

For the purpose of determining an equivalent measure of the stress and a threshold condition for the material under investigation, we proceed as follows, (a) several tests of detachment are reproduced on a test beam, (b) an estimation of the surface stresses is given, and (c) an ellipse of best interpolation in the Yield plane of the estimated detachment conditions is determined. The general expression of an ellipse in the Yield plane is:

$$A\sigma^2 + B\sigma\tau + C\tau^2 + D\sigma + E\tau + F = 0 \tag{9.4}$$

which is completely determined by its coefficient array $\boldsymbol{A} = [\,A, B, C, D, E, F\,]$. Also, the set of the ellipses centered at the origin may be useful, that are those with $D = E = 0$. The values of the coefficients in $\boldsymbol{A}$ can be determined by least squares fitting of the detachment data, and all the parallel ellipses can be parameterized by the parameter F in Eq. (9.4).

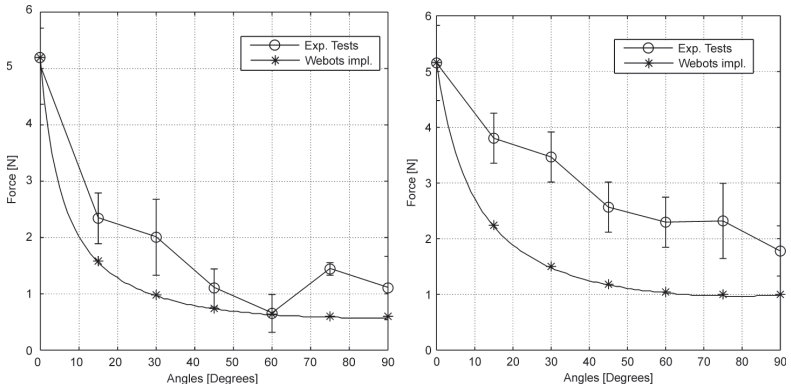

Figure 9.4: Adhesion detachment tests and model implementation conservative predictions.

Call F_e the parameter chosen to represent the threshold ellipse, than at the σ-axis intercept the equivalent stress σ_e is found, and Eq. (9.4) becomes:

$$A\sigma_e^2 + D\sigma_e + F_e = 0 \tag{9.5}$$

Now substitute for the threshold value here determined of $F = F_e = -A\sigma_e^2 - D\sigma_e$ in the Yield-ellipse equation of Eq. (9.4), the equivalent stress measure is found:

$$\sigma_{e1}(\boldsymbol{\sigma}) = \sqrt{\sigma^2 + \left(\frac{B}{A}\right)\sigma\tau + \left(\frac{C}{A}\right)\tau^2 + \left(\frac{D}{A}\right)\sigma + \left(\frac{E}{A}\right)\tau - \left(\frac{D}{A}\right)} \tag{9.6}$$

For the significant condition of a threshold ellipse centered at the origin, becomes simply:

$$\sigma_{e2}(\boldsymbol{\sigma}) = \sqrt{\sigma^2 + \left(\frac{B}{A}\right)\sigma\tau + \left(\frac{C}{A}\right)\tau^2}\,. \tag{9.7}$$

In this context, the model predicts that the adhesion is holding, if

$$\sigma_e(\boldsymbol{\sigma}) < \sigma_{\text{th}} \tag{9.8}$$

A test campaign have been carried out for the adhesion of Polydimethylsiloxane against glass. The adhesion characteristics have been evaluated by means of the model of Eq. (9.7) giving the following expression for the equivalent stress

$$\sigma_{\text{e2(P/G)}} \approx \sqrt{\sigma^2 + 0.188\,\sigma\tau + 0.692\,\tau^2} \tag{9.9}$$

and a threshold equivalent stress of

$$\sigma_{\mathrm{th(P/G)}} \approx 30.5 \text{ kPa} \tag{9.10}$$

By means of functional composition $\sigma_{\mathrm{e}} = \sigma_{\mathrm{e}} \circ \boldsymbol{\sigma} \circ \boldsymbol{t} \circ \boldsymbol{F}$, and an evaluation about selected points $\boldsymbol{r}$ at the contact interface, the measure of detachment can be referred to the forces applied by the robot to the pad through its foot hinge $\sigma_{\mathrm{e}} = \sigma_{\mathrm{e}}(\boldsymbol{F})$. This model have been tested and gave conservative detachment predictions in the undertaken experiments, as illustrated in Fig. 9.1. Further test campaigns are expected in order to obtain a more accurate model.

9.2 Experimental robot setup

In this part the problem of controlling the surface contact forces is presented and resolved according to optimization criteria for an experimental robot prototype setup that have been developed for the purpose of validating the concepts [59] . A homologous simulation counterpart that reproduces the geometrical and inertial properties of the experimental prototype have been developed in Matlab$^{\mathrm{TM}}$, and validated in Adams$^{\mathrm{TM}}$. The experimental setup, illustrated in Fig. 9.5, is composed of a planar robot in a fixed configuration and a set of load cell that retrieve the contact reaction forces normal to the climbing surface. The robot joints are powered by n.3 servomotors that provide the desired torque. Joints and links are aligned in a vertical axis and numbered from top to bottom, such as joint 1 and link 1 are at the top of the robot, such as joint 2 and link 2 are at the center, and joint 3 and link 3 are at the bottom of the robot. The analyzed configuration simulates a vertical climb. The goal of the optimization control process is to define a set of desired control torques that depart the robot adhesion state from the detachment conditions. The robot is fixed in an over-constrained configuration, such that its balance is achieved also with zero torque at the joints; in this way it is possible to compare the results of an active joint control with the *natural* unloaded joint conditions.

The geometrical and inertial properties of the robot that have been used also in simulation models, are reported in Tab. 9.1. The instrumentation part is composed of n.3 load cells arranged in a vertical line, capable of retrieving the reaction forces in the direction normal to the climbing surface. For further details on the design and construction of the experimental setup, see the masters thesis of Li in [59].

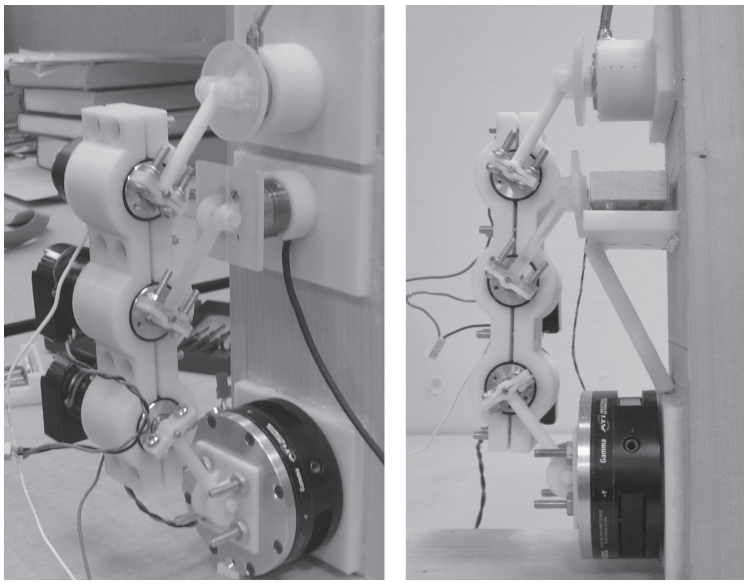

Figure 9.5: Experimental setup of the planar 3 DOF climbing robot prototype, with three joint motors and three force sensors at the contact hinges. Side and lateral view [59].

9.3 Statics of a climbing robot

In this section it is shown how it is possible to optimize the surface contact forces $\boldsymbol{F}_{ci}$ by means of applying a set of optimal control torques $\boldsymbol{\tau}$ at the robot joints. Consider the test robot with 3 powered 1-DOF joints and 3 legs and contact tips with the climbing surface, and an external gravity acceleration of $\boldsymbol{g}$, generating a weight force $m\,\boldsymbol{g}$ about the robot CM.

In order to maintain the static balance of the robot, the resultant external forces and torques applied to the robot need to compensate. The static balance equation of the whole system, represents the statics *equality constraint* of the optimization problem. Define a pole for evaluation of the torques as the origin of the reference frame solid with the climbing surface $\vec{\Sigma}_c$.

Simplified adhesion model In order to simplify the problem and given the experimental setup, consider the problem of controlling the normal components of the contact forces instead of a complete function of contact forces and torques as proposed in the previous section. In this condition, the equiv-

Property	Body	Link 1	Link 2	Link 3
l [m]	0.200	0.050	0.050	0.050
θ [rad]	–	0.876	0.876	−0.876
m [kg]	0.557	~ 0	~ 0	~ 0

Table 9.1: Experimental climbing robot geometrical and inertial properties.

alent measure of surface stress according to the definitions of the previous paragraph may be defined as:

$$\sigma_e = \bar{\sigma}_n = \frac{F_{cn}}{A_c} = \frac{\boldsymbol{F}_c^{\mathrm{T}} \boldsymbol{n}}{A_c} \tag{9.11}$$

Where $\boldsymbol{n}$ is the unit vector normal to the flat climbing surface, oriented towards the robot such that it correspond to a detaching pulling force, and A_c is the adhesion pad contact area. For this experimental setup, the x-axis is horizontal, oriented towards the vertical surface in the direction opposite to the normal vector, and the y-axis, is in vertical direction, opposite to the gravity vector.

From a global point of view, observe that the detachment of the robot from the wall would eventually start when the equivalent stress in a contact point overcomes the threshold value. In general, the robot static state can be said to be as far as possible from the undesired detaching conditions when we are able minimize the maximum value of the stress measure $\sigma_e(\boldsymbol{c})$, problem that, for the simplified model considered here, is equivalent to the minimization of the maximum value of the *pulling* contact force normal to the climbing surface:

$$\text{minimize} \max_i \{F_{cn\,i}\} \tag{9.12}$$

If we are able, by means of a joint torque loading action, to set the maximum contact force to a lower level, it can be said that the robot is working in favor of stability. The optimization problem in this form, in the contact forces variables, becomes a *minimax* problem, as is explained in the following paragraphs.

Static balance The overall balance of the robot in static configuration is guaranteed by the Newton-Euler Eq. (4.21) for the static condition, and the resultant forces and torques applied to the robot must balance. The robot balance represents the equality constraint of the problem. In order to express this constraint, define the contact forces vector variable as the collection of

all the contact forces applied at each tip to the climbing surface, equal to the opposite of the reaction forces that the surface applies to the robot:

$$\boldsymbol{c} \triangleq \begin{bmatrix} \boldsymbol{F}_1 \\ \boldsymbol{F}_2 \\ \boldsymbol{F}_3 \end{bmatrix} = - \begin{bmatrix} \boldsymbol{F}_{c1} \\ \boldsymbol{F}_{c2} \\ \boldsymbol{F}_{c3} \end{bmatrix} \tag{9.13}$$

Be G the robot center of mass of position $\boldsymbol{r}_G = \boldsymbol{r}_{OG}$, the external wrench due to the weight $\boldsymbol{F}_b$ composed of the resultant force and resultant force about the system origin due to the weight is:

$$\boldsymbol{b} \triangleq \begin{bmatrix} \mathbf{1} \\ \boldsymbol{r}_G^{\times} \end{bmatrix} \boldsymbol{F}_b = \begin{bmatrix} \boldsymbol{F}_b \\ \boldsymbol{r}_G^{\times} \boldsymbol{F}_b \end{bmatrix} \tag{9.14}$$

By means of defining a *grasp matrix* $\boldsymbol{G}$, suggested from the analogies with problems of manipulation grasping, of the form:

$$\boldsymbol{G} = \begin{bmatrix} \mathbf{1} & \mathbf{1} & \mathbf{1} \\ \boldsymbol{r}_{c1}^{\times} & \boldsymbol{r}_{c2}^{\times} & \boldsymbol{r}_{c3}^{\times} \end{bmatrix} \tag{9.15}$$

The system balance constraint can be expressed as:

$$\boldsymbol{G}\,\boldsymbol{c} = \boldsymbol{b} \tag{9.16}$$

In former Eq. (9.15), the positions vectors $\boldsymbol{r}_{ci}$ are the positions of the centers of the contact tips, while for a non-fixed robot configuration the grasp matrix depends on the configuration itself $\boldsymbol{G} = \boldsymbol{G}(\boldsymbol{\theta})$. Since the balance equation represents an under-constrained system in the contact forces variables $\boldsymbol{c}$, an optimization process can be carried out according to the discussions in Appendix A. The generic solution of the contact forces can be expressed by means of an arbitrary vector $\boldsymbol{\xi}$ as:

$$\boldsymbol{c}_{\xi} = \boldsymbol{G}^{\dagger}\boldsymbol{b} + \boldsymbol{Z}_G\,\boldsymbol{\xi} \tag{9.17}$$

The optimization of the contact forces $\boldsymbol{c}$ is the subject of the following paragraph, and can be carried out by observing that different configurations of contact forces can be achieved by means of different internal joint torques $\boldsymbol{\tau}$.

Once a desired set of contact forces $\boldsymbol{c}$ have been evaluated, the necessary joint torques that are able to produce those interaction forces are given by means of statics relations of the structure,[1] that can be obtained with the methods of statics, for example by free-body diagrams of each links of the

[1]For the robot structure of our tests, be α the inclination of the climbing surface, ℓ the length of the links, and $\boldsymbol{e}$ the eccentricity of the center of mass G with respect to the geometrical center of the main body, the statics equations of the robot can be organized

system, similar to the transposed Jacobian statics equations for serial manipulators and parallel robots. This forces Jacobian matrix is here denoted by $\boldsymbol{J}^F$. The statics relation for the robot structure can be expressed in the form:

$$\boldsymbol{\tau} = \boldsymbol{J}^F \boldsymbol{c} \tag{9.18}$$

With $\boldsymbol{J}^F$ of the experimental robot as in the footnote (1).

9.4 Contact forces optimization

In this section two optimization solutions will be considered to the contact forces distribution. Their performances have been tested on a Matlab^{TM} simulator, and validated by means of the experimental robot prototype previously described. Furthermore, give the over-constrained static configuration of the robot, it is possible to compare the results with the natural solution without any torque load at the robot joints. The two optimization procedures examined are 1) the least squares (LS) optimization, according to the theory in Appendix A, and 2) the minimax (MMX) optimization, according to standard numerical routines.

Minimax optimization The normal contact forces of all the robot tips can be extracted by means of a selection matrix $\boldsymbol{c}_n = -\boldsymbol{c}_x = \boldsymbol{S}_x \boldsymbol{c}$, as described in Chapter 5, and the MMX optimization problem of Eq. 9.12 as follows:

$$\begin{bmatrix} 1 & 1 & 1 & 0 & 0 & 0 \\ 0 & 0 & 0 & 1 & 1 & 1 \\ -d/2 & 0 & d/2 & 0 & 0 & 0 \\ \ell \sin\theta_1 & 0 & 0 & -\ell\cos\theta_1 & 0 & 0 \\ 0 & \ell\sin\theta_2 & 0 & 0 & -\ell\cos\theta_2 & 0 \\ 0 & 0 & \ell\sin\theta_3 & 0 & 0 & -\ell\cos\theta_3 \end{bmatrix} \begin{bmatrix} c_{1x} \\ c_{2x} \\ c_{3x} \\ c_{1y} \\ c_{2y} \\ c_{3y} \end{bmatrix} =$$

$$= \begin{bmatrix} mg\cos\alpha \\ mg\sin\alpha \\ \tau_\alpha \\ -\tau_1 \\ -\tau_2 \\ -\tau_3 \end{bmatrix} \quad \text{with} \quad \tau_\alpha = -\tau_1 - \tau_2 - \tau_3 - mg \cdot (e_y \cos\alpha + e_x \sin\alpha)$$

ri-formulated by taking into account the balance constraint as:

$$\begin{array}{ll} \text{minimize} & \max_i \left(\boldsymbol{S}_x \, \boldsymbol{c}\right)_i \\ \text{subject to} & \boldsymbol{G}\boldsymbol{c} = \boldsymbol{b} \end{array} \tag{9.19}$$

The solution is provided by means of standard numerical iterative routines, on which no further investigation is of interest for the purposes of these tests.

Least squares optimization On the other side, the least squares optimization of the pulling forces, can be expressed as:[2]

$$\begin{array}{ll} \text{minimize} & \|\boldsymbol{S}_x \, \boldsymbol{c}\|^2 \\ \text{subject to} & \boldsymbol{G}\boldsymbol{c} = \boldsymbol{b} \end{array} \tag{9.20}$$

Note that for a general expression of the matrix $\boldsymbol{S}_x$ that could characterize a different cost function, the problem of Eq. (9.20), results to be a Least Squares Problem with Equality constraints problem, LSE. Anyhow, given the special formulation of the cost function given in this test-case, with the cost-function matrix composed only of elements in $\mathbb{B} = \{0, 1\}$, the problem, and its solution, have been found to be equivalent to a simple under-constrained least squares problem of the form of Eq. (A.26):

$$\begin{cases} \boldsymbol{G} \, \boldsymbol{c} = \boldsymbol{b} \\ \quad \boldsymbol{c} \cong \boldsymbol{0} \end{cases} \tag{9.21}$$

and its solution is:

$$\boldsymbol{c} = \boldsymbol{G}^{\dagger} \, \boldsymbol{b} \tag{9.22}$$

For this reason in this context we use the notation LS to identify the solution to the problem in Eq. (9.20). The optimal contact forces obtained with these procedures, are then passed to the statics model of the robot of Eq. (9.18), that provides the corresponding joint control torques $\boldsymbol{\tau}$.

Simulations and experimental tests The force control concepts proposed in this Chapter, have been tested on the experimental robot prototype of Fig. 9.5, and simulations have been carried out by means of a validated simulator, in which the robot statics and the control paradigms have been implemented. The results of the optimization have been compared to the *natural* unloaded-joints configuration with $\boldsymbol{\tau} = \boldsymbol{0}$. In Fig. 9.6 are displayed the values of the normal contact forces that are obtained by means of the natural solution, and the minimax solution, showing a good correspondence between the simulation results and the experimental data. For what con-

[2] In this case the problem setting could be described by means of the notation used in the part regarding the space manipulator, but we prefer to leave the explicit definition of the cost function in order to be comparable to the minimax problem formulation.

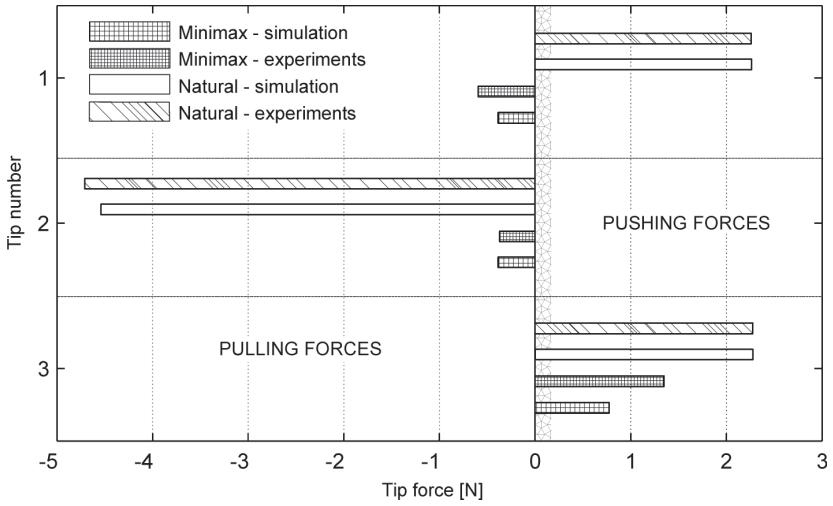

Figure 9.6: Experimental and simulation values of the normal contact forces at the tips, for the unloaded joints and the Minimax optimization.

cerns the maximum value of the pulling contact forces, from the analysis of Fig.s 9.7 and 9.6 it can be noticed that: 1) the MMX solution provides slightly better performances than the LS solution, resulting in a reduction of the maximum force of 31.0% for the simulation results, and showing also a slightly reduced control torque, whose maximum values is reduced of 19.4% with respect to the LS solution; 2) the LS and the MMX solutions highely improves the performances with respect to the unloaded natural configuration. The simulation comparisons result in a peak force reduction of 88.1% for the LS solution, and of 91.4% for the MMX solution, demonstrating the significant improvements on the stability of the climbing robot that can be attained by means of an active joint torque control. For what concernes the experimental data, the MMX solution still provide a reduction of 87.4% of the peak pulling force, confirming very good performances also in experimental conditions. The difference in terms of pulling forces results between the LS and MMX solutions are not significant for what concernes the experimental results and are below the accuracy of the experimental setup.

In order to observe the performances of the optimization in different climbing conditions, a simulation campaign have been carried out by means of changing the angle α of the climbing surface (and its normal vector) with respect to the gravity vector. The results are reported in Fig. 9.8 for the unloaded, LS, and MMX solutions, and the maximum value of the pulling forces

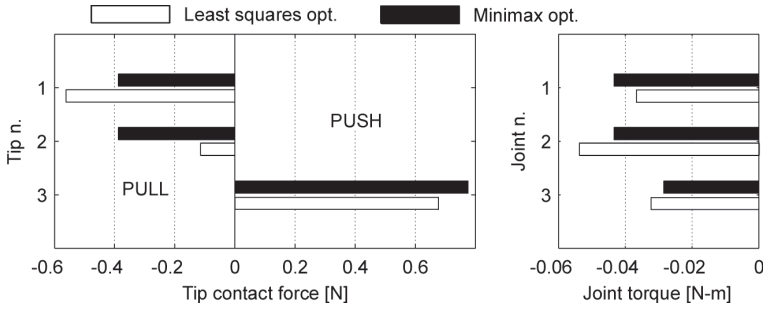

Figure 9.7: Normal contact forces and required joint torques comparison between Least Squares and Minimax optimizations.

together with the maximum value of the required joint torques is provided. In this plot, positive values are aligned with the surface-normal vector, such that they identify the pulling forces; negative values are displayed if none of the contact forces is pulling, and in that condition the minimum (closer to zero) pushing force is displayed. The simulation tests confirm very good performances of the optimization laws for what concerns the reduction in pulling forces of LS and MMX solution with respect to the natural solution, with a peak in the optimization performances for the vertical climbing conditions discussed in the experimental tests. When the climbing surface is about horizontal, the LS and MMX solutions give the same results, while the solution start to differ when some pulling detaching components arise. In this case the MMX solution provides always slightly better performances than the LS solution. The experimental condition achieved for an angle of 90 deg, results favorable in terms of joint torques to the MMX solution, although for the inverted configuration achieved for an angle of 270 deg, the convenience is inverted as well and the LS solution provides lower torques. The natural configuration results convenient only for an angle of about 160 deg, where all the three solution provide very similar results thanks to a favorable distribution of the forces. It results also interesting to observe that both the optimal solutions always exhibit a pushing force at the bottom tip, suggesting a similar behaviour to what happens in nature for example in geckos, whose climbing system relies on similar adhesive principles, and for which the bottom tip can be represented by its tail, that is pushing against the climbing surface in order to preserve the static balance.

In conclusion, from the test campaign can be asserted that 1) contact pulling forces can be greatly reduced by means of an active joint torque control, at the expense of pretty high values for the require joint torques;

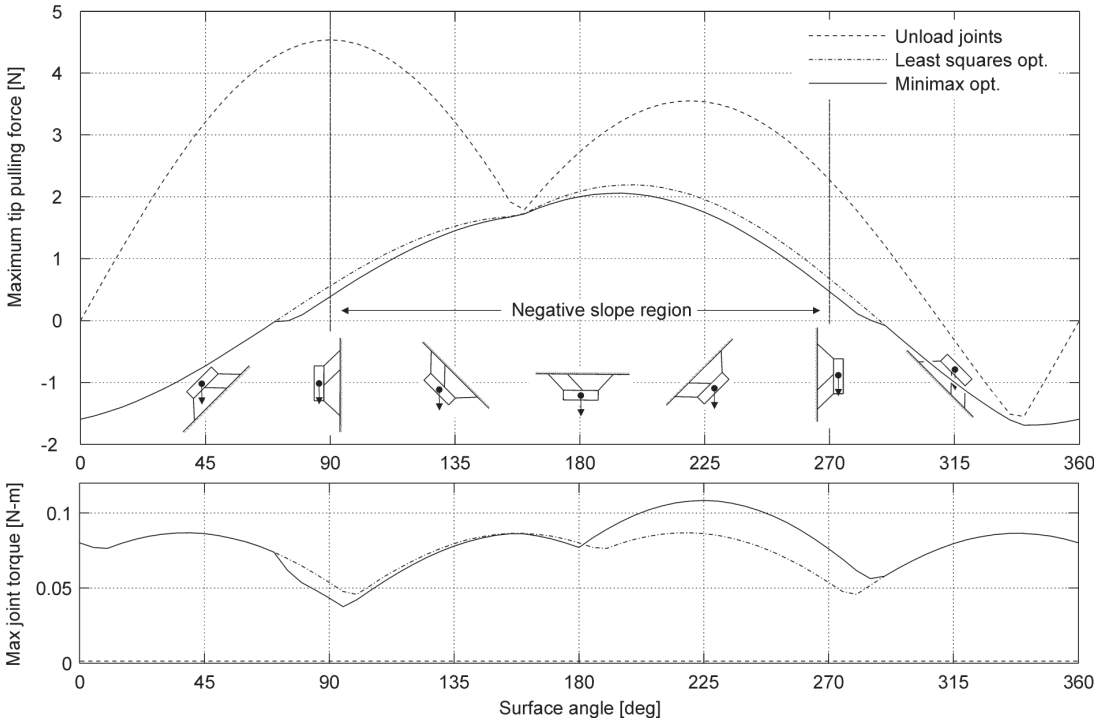

Figure 9.8: Contact forces and required joint torques for the natural, least squares, and minimax joint loading conditions.

2) the LS and MMX solutions do not significantly differ in performances with respect to the natural condition for the test configurations, suggesting further investigation in order to assess if a simple LS control, suitable for real-time implementation with a lower computational effort, is generally effective for different operative conditions. In order to reduce the required reaction torques as pointed out in the first observation, the study of an improved inequality constrained problem that consider joint-torque limits to the solution may be interesting, especially if the robot present a non null number of joint redundancies such that more freedom would be available in the solution of the joint torques.

Chapter 10

Conclusions

In this thesis original solutions to the base reaction control problem of space manipulators have been presented, by exploiting the manipulator kinematic redundancy in order to minimize appropriate dynamic cost functions defined through a weighted combination of reaction forces and torques. The development is carried out in the general framework of a trajectory-tracking manoeuvre, through local optimization of the joint trajectories, which is performed in the context of the Resolved Acceleration Control (RAC). Solutions are provided in the domain of a more general theory, presenting original applications in dynamic control of robot manipulators and extending the results in a form suitable for on-line implementations, that allows to approach a wide class of kinematics and dynamics coupled problems, thanks to the arrangement of the kinematic control problems in the form of constrained least squares problems. The proposed solutions have been compared to the traditional Least Squares (LS) solution of the kinematic redundancy, while closed form optimal solutions have been provided for the trajectory-tracking manoeuvre problem that has been defined as a Least Squares with Equality constraints (LSE) problem. The introduction of joint acceleration limits in the solution has been provided, by means of a Least Squares with Equality and Inequality constraints (LSEI) problem formulation. Original formulations of the solutions have also been proposed by means of an extended Jacobian approach, through the utilization of inverse and pseudoinverse methods. The possibility of improving the dynamic performances of the solutions by means of assigning appropriate weights to the kinematic and dynamic tasks have been assessed, thanks to the introduction and extension of the weighting method for solving the general LSE problem. Furthermore, the approach to the problem used in this work allows the unification of the base reaction control problem for fixed base manipulators and free-floating base manipula-

tors, under a common resolution scheme. The proposed control schemes have been tested on a planar three degrees-of-freedom experimental manipulator, available in the laboratories of the CISAS center at the University of Padua, in Padova (Italy), and analyzed through simulations carried out in a robot simulation environment. Test campaigns have been carried out for different configurations, and a sensitivity analysis on relevant parameters has been undertaken, demonstrating that good performances of the optimal solutions are possible in the reduction of the dynamic reaction disturbances. As a drawback, it has been observed that higher joint accelerations are requested by the optimal solutions in order to provide the desired counterbalance. Simulations of the control schemes in the free-floating base condition revealed that when attitude stability is conferred to the base platform by means of an optimal LSE kinematic control of the manipulator motion, the optimal joint acceleration solutions are not significantly different with respect to the fixed base condition, which suggests further investigation on the possibility of implementing approximate fixed base dynamics models on space robotic systems in order to reduce the computation burden of the kinematic control. As an important result, the possibility of realizing a zero reaction target-tracking manoeuvre has been demonstrated, and studies on the zero reaction workspace in the fixed base and free floating conditions have been presented. Furthermore, the approach to the problem have been extended in order to realize a general reaction-tracking manoeuvre at the manipulator base, which allows the achievement of an exact base reaction profile with simultaneous control of the end-effector motion, and thus creating a unified basis for a zero reaction control framework, and the possible extension to dynamic coordination principles for a multi-manipulator platform.

A collateral research activity on the control of the contact forces of a bio-inspired climbing robot, relying on contact devices with dry adhesion properties, have been presented. This research have been developed in cooperation with the Simon Fraser University, in Vancouver (Canada). First, a simplified model of adhesion have been proposed for a Polydimethylsiloxane micro-machined material layer against a glass surface, that reveals suitable for real-time applications. Then, a control framework have been developed in order to optimize the contact forces of the climbing robot, by means of Least Squares (LS) and Minimax (MMX) optimization schemes. The study evidenced the possibility to improve the stability of the robot by means of an active joint torque control. The design of a planar experimental robot test setup and and a simulation campaign have allowed the observation of great performances of the proposed schemes, at the expense of relatively high joint control torques.

The results accomplished in this work and presented in this thesis, motivate the effective implementation of the proposed control schemes in full scale tri-dimensional robotic systems, by means of efficient and numerically

stable computational schemes and in the framework of robust sensory feedback control systems.

Appendix A

Optimization with least squares methods

The control paradigms developed in this work, make use mostly of linear least squares methods, that are briefly reviewed in this chapter. The notation is derived from the classic numerical work on least squares problems by Lawson and Hanson in [27], and Hanson and Haskell in [29, 60]. Other useful references on least squares methods and generalized inverses can be found in [28, 61, 62], while a recent review on numerical methods for least squares problems can be found in the work of Björk [63].

Since the scope of the optimization consists in obtaining a control input solution, let's denote by $\boldsymbol{u} \in \mathbb{R}^n$ the unknown n-dimensional vectorial incognita, as common in control problems. A linear transformation $\mathbb{R}^n \to \mathbb{R}^m$ of the variable $\boldsymbol{u}$ is defined by a function of the form $\boldsymbol{f}_A(\boldsymbol{u}) \triangleq \boldsymbol{A}\boldsymbol{u} + \boldsymbol{b}$. The associated homogeneous linear transformation is $\boldsymbol{g}_A(\boldsymbol{u}) \triangleq \boldsymbol{A}\,\boldsymbol{u}$ and can be identified with its transformation matrix $\boldsymbol{A} \in \mathbb{R}^{m \times n}$.

The *range space* of $\boldsymbol{A}$, $\mathcal{R}_A \triangleq \{\boldsymbol{g}_A(\boldsymbol{u}) : \boldsymbol{u} \in \mathbb{R}^n\}$, set of all the images of the homogeneous function $\boldsymbol{g}_A$, is also the linear span of the columns of $\boldsymbol{A}$. Its dimension is called *rank* of the transformation

$$\mathrm{rk}_A \triangleq \dim(\mathcal{R}_A) \leqslant m \tag{A.1}$$

The *null space* of $\mathcal{N}_A \triangleq \{\boldsymbol{u} : \boldsymbol{g}_A(\boldsymbol{u}) = \boldsymbol{0}\}$, is the subspace of $\mathbb{R}^n$ such that the images through $\boldsymbol{g}_A$ are the null vector $\boldsymbol{0}$, and its dimension is called *nullity* of the transformation

$$\mathrm{ny}_A \triangleq \dim(\mathcal{N}_A) \leqslant n - m \tag{A.2}$$

The bounding relation at the right side in previous definition, come from the *rank-nullity theorem*, affirming that:

$$\mathrm{rk}_A + \mathrm{ny}_A = n \tag{A.3}$$

These definitions for the homogeneous transformation $\boldsymbol{g}_A$, characterize also the linear transformation $\boldsymbol{f}_A$, spanning a linear flat, which is a translated subspace passing through the point $\boldsymbol{b} \in \mathbb{R}^m$.

A.1 Linear algebraic systems

Consider now a linear system of equations:

$$\boldsymbol{A}\ \boldsymbol{u} = \boldsymbol{b} \tag{A.4}$$

Different conditions arise depending on the number of possible solutions to the problem. In fact, there can be a unique solution, no solutions at all, or infinite solutions. When the matrix $\boldsymbol{A}$ is a square full-rank matrix, $m = n$ and $\mathrm{rk}_A = n$, a unique solution exists to the problem (A.4), and is formally obtained through inversion of the transformation matrix, leading to what here we call the *inverse* solution

$$\boldsymbol{u}_{\mathrm{INV}} = \boldsymbol{A}^{-1}\ \boldsymbol{b} \tag{A.5}$$

Accurate and efficient numerical implementations of this solution can be carried out by factorization or iterative methods, see for example Golub in [62].

When infinite solutions to the problem (A.4) exist, optimization criteria can be involved in order to define a preference solution, while in the case with no solution, in many cases it's interesting to obtain the best approximation to the problem according to some criteria.

A.2 Least squares approximation and generalized inverses

Consider at first the condition for which no solution exists to the problem (A.4), that in this way results to be *over-constrained*. In this context, we are interested in determining the best approximation of the solution in a least squares sense. With this we mean the determination of the solution $\boldsymbol{u}$ such that its image $\boldsymbol{A}\ \boldsymbol{u}$ is of minimum distance from the desired vector $\boldsymbol{b}$, i.e. we intend to minimize the norm of the difference

$$\|\boldsymbol{A}\ \boldsymbol{u} - \boldsymbol{b}\|^2 \tag{A.6}$$

We rewrite this problem with the notation introduced in [27] as

$$\boldsymbol{A}\ \boldsymbol{u} \cong \boldsymbol{b} \tag{A.7}$$

This notation underlines the point that we are interested in the best approximation of the solution, and we mean this in a least squares sense.

The solution to the problem (A.7) is given by means of the Moore-Penrose generalized inverse $\boldsymbol{A}^\dagger$, or *pseudoinverse*, of the transformation matrix, in the form

$$\boldsymbol{u}_{\mathrm{LS}} = \boldsymbol{A}^\dagger\ \boldsymbol{b} \tag{A.8}$$

The concept of generalized inverses arises for rectangular matrices as in the cases of our problem. There have been defined different types of generalized inverses of a matrix, see for example [61], while the most known and most useful for our applcation is the Moore-Penrose generalized inverse that is briefly introduced here.

Moore-Penrose generalized inverse In order to introduce the generalized inverse of a matrix, it is useful to remind the notion of a projection matrix. Given a subspace $\mathcal{M}$, the *orthogonal projector* onto $\mathcal{M}$, $\boldsymbol{P}_{\mathcal{M}}$ is defined as the symmetric matrix such that:

$$\begin{cases} \boldsymbol{P}_{\mathcal{M}}\,\boldsymbol{u} = \boldsymbol{u} & \text{if} \quad \boldsymbol{u} \in \mathcal{M} \\ \boldsymbol{P}_{\mathcal{M}}\,\boldsymbol{u} = \boldsymbol{0} & \text{if} \quad \boldsymbol{u} \in \mathcal{M}^\perp \end{cases} \tag{A.9}$$

This matrix operator satisfies the properties: $\boldsymbol{1} - \boldsymbol{P}_{\mathcal{M}} = \boldsymbol{P}_{\mathcal{M}^\perp}$, and also $\boldsymbol{P} = \boldsymbol{P}_{\mathcal{R}(\boldsymbol{P})}$. Now the pseudoinverse can be defined. There have two equivalent definitions, the first, given by Moore, defines the pseudoinverse of $\boldsymbol{A}$ as the unique matrix $\boldsymbol{A}^\dagger$ such that

$$\begin{aligned} \boldsymbol{A}\,\boldsymbol{A}^\dagger &= \boldsymbol{P}_{\mathcal{R}(\boldsymbol{A})} \\ \boldsymbol{A}^\dagger\,\boldsymbol{A} &= \boldsymbol{P}_{\mathcal{R}(\boldsymbol{A}^{\mathrm{T}})} \end{aligned} \tag{A.10}$$

In this way, $\boldsymbol{A}^\dagger\boldsymbol{A}$ is the projector onto the row space of $\boldsymbol{A}$, while

$$\boldsymbol{Z}_A \triangleq \boldsymbol{1} - \boldsymbol{A}^\dagger\boldsymbol{A} = \boldsymbol{P}_{\mathcal{N}(\boldsymbol{A})} \tag{A.11}$$

is the projector onto the null space of $\boldsymbol{A}$, and $\boldsymbol{A}\,\boldsymbol{A}^\dagger$ is the projector onto its range (column space). The null-space projector $\boldsymbol{Z}_A$ will be very useful in the following developments.

The second is a formal definition, due to Penrose, and defines the pseudoinverse as the unique matrix that satisfies the following statements:

$$\boldsymbol{A}\boldsymbol{A}^\dagger\boldsymbol{A} = \boldsymbol{A} \tag{A.12}$$

$$\boldsymbol{A}^\dagger\boldsymbol{A}\boldsymbol{A}^\dagger = \boldsymbol{A}^\dagger \tag{A.13}$$

$$(\boldsymbol{A}\boldsymbol{A}^\dagger)^{\mathrm{T}} = \boldsymbol{A}\boldsymbol{A}^\dagger \tag{A.14}$$

$$(\boldsymbol{A}^\dagger\boldsymbol{A})^{\mathrm{T}} = \boldsymbol{A}^\dagger\boldsymbol{A} \tag{A.15}$$

Now we intend to give a formal expression of the pseudoinverse of a matrix. Denote by r the rank of $\boldsymbol{A}$, it can be demonstrated (see for example [28] for reference) that, for any full rank decomposition of $\boldsymbol{A}$:

$$\underset{m\times n}{\boldsymbol{A}} = \underset{m\times r}{\boldsymbol{B}}\,\underset{r\times n}{\boldsymbol{C}} \tag{A.16}$$

the following expression of the pseudoinverse satisfies the conditions of the definition:

$$\boldsymbol{A}^\dagger = [\boldsymbol{C}^{\mathrm{T}}(\boldsymbol{C}\boldsymbol{C}^{\mathrm{T}})^{-1}]\,[(\boldsymbol{B}^{\mathrm{T}}\boldsymbol{B})^{-1}\boldsymbol{B}^{\mathrm{T}}] \tag{A.17}$$

Observe that, if $\boldsymbol{A}$ is *full-row rank*, $r = n$, the identity matrix can be substituted to the matrix $\boldsymbol{B}$, $\boldsymbol{B} = \underset{n\times n}{\mathbf{1}}$, and so $\boldsymbol{A}$ itself becomes the $\boldsymbol{C}$ matrix, $\boldsymbol{C} = \boldsymbol{A}$. Then the expression for $\boldsymbol{A}^\dagger$ becomes:

$$\boldsymbol{A}^\dagger = \boldsymbol{A}^{\mathrm{T}}(\boldsymbol{A}\boldsymbol{A}^{\mathrm{T}})^{-1} \tag{A.18}$$

Vice versa, the *full-column rank* case, $r = m$, becomes:

$$\boldsymbol{A}^\dagger = (\boldsymbol{A}^{\mathrm{T}}\boldsymbol{A})^{-1}\boldsymbol{A}^{\mathrm{T}} \tag{A.19}$$

These are the more familiar expressions for the pseudoinverse of a matrix. However, it has to be noticed that the numerical implementation cannot rely on direct implementation of these expressions, because of the ill conditioning troubles due to matrix inversions, but should instead be based for instance on Singular Value Decomposition (SVD) or QR factorization [62]. The reader is reminded to the literature for further informations and properties of the pseudoinverse.

A.3 Constrained least squares problems

This section deals with *under-constrained* condition for the problem of Eq. (A.4), in which an infinite number of solutions exist. It can be shown that the general solution can be expressed by means of the null-space projector $\boldsymbol{Z}_A$, defined in Eq. (A.11), the Moore-Penrose pseudoinverse [1], and an arbitrary vector $\boldsymbol{\zeta} \in \mathbb{R}^n$, in the form

$$\boldsymbol{u}_\zeta = \boldsymbol{A}^\dagger\ \boldsymbol{b} + \boldsymbol{Z}_A\ \boldsymbol{\zeta} \tag{A.20}$$

This condition is of most interest for the subject of this thesis which is mainly concerned with redundant systems. The existence of infinite solutions allows the definition of an optimization cost function. Choosing the cost function

[1] The general expression of the solution to the under-constrained problem can be given also in terms of other generalized inverses, see for example [61].

to be a linear function in the $\boldsymbol{u}$ vector unknown, the problem results to be a linear Least Squares Problem with Equality constraints (LSE). Define the linear cost function as

$$f_{\mathrm{C}}(\boldsymbol{u}) \triangleq \|\boldsymbol{C}\boldsymbol{u} - \boldsymbol{d}\|^2 \tag{A.21}$$

This is also the norm of the vector function $\boldsymbol{f}_{\mathrm{C}}(\boldsymbol{u}) = \boldsymbol{C}\boldsymbol{u} - \boldsymbol{d}$. The problem of determining the point in $\mathbb{R}^n$ that satisfies the equality constraint of Eq. (A.4) while minimizing the cost function of Eq. (A.21) can be synthesized with the previous least-squares notation in the form

$$\begin{cases} \boldsymbol{A}\ \boldsymbol{u} = \boldsymbol{b} \\ \boldsymbol{C}\ \boldsymbol{u} \cong \boldsymbol{d} \end{cases} \tag{A.22}$$

A formulation of the solution to this problem can be provided in terms of the pseudoinverse of the matrix $\boldsymbol{A}$, that now defines an equality constraint to be exactly satisfied during the approximation of the optimization relation, and results to be:

$$\boldsymbol{u}_{\mathrm{LSE}} = \boldsymbol{A}^{\dagger}\,\boldsymbol{b} - (\boldsymbol{C}\boldsymbol{Z}_A)^{\dagger}\,(\boldsymbol{C}\boldsymbol{A}^{\dagger}\boldsymbol{b} - \boldsymbol{d}) \tag{A.23}$$

Observe that the most general solution would still consider the availability of infinite solutions to the constrained problem in terms of an arbitrary vector and the null-space projectors of $\boldsymbol{A}$ and $\boldsymbol{C}$ (see for example [28]). For the purposes of this work this condition is not relevant; furthermore, may infinite solutions still exist, the LSE solution of Eq. (A.23) provides the constrained least squares solution of minimum norm.

Numerical methods are available for an appropriate implementation of the solution to the LSE problem. Among those there have the *weighting method* investigated by Van Loan [33, 27, 62], that makes use of a scalar weighting factor μ, in order to derive a stable solution algorithm. This methods comes from the observation that the LSE solution can be expressed as the limit solution to the associate over-constrained least squares problem by weighting:

$$\begin{bmatrix} \mu\,\boldsymbol{A} \\ \boldsymbol{C} \end{bmatrix} \boldsymbol{u} \cong \begin{bmatrix} \mu\,\boldsymbol{b} \\ \boldsymbol{d} \end{bmatrix} \tag{A.24}$$

when the weight μ tends to infinity (the same could be achieved by a small weighting factor ϵ multiplying the optimization equation and made approach zero, that can be found in literature as well). Call $\boldsymbol{u}_{\mathrm{VL}}$ the solution to the weighting problem, that reduces to a LS problem in the form of Eq. (A.7), the solution to the LSE problem (A.22) is reached for

$$\boldsymbol{u}_{\mathrm{LSE}} = \lim_{\mu \to \infty} \boldsymbol{u}_{\mathrm{VL}}(\boldsymbol{\mu}) \tag{A.25}$$

This formulation has also the advantage that it allows the solution of a constrained least squares problem by means of a simple least squares routine.

The reader is reminded to the literature for suitable numeric implementations and studies on the convenient choices for the weighting factor.

Now assign the values of $\boldsymbol{C} = \mathbf{1}$, and $\boldsymbol{d} = \mathbf{0}$, to the elements of the optimization function $\boldsymbol{f}_{\mathrm{C}}$. The constrained least squares problem for these values can be reformulated as:

$$\begin{cases} \boldsymbol{A}\ \boldsymbol{u} = \boldsymbol{b} \\ \quad \boldsymbol{u} \cong \mathbf{0} \end{cases} \tag{A.26}$$

its solution is formally provided by the same LS solution to the over-constrained problem of Eq. (LS-solution)

$$\boldsymbol{u}_{\mathrm{LS}} = \boldsymbol{A}^{\dagger}\ \boldsymbol{b} \tag{A.27}$$

with the difference that the pseudoinverse matrix $\boldsymbol{A}^{\dagger}$ is evaluated differently accoring to the formulation of Eq.s (A.18) and (A.19). We still refer to this solution as LS solution, although it would be more appropriate to address it as minimum norm solution. In order to underline the different meanings one can mention the contexts of the over-constrained amd under-constrained problems. Furthermore, these observations clarify the different meaning of the pseudoinverse solutions in different dimensional contexts.

A.4 Equality and inequality constraints

The LSE problem can be further completed by taking in to account domain boundaries for the unknown variable $\boldsymbol{u}$, that in the original formulation of the Least Squares Problem with Equality and Inequality constraints (LSEI) [29]lawson1974solving can also be subject to linear transformation. In the framework of this work we address the LSEI problem as

$$\begin{cases} \boldsymbol{A}\ \boldsymbol{u} = \boldsymbol{b} \\ \boldsymbol{C}\ \boldsymbol{u} \cong \boldsymbol{d} \\ \bar{\boldsymbol{u}}_{\mathrm{l}} \leqslant \boldsymbol{u} \leqslant\ \bar{\boldsymbol{u}}_{\mathrm{u}} \end{cases} \tag{A.28}$$

The lower-bound and upper-bound inequalities are intended in a component-wise sense. The solution to this problem can be reduced to LSE subproblems and algorithms for its solution are available in literature to which the reader is reminded. The solution is here addressed as

$$\boldsymbol{u}_{\mathrm{LSEI}} = \mathrm{LSEI}(\boldsymbol{A}, \boldsymbol{b}, \boldsymbol{C}, \boldsymbol{d}) \tag{A.29}$$

since it's not possible to give a closed form solution as it was done for the LS and LSE cases due to the nature of the LSEI problem.

List of Figures

Bibliography

[1] D. A. Rohn, C. Lawrence, and A. Brush, "Microgravity robotics technology program." Houston, Texas: prepared for the International Conference and Exhibit ISA/88 of the Instrument Society of America, October 1988, also E-4148; NAS 1.15:100898; NASA-TM-100898, NASA Glenn Research Center .

[2] D. A. Rohn, "Microgravity Mechanisms and Robotics Program," NASA, Lewis Research Center, Lewis Structures Technology, Tech. Rep., 1988, vol. 1: Structural Dynamics, pp. 143–155.

[3] J. H. Miller, C. Lawrence, and D. A. Rohn, "The Dynamic Effects of Internal Robots on Space Station Freedom," in *AIAA Guidance, Navigation and Control Conference, New Orleans, LA.*, vol. 3. Washington, DC: American Institute of Aeronautics and Astronautics, Aug. 12-14 1991, pp. 1865–1878, previously announced in STAR as N91-22604.

[4] P. Putz, "Space robotics," *Reports on Progress in Physics*, vol. 65, pp. 421–463, 2002.

[5] A. Ellery, *An introduction to space robotics.* Springer Verlag, 2000.

[6] S. Dubowsky and M. A. Torres, "Path Planning for Space Manipulators to Minimize Spacecraft Attitude Disturbances," in *Proc. IEEE International Conference on Robotics and Automation*, Apr. 9–11, 1991, pp. 2522–2528.

[7] S. Dubowsky and E. Papadopoulos, "The Kinematics, Dynamics, and Control of Free-Flying and Free-Floating Space Robotic Systems," *IEEE Transactions on Robotics and Automation*, vol. 9, no. 5, pp. 531–543, Oct. 1993.

[8] E. Papadopoulos and S. Dubowsky, "On the Nature of Control Algorithms for Free-Floating Space Manipulators," *IEEE Transactions on Robotics and Automation*, vol. 7, no. 6, pp. 750–758, Dec. 1991.

[9] D. Nenchev, Y. Umetani, and K. Yoshida, "Analysis of a Redundant Free-Flying Spacecraft/Manipulator System," *IEEE Transactions on Robotics and Automation*, vol. 8, no. 1, pp. 1–6, Feb. 1992.

[10] Y. Umetani and K. Yoshida, "Resolved Motion Rate Control of Space Manipulators with Generalized Jacobian Matrix," *IEEE Transactions on Robotics and Automation*, vol. 5, no. 3, pp. 303–314, 1989.

[11] K. Yoshida and Y. Umetani, *Space Robotics: Dynamics and Control*. Kluwer Academic Publishers, 1993, ch. Control of Space Manipulators with Generalized Jacobian Matrix, pp. 165–204.

[12] Y. Xu and T. Kanade, Eds., *Space Robotics: Dynamics and Control*. Norwell, Massachussetts USA: Kluwer Academic Press, 1993.

[13] S. Moosavian and E. Papadopoulos, "Free-flying robots in space: an overview of dynamics modeling, planning and control," *Robotica*, vol. 25, no. 05, pp. 537–547, 2007.

[14] D. Nenchev, K. Yoshida, and Y. Umetani, "Analysis, design and control of free-flying space robots using fixed-attitude-restricted Jacobian matrix," in *The fifth international symposium on Robotics research*. MIT Press, 1991, pp. 251–258.

[15] M. A. Torres and S. Dubowsky, "Minimizing spacecraft attitude disturbances in space manipulator systems," *Journal of Guidance, Control, and Dynamics*, vol. 15, pp. 1010–1017, Aug. 1992.

[16] Y. Nakamura and R. Mukherjee, "Exploiting nonholonomic redundancy of free-flying space robots," *IEEE Transactions on Robotics and Automation*, vol. 9, no. 4, pp. 499–506, Aug. 1993.

[17] ——, "Nonholonomic motion planning of free-flying space robots via a bi-directional approach," *Space robotics: dynamics and control*, p. 101, 1993.

[18] C. W. De Silva, "Trajectory design for robotic manipulators in space applications," *Journal of Guidance, Control, and Dynamics*, vol. 14, pp. 670–674, 1991.

[19] R. D. Quinn, L. Chen, and C. Lawrence, "Base Reaction Control for Space-Based Robots Operating in Microgravity Environment," *Journal of Guidance, Control, and Dynamics*, vol. 17, no. 2, pp. 263–270, 1994.

[20] B. Schäfer, R. Krenn, and B. Rebele, "On inverse kinematics and kinetics of redundant space manipulator simulation," *J. of Computational and Applied Mechanics*, vol. 4, no. 1, pp. 53–70, 2003.

[21] R. Krenn and G. Hirzinger, "Modular, Generic Inverse Kinematics Algorithm Applied to Kinematically Redundant Space Manipulators," in *Proc. 8th ESA Workshop on Advanced Space Technologies for Robotics and Automation, Noordwijk, The Netherlands*, 2004.

[22] D. N. Nenchev, K. Yoshida, P. Vichitkulsawat, and M. Uchiyama, "Reaction null-space control of flexible structure mounted manipulator systems," *IEEE Transactions on Robotics and Automation*, vol. 15, no. 6, pp. 1011–1023, Dec. 1999.

[23] K. Yoshida, D. Nenchev, and M. Uchiyama, "Moving base robotics and reaction management control," in *International Symposium on Robotics Research*, vol. 7. MIT Press, 1996, pp. 100–110.

[24] J. Luh, M. Walker, and R. Paul, "Resolved-acceleration control of mechanical manipulators," *IEEE Transactions on Automatic Control*, vol. 25, no. 3, pp. 468–474, 1980.

[25] B. Siciliano, "Kinematic control of redundant robot manipulators: A tutorial," *Journal of Intelligent and Robotic Systems*, vol. 3, no. 3, pp. 201–212, 1990.

[26] Y. Nakamura, *Advanced robotics: redundancy and optimization*. Addison-Wesley Longman Publishing Co., Inc. Boston, MA, USA, 1990.

[27] C. L. Lawson and R. J. Hanson, *Solving least squares problems*. Prentice-Hall, Upper Saddle River, NJ, 1974.

[28] S. L. Campbell and C. D. Meyer, *Generalized Inverses of Linear Transformations*. New York: Dover Publications, Inc., 1991.

[29] R. Hanson and K. Haskell, "Algorithm 587: two algorithms for the linearly constrained least squares problem," *ACM Transactions on Mathematical Software (TOMS)*, vol. 8, no. 3, p. 333, 1982.

[30] Y. Zhu and X. R. Li, "Recursive least squares with linear constraints," in *Proc. 38th IEEE Conference on Decision and Control*, vol. 3, Dec. 7–10, 1999, pp. 2414–2419.

[31] K. C. Park, P. H. Chang, and S. H. Kim, "The enhanced compact QP method for redundant manipulators using practical inequality constraints," in *Proc. IEEE International Conference on Robotics and Automation*, vol. 1, May 16–20, 1998, pp. 107–114.

[32] Y. Zhang and S. Mai, "Minimum-Energy Redundancy Resolution of Robot Manipulators Unified by Quadratic Programming and its Online Solution," in *Mechatronics and Automation, 2007. ICMA 2007. International Conference on*, 2007, pp. 3232–3237.

[33] C. Van Loan, "On the method of weighting for equality-constrained least-squares problems," *SIAM Journal on Numerical Analysis*, vol. 22, no. 5, pp. 851–864, 1985.

[34] G. Stewart, "On the weighting method for least squares problems with linear equality constraints," *BIT Numerical Mathematics*, vol. 37, no. 4, pp. 961–967, 1997.

[35] S. Cocuzza, I. Pretto, and F. Angrilli, "Controllo dei disturbi dinamici sulla base di robot per manutenzione in orbita," in *XIX Congresso Nazionale AIDAA*, Forlì, Italy, 2007.

[36] S. Cocuzza, I. Pretto, C. Menon, and F. Angrilli, "Control of Dynamic Attitude Disturbances on Spacecrafts Equipped with Robotic Systems for Orbital Maintenance," in *Proceedings of the 58th International Astronautical Congress*, Hyderabad, India, September 2007.

[37] S. Cocuzza, I. Pretto, and S. Debei, "Optimal Kinematic Control of Redundant Space Robotic Systems for Orbital Manteinance: Simulated Microgravity Tests," in *Proc. 59th International Astronautical Congress*, Glasgow, UK, 2008.

[38] I. Pretto, S. Ruffieux, C. Menon, A. Ijspeert, and S. Cocuzza, "A Point-Wise Model of Adhesion Suitable for Real-Time Applications of Bio-Inspired Climbing Robots," *Journal of Bionic Engineering*, vol. 5, pp. 98–105, 2008.

[39] S. Cocuzza, I. Pretto, and S. Debei, "Novel Reaction Control Techniques for Redundant Space Manipulators: Theory and Simulated Microgravity Tests," in *Proceedings of the 60th International Astronautical Congress*, Daejeon, Korea, 2009.

[40] I. Pretto, S. Cocuzza, and S. Debei, "Tracking of a Base Reaction Profile for a Space Manipulator," in *XX AIDAA Congress*, Milano, Italy, 2009.

[41] S. Cocuzza, I. Pretto, and S. Debei, "New Approaches for Redundancy Resolution in the Reaction Torque Control of Space Manipulators," in *XX AIDAA Congress*, Milano, Italy, 2009.

[42] ——, "A Constrained Least Squares Approach for Reaction Torque Control in Spacecraft/manipulator Systems," in *Proceedings of the 60th International Astronautical Congress*, Daejeon, Korea, 2009.

[43] I. Pretto, S. Cocuzza, and S. Debei, "Dynamic Coordination Principles for Multiple Spacecraft Mounted Manipulators," in *Proceedings of the 60th International Astronautical Congress*, Daejeon, Korea, 2009.

[44] S. Cocuzza, I. Pretto, and S. Debei, "Least Squares Based Reaction Control of Space Manipulators," 2010, submitted for journal publication.

[45] ——, "Reaction Torque Control of Redundant Space Robotic Systems for Orbital Maintenance and Simulated Microgravity Tests," *Acta Astronautica*, 2010, article in press.

[46] P. C. Hughes, *Spacecraft Attitude Dynamics*. Mineola, New York: Dover Publications, Inc., 2004.

[47] B. Wie, *Space Vehicle Dynamics and Control*. Reston, Virginia USA: American Institute of Aeronautics and Astronautics, 2008.

[48] A. Liégeois, "Automatic supervisory control of the configuration and behavior of multibody mechanisms," *IEEE Transactions on Systems, Man, and Cybernetics*, vol. 7, no. 12, pp. 868–871, 1977.

[49] D. E. Whitney, "Resolved motion rate control of manipulators and human prostheses," *IEEE Transactions on Man-Machine Systems*, vol. 10, no. 2, pp. 47–53, 1969.

[50] Y. Nakamura, H. Hanafusa, and T. Yoshikawa, "Task-priority based redundancy control of robot manipulators," *The International Journal of Robotics Research*, vol. 6, no. 2, p. 3, 1987.

[51] H. Bruyninckx and O. Khatib, "Gauss' principle and the dynamics of redundant and constrained manipulators," in *IEEE International conference on robotics and automation*, vol. 3. Citeseer, 2000, pp. 2563–2568.

[52] S. Cocuzza, "Design and Construction of a Free-Flying 3D Robot for Space Applications and Microgravity Tests," Ph.D. dissertation, University of Padova, Padova, Italy, 2005.

[53] S. Cocuzza, C. Menon, and F. Angrilli, "Free-Flying Robot Tested on ESA Parabolic Flights: Simulated Microgravity Tests and Simulator Validation," in *Proceedings of the 58th International Astronautical Congress*, Hyderabad, India, 2007.

[54] S. Cocuzza, C. Bettanini, M. De Cecco, C. Menon, M. Zaccariotto, and F. Angrilli, "Free-Flying Robot 3D Simulator Validation by means of Air-Bearings Table 2D Tests Test-Bed Design," in *Proceedings of the 56th International Astronautical Congress*, October 2005.

[55] S. Cocuzza, C. Menon, A. Aboudan, A. Bulgarelli, and F. Angrilli, "Free-Flying 3D Space Robot Prototype Design and Zero-g Experiments on ESA Parabolic Flights," in *Proceedings of the 55th International Astronautical Congress*, Vancouver, Canada, October 2004.

[56] C. Menon, Y. Li, D. Sameoto, and C. Martens, "Abigaille-I: Towards the development of a spider-inspired climbing robot for space use," in *2nd IEEE RAS & EMBS International Conference on Biomedical Robotics and Biomechatronics, 2008. BioRob 2008*, 2008, pp. 384–389.

[57] S. Ruffieux, "Modeling and simulating biologically inspired climbing robots," Master's thesis, Ecole Polytechnique Fédérale de Lausanne, Lausanne, Switzerland, 2008.

[58] K. Autumn, A. Dittmore, D. Santos, M. Spenko, and M. Cutkosky, "Frictional adhesion: a new angle on gecko attachment," *Journal of Experimental Biology*, vol. 209, no. 18, p. 3569, 2006.

[59] Y. Li, "Preliminary development of a bio-inspired hexapod climbing robot relying on dry adhesives," Master's thesis, Simon Fraser University, Vancouver BC, Canada, 2008.

[60] K. Haskell and R. Hanson, "An algorithm for linear least squares problems with equality and nonnegativity constraints," *Mathematical Programming*, vol. 21, no. 1, pp. 98–118, 1981.

[61] A. Ben-Israel and T. Greville, *Generalized inverses: Theory and applications*. Springer Verlag, 2003.

[62] G. Golub and C. Van Loan, *Matrix computations*. Johns Hopkins Univ Pr, 1996.

[63] A. Björck, *Numerical methods for least squares problems*. Society for Industrial Mathematics, 1996.

[64] H. Alexander and R. Cannon, "An extended operational-space control algorithm for satellite manipulators," *Journal of the Astronautical Sciences*, vol. 38, pp. 473–486, 1990.

[65] F. Barbagli, D. Prattichizzo, and K. Salisbury, *Multi-point Interaction with Real and Virtual Objects*, ser. Springer Tracts in Advanced Robotics. Springer-Verlag New York, Inc. Secaucus, NJ, USA, 2005.

[66] C. D. Brown, *Elements of Spacecraft Design*, J. S. Przemieniecki, Ed. Reston, Virginia: American Institute of Aeronautics and Astronautics, 2002.

[67] F. Caccavale and B. Siciliano, "Kinematic Control of Redundant Free-Floating Robotic Systems," *Advanced Robotics*, vol. 15, no. 20, pp. 429–448, 2001.

[68] K. Chang and O. Khatib, "Efficient algorithm for extended operational space inertia matrix," in *Proc. IEEE Intl. Conf. Robotics and Automation*. Citeseer, 1999, pp. 350–355.

[69] F. T. Cheng, T. H. Chen, and Y. Y. Sun, "Resolving manipulator redundancy under inequality constraints," *IEEE Transactions on Robotics and Automation*, vol. 10, no. 1, pp. 65–71, Feb. 1994.

[70] F. T. Cheng, R. J. Sheu, and T. H. Chen, "The improved compact qp method for resolving manipulator redundancy," *IEEE Transactions on Systems, Man, and Cybernetics*, vol. 25, no. 11, pp. 1521–1530, Nov. 1995.

[71] C. L. Chung and S. Desa, "A global approach for using kinematic redundancy to minimize base reactions of manipulators," Carnegie Mellon University, Tech. Rep. CMU-RI-TR-89-9; NAS 1.26:186825; NASA-CR-186825, 1989.

[72] W. R. Doggett, W. C. Messner, and J. N. Juang, "Global Minimization of the Robot Base Reaction Force During 3-D Maneuvers," *IEEE Transactions on Robotics and Automation*, vol. 16, no. 6, pp. 700–711, Dec. 2000.

[73] R. Featherstone, "Robot Dynamics Algorithms," Ph.D. dissertation, University of Edinburgh, Edinburgh, UK, 1984.

[74] ——, *Rigid body dynamics algorithms*. Springer-Verlag New York Inc, 2008.

[75] ——, "A divide-and-conquer articulated-body algorithm for parallel O (log (n)) calculation of rigid-body dynamics. Part 2: Trees, loops, and accuracy," *The International Journal of Robotics Research*, vol. 18, no. 9, p. 876, 1999.

[76] ——, "A divide-and-conquer articulated-body algorithm for parallel O (log (n)) calculation of rigid-body dynamics. Part 1: Basic algorithm," *The International Journal of Robotics Research*, vol. 18, no. 9, p. 867, 1999.

[77] ——, *Robot dynamics algorithms*. Kluwer Academic Publishers, 1987.

[78] ——, "The calculation of robot dynamics using articulated-body inertias," *The International Journal of Robotics Research*, vol. 2, no. 1, p. 13, 1983.

[79] ——, "The calculation of robot dynamics using articulated-body inertias," *International Journal of Robotics Research*, vol. 2, no. 1, pp. 13–30, 1983.

[80] R. Featherstone and D. Orin, "Robot dynamics: Equations and algorithms," in *IEEE International Conference on Robotics and Automation*, vol. 1. Citeseer, 2000, pp. 826–834.

[81] J. Hollerbach and K. Suh, "Redundancy resolution of manipulators through torque optimization," *IEEE Journal of Robotics and Automation*, vol. 3, no. 4, pp. 308–316, 1987.

[82] J. M. Hollerbach, "A recursive Lagrangian formulation of manipulator dynamics and a comparative study of dynamics formulation complexity," *IEEE Transactions on Systems, Man, and Cybernetics*, vol. 10, no. 11, pp. 730–736, 1980.

[83] A. Jain, "Unified formulation of dynamics for serial rigid multibody systems," *Journal of Guidance, Control, and Dynamics*, vol. 14, no. 3, pp. 531–542, 1991.

[84] R. Longman, R. Lindberg, and M. Zedd, "Satellite-mounted robot manipulators – New kinematics and reaction moment compensation," *International Journal of Robotics Research*, vol. 6, pp. 87–103, 1987.

[85] J. Y. S. Luh, M. W. Walker, and R. P. C. Paul, "On-line computational scheme for mechanical manipulators," *Journal of Dynamic Systems, Measurement, and Control*, vol. 102, p. 69, 1980.

[86] A. Maciejewski and C. Klein, "Obstacle avoidance for kinematically redundant manipulators in dynamically varying environments," *The international journal of robotics research*, vol. 4, no. 3, p. 109, 1985.

[87] C. Menon, A. Aboudan, S. Cocuzza, A. Bulgarelli, and F. Angrilli, "Free-flying robot tested on parabolic flights: Kinematic control," *Journal of Guidance Control and Dynamics*, vol. 28, no. 4, p. 623, 2005.

[88] C. Menon, A. Aboudan, S. Cocuzza, A. Bulgarelli, C. Bettanini, M. Marchesi, and F. Angrilli, "Self-balancing free flying 3 D underactuated robot for zero-g object capture," in *54 th International Astronautical Congress of the International Astronautical Federation(IAF)*, 2003.

[89] J. Merlet, *Parallel robots*. Springer-Verlag New York Inc, 2006.

[90] S. A. A. Moosavian and E. Papadopoulos, "Free-flying robots in space: an overview of dynamics modeling, planning and control," *Robotica*, vol. 25, no. 5, pp. 537–547, 2007.

[91] D. Nenchev, K. Yoshida, and Y. Umetani, "Analysis, design and control of free-flying space robots using fixed-attitude-restricted jacobian matrix," in *The fifth international symposium on Robotics research*. Cambridge, MA, USA: MIT Press, 1990, pp. 251–258.

[92] K. A. O'Neil, "Divergence of linear acceleration-based redundancy resolution schemes," *IEEE Transactions on Robotics and Automation*, vol. 18, no. 4, pp. 625–631, Aug. 2002.

[93] M. Oda, "Attitude Control Experiments of a Robot Satellite," *Journal of Spacecraft and Rockets*, vol. 37, no. 6, pp. 788–794, 2000.

[94] E. Papadopoulos and S. Dubowsky, "Dynamic singularities in free-floating space manipulators," *ASME J. Dyn. Syst., Meas., Contr.,115:1*, no. 115, pp. 44–52, 1993.

[95] E. Papadopoulos and S. A. A. Moosavian, "Dynamics & control of space free-flyers with multiple arms," *Journal of Advanced Robotics*, no. 9, pp. 603–624, 1995.

[96] E. Papadopoulos, I. Tortopidis, and K. Nanos, "Smooth planning for free-floating space robots using polynomials," in *Proc. 2005 IEEE/ICRA Intl. Conf. On Robotics and Automation*, 2005, pp. 4283–4288.

[97] J. Park, W.-K. Chung, and Y. Youm, "Characterization of instability of dynamic control for kinematically redundant manipulators," in *Proc. IEEE International Conference on Robotics and Automation ICRA '02*, vol. 3, May 11–15, 2002, pp. 2400–2405.

[98] I. Pretto, "Minimizzazione dei disturbi dinamici sulla base di robot free-flying," Master's thesis, Università degli Studi di Padova, 2006.

[99] M. Raibert, *Legged robots that balance*. MIT press Cambridge, MA, 1986.

[100] G. Rodriguez, "Spatial operator approach to flexible manipulator inverse and forward dynamics," in *1990 IEEE International Conference on Robotics and Automation, Cincinnati, OH*, 1990, pp. 845–850.

[101] G. Rodriguez, A. Jain, and K. Kreutz-Delgado, "A spatial operator algebra for manipulator modeling and control," *The International Journal of Robotics Research*, vol. 10, no. 4, pp. 371–381, 1991.

[102] D. Rohn, C. Lawrence, and J. Miller, "Reaction-compensation technology for microgravity laboratory robots," Tech. Rep., 1990.

[103] L. Sciavicco and B. Siciliano, *Modelling and control of robot manipulators*. Springer Verlag, 2000.

[104] Y. Umetani and K. Yoshida, "Resolved motion rate control of space manipulators with generalized jacobian matrix," *IEEE Transactions on Robotics and Automation*, vol. 5, no. 3, pp. 303–314, June 1989.

[105] Z. Vafa and S. Dubowsky, "On the dynamics of space manipulators using the virtual manipulator, with applications to path planning," *The Journal of the Astronautical Sciences*, no. 38, pp. 441–472, 1990.

[106] C. W. Wampler, "Manipulator inverse kinematic solutions based on vector formulations and damped least-squares methods," *IEEE Transactions on Systems, Man, and Cybernetics*, vol. SMC 16, no. 1, pp. 93–101, 1986.

[107] Y. S. Xia, G. Feng, and J. Wang, "A primal-dual neural network for online resolving constrained kinematic redundancy in robot motion control," *IEEE Transactions on Systems, Man, and Cybernetics, Part B*, vol. 35, no. 1, pp. 54–64, Feb. 2005.

[108] J. X. Xu and W. Wang, "Two optimization algorithm for solving robotics inverse kinematics with redundancy," in *Proc. IEEE International Conference on Control and Automation ICCA 2007*, May 2007, pp. 3021–3028.

[109] K. Yoshida, "Engineering Test Satellite VII Flight Experiments for Space Robot Dynamics and Control: Theories on Laboratory Test Beds Ten Years Ago, Now in Orbit," *The International Journal of Robotics Research*, vol. 22, no. 5, pp. 321–335, 2003.

[110] ——, "Practical coordination control between satellite attitude and manipulator reaction dynamics based on computed momentum concept," in *Proc. IEEE/RSJ/GI International Conference on Intelligent Robots and Systems '94. 'Advanced Robotic Systems and the Real World' IROS '94*, vol. 3, Sept. 12–16, 1994, pp. 1578–1585.

[111] Y. Zhang, S. S. Ge, and T. H. Lee, "A unified quadratic-programming-based dynamical system approach to joint torque optimization of physically constrained redundant manipulators," *IEEE Transactions on Systems, Man, and Cybernetics, Part B*, vol. 34, no. 5, pp. 2126–2132, Oct. 2004.

[112] Y. Zhang and J. Wang, "Obstacle avoidance for kinematically redundant manipulators using a dual neural network," *IEEE Transactions on Systems, Man, and Cybernetics, Part B*, vol. 34, no. 1, pp. 752–759, Feb. 2004.

[113] ——, "A dual neural network for convex quadratic programming subject to linear equality and inequality constraints," *Physics Letters A*, vol. 298, no. 4, pp. 271–278, 2002.

[114] Y. Zhang, J. Wang, and Y. Xia, "A dual neural network for redundancy resolution of kinematically redundant manipulators subject to joint limits and joint velocity limits," *IEEE Transactions on Neural Networks*, vol. 14, no. 3, pp. 658–667, May 2003.